

BIOPHYSICS MODEL IMPROVEMENT IN MAGNETIC RESONANCE
IMAGING: CEREBRAL METABOLIC RATE OF OXYGEN

A Dissertation

Presented to the Faculty of the Graduate School

of Cornell University

In Partial Fulfillment of the Requirements for the Degree of

Doctor of Philosophy

by

JUNGHUN CHO

DECEMBER 2019

© 2019 JUNGHUN CHO
ALL RIGHTS RESERVED

BIOPHYSICS MODEL IMPROVEMENT IN MAGNETIC RESONANCE
IMAGING: CEREBRAL METABOLIC RATE OF OXYGEN

JUNGHUN CHO, PH. D.

Cornell University 2019

Cerebral metabolic rate of oxygen (CMRO₂) and oxygen extraction fraction (OEF) are valuable to investigate tissue viability and function. Numerous magnetic resonance imaging (MRI) methods have been proposed to estimate them quantitatively. While those methods are investigated in healthy subjects, a robust framework is elusive from literature for reliable CMRO₂ and OEF estimation in pathological scenarios.

This thesis developed algorithms that improve the accuracy, robustness and applicability of CMRO₂ and OEF for both healthy and pathological subjects. First, quantitative susceptibility mapping (QSM)-based and quantitative blood oxygen-level dependent magnitude (qBOLD)-based CMRO₂ method were combined to resolve the issues of the individual methods. Second, the cluster analysis of time evolution (CAT) was proposed to improve robustness of the combined model against noise.

With the technical advances in this thesis, CMRO₂ and OEF that are robust against noise and sensitive to pathological scenarios, e.g. ischemic stroke lesion, can be estimated.

BIOGRAPHICAL SKETCH

Junghun Cho received a Bachelor of Science degree in Physics from the University of Michigan - Ann Arbor in 2008 and a Master of Science degree in Physics from the University of Wisconsin - Madison in 2010. He joined the graduate program in Biomedical Engineering at Cornell University in the Fall 2014 and received a Master of Science degree in Biomedical Engineering in 2017.

Dedicated to my parents who have served as models of sincerity and always
encouraged me to turn my dreams into reality
and to my extraordinary wife
for her boundless support and perpetual kindness and positivity

ACKNOWLEDGMENTS

During my Ph.D. study, I have always been grateful for the support, guidance and inspiration from wonderful people.

First, I would like to thank my advisor and mentor, Professor Yi Wang. He has been an exceptional role model in rigorous scientific thinking based on first principles. I am grateful for his lesson to think deeply and to get to the bottom of research topics. I was profoundly moved by his insistence on a thorough understanding in research, which leads to breakthroughs. I will continue to strive to practice his teachings.

Sincere gratitude is owed to Professors, Dr. Pascal Spincemaille and Dr. Thanh Nguyen. They were the first people I would turn to whenever I encountered academic or technical hurdles in my research. They were always insightful and provided great suggestions. They contributed in various aspects to my research, including discussing CMRO2 model optimizations.

My research could never be achieved without the help of other colleagues in our lab. Former post-docs, Dr. Dong Zhou and Dr. Youngwook Kee, provided great insights not only about MRI, but also about life. Countless discussions about quadrupole derivation, CMRO2 and QSM modeling, philosophies and meditations made me feel alive in both research and life. I also want to thank Yan Wen, Alexey Dimov and Zhe Liu for their support through many late-night scans and discussions about MRI principles. Dr. Shun Zhang provided valuable clinical data and helped me through demanding tasks including ROI segmentation in many of my projects. Kelly Gillen provided constant

help through all the paperwork and logistics arrangement, and gave professional edits in the preparing of my publications. I feel fortunate to work with other talented members in the lab, Sarah Eskreis-Winkler, Kofi Deh, Ramin Jafari, Liangdong Zhou, Jingwei Zhang, Jinwei Zhang, Qihao Zhang, John Morgan, who have provided with insight and encouragement.

Most importantly, I thank my family. To my mother, Yangok Park, who serves as my wonderful example of integrity and sincerity and provides sage advice about how to embrace life. To my father, Young Jae Jo, for inspiring me to follow my dreams and showing me the power of humor, which has enabled me to navigate the complexities in research and life. To my mother in law, Youngsuk Lee, for providing unconditional love and care. To my father in law, Kwonsoo Park, for his wise advice and warm-hearted encouragement. To my brother and his wife, Jinhwan Jo and Kyohyun Lee, for being my admirable life-long friends. To my brother in law and his wife, Joosun Park and Seulki Hyun, for letting me have awesome younger brother and sister.

I have shared the most important decisions of my life with Joo Won Park, my most elegant and exceptional wife. She shows me the beauty of being together. Her boundless support, encouragement, kindness are what have enabled me to overcome difficulties in life and research. She is the most beautiful thing that happened to my life, followed by the cutest being called Reina Cho.

Finally, I would like to acknowledge the members on my special committee, Dr. Yi Wang, Dr. Peter Doerschuk, Dr. Chris Schaffer and Dr. Micheal Kaplitt, for agreeing to examine this thesis.

TABLE OF CONTENTS

BIOGRAPHICAL SKETCH.....	v
ACKNOWLEDGMENTS.....	vii
TABLE OF CONTENTS.....	ix
LIST OF FIGURES.....	xi
LIST OF ABBREVIATIONS.....	xii
1 Introduction.....	1
1.1 QSM-based CMRO2 method.....	1
1.2 qBOLD-based CMRO2 method.....	4
1.3 Summary of Contributions.....	5
2 Background.....	7
2.1 MRI principle to signal model.....	7
2.1.1 Larmor frequency and transverse magnetization.....	7
2.1.2 Signal detection.....	8
2.1.3 Signal in time.....	9
2.1.4 Signal in time with relaxation.....	9
2.1.5 Signal in image domain.....	10
2.2 Signal model to QSM-based and qBOLD modeling.....	11
2.2.1 QSM-based modeling.....	11
2.2.2 qBOLD modeling.....	12
3 CMRO2 Mapping by Combining QSM and qBOLD.....	15
3.1 Abstract.....	15
3.2 Introduction.....	15
3.3 Theory.....	16
3.4 Methods and Materials.....	17
3.4.1 Data Acquisition.....	17
3.4.2 Image Processing.....	18
3.4.3 Optimization.....	19
3.4.4 Statistical Analysis.....	21
3.5 Results.....	22
3.6 Discussion.....	28
3.7 Conclusion.....	31
4 Cluster analysis of time evolution for QSM+qBOLD.....	32
4.1 Abstract.....	32
4.2 Introduction.....	32
4.3 Theory.....	33
4.4 Methods and Materials.....	34
4.4.1 Numerical Simulation 1.....	34
4.4.2 Numerical Simulation 2.....	34
4.4.3 Data Acquisition.....	35
4.4.4 Image Processing.....	36
4.4.5 Clustering.....	37
4.4.6 Optimization.....	38
4.4.7 Statistical Analysis.....	41
4.5 Results.....	42

4.6	Discussion	53
4.7	Conclusion	58
5	Future directions and conclusion.....	59
5.1	Future directions	59
5.1.1	Clinical application of QQ.....	59
5.1.2	Deep learning for QQ	66
5.1.3	Validation of QQ	70
5.2	Conclusion	73
	APPENDIX	74
	Dipole and Quadrupole formulism derivation.....	74
	REFERENCE	76

LIST OF FIGURES

<i>Figure 3.1. L-curve analysis</i>	21
<i>Figure 3.2. CMRO2 maps in axial, sagittal, and coronal sections</i>	23
<i>Figure 3.3. OEF, v, χ_{nb}, and CMRO2 maps</i>	24
<i>Figure 3.4. ROI comparisons</i>	26
<i>Figure 3.5. Bland-Altman plots</i>	27
<i>Figure 4.1. Influence of SNR on the estimated Y (Numerical Simulation 1)</i>	43
<i>Figure 4.2. Comparison between QQ w/o and w/ CAT (Numerical Simulation 2)</i>	45
<i>Figure 4.3. Parameter maps between QQ w/o and w/ CAT (healthy subject)</i>	46
<i>Figure 4.4. Parameter maps between QQ w/o and w/ CAT (6 d post onset)</i>	47
<i>Figure 4.5. OEF histogram in the lesion and its contralateral side (12 d post onset)</i>	49
<i>Figure 4.6. The segmentations and resultant OEF maps</i>	50
<i>Figure 4.7. X-means clustering ($K = 17$) and the average signal evolution</i>	51
<i>Figure 4.8. ROI analysis</i>	52
<i>Figure 5.1. OEF maps in six ischemic stroke patients</i>	60
<i>Figure 5.2. Average OEF value in the lesion and the contralateral side</i>	61
<i>Figure 5.3. Average OEF between healthy controls (HC) and MS patients</i>	63
<i>Figure 5.4. T1w, T2w, QSM, and OEF maps for an MS patient</i>	64
<i>Figure 5.5. Lesion OEF in three MS types</i>	65
<i>Figure 5.6. Comparison between the OEFs obtained by QQ-CAT and QQ-NET</i>	68
<i>Figure 5.7. OEF Comparison between QQ-CAT and QQ-NET</i>	69
<i>Figure 5.8. Scatter plot of the OEF ratio between lesion and contralateral side</i>	70
<i>Figure 5.9. Baseline OEF, CBF, CMRO2 map between DGC and QQ</i>	72
<i>Figure 5.10. OEF, CBF, CMRO2 from QQ between baseline and hypercapnia</i>	73

LIST OF ABBREVIATIONS

ACA	Anterior Cerebral Artery
AD	Alzheimer's Disease
ASL	Arterial Spin Labeling
BIC	Bayesian Information Criteria
BOLD	Blood Oxygen Level-Dependent magnitude
CAT	Cluster Analysis of Time evolution
CMRO ₂	Cerebral Metabolic Rate of Oxygen
CGM	Cortical Gray Matter
CSF	Cerebrospinal Fluid
DGC	Dual-Gas Challenge calibrated BOLD
DWI	Diffusion Weighted Image
FOV	Field Of View
GM	Gray matter
MCA	Middle Cerebral Artery
mGRE	multi-echo Gradient Echo
MEDI	Morphology Enabled Dipole Inversion
MRI	Magnetic Resonance Imaging
MS	Multiple Sclerosis
NAWM	Normal-Appearing White Matter
OEF	Oxygen Extraction Fraction
PCA	Posterior Cerebral Artery
PDF	Projection onto Dipole Fields
PET	Positron Emission Tomography
PWI	Perfusion Weighted Image
qBOLD	quantitative BOLD
QSM	Quantitative Susceptibility Mapping
QQ	QSM+qBOLD
QUIXOTIC	QUantitative Imaging of eXtraction of Oxygen and Tissue Consumption
RMSE	Root Mean Square Error
ROI	Region Of Interest
SNR	Signal to Noise Ratio
SS	Straight Sinus
SSIM	Structure Similarity Index
TE	Echo Time
TR	Repetition Time
VSF	Voxel Spread Function
VT	Vascular Territories
WM	White Matter

CHAPTER 1

1 INTRODUCTION

The cerebral metabolic rate of oxygen (CMRO₂) and oxygen extraction fraction (OEF) are important markers of brain tissue viability and function, such as in stroke (1-3), and their mapping using MRI has received great interest (4). MR signal is highly sensitive to the strongly paramagnetic deoxyhemoglobin converted from weakly diamagnetic deoxyhemoglobin. Quantitative models have been proposed to investigate the effect of deoxyhemoglobin in blood on the MRI signal, including 1) magnitude signal modeling methods such as quantitative imaging of extraction of oxygen and tissue consumption (QUIXOTIC) (5), calibrated functional MRI (6-9), and quantitative blood oxygen level dependent magnitude (qBOLD) (10-12), and 2) phase signal modeling methods for a value of the whole brain CMRO₂ (13-16) and a voxel-wise quantitative susceptibility mapping (QSM)-based CMRO₂ methods (17-19).

We will focus on two CMRO₂ methods, QSM-based (17-19) and qBOLD-based (11,12) CMRO₂ method. Both don't need vascular challenges, which are impractical in clinical settings. Each utilizes phase and magnitude signal from the same underlying multi-echo gradient echo (mGRE) data, respectively. We will review the two methods. Then, we will specify their limitations and propose novel algorithms to overcome these limitations as major contribution of the current thesis.

1.1 QSM-based CMRO₂ method

In this chapter, we examine QSM-based CMRO₂ methods (17-19). QSM-based CMRO₂

methods separate the voxel-wise susceptibility χ into two main contributions: non-blood tissue and blood susceptibility, which is mainly deoxyhemoglobin in venous blood. The susceptibility χ can be estimated via QSM (20-22). QSM algorithms solve the inversion problem from the measured magnetic field b to susceptibility map χ . The forward problem is as follows.

$$b = d * \chi \quad [1.1]$$

Where d is dipole kernel:

$$d(\mathbf{r}) = \frac{1}{4\pi} \frac{3 \cos^2 \theta - 1}{|\mathbf{r}|^3}, \quad \mathbf{r} \neq \mathbf{0} \quad [1.2]$$

θ is the angle between the location vector \mathbf{r} and the main magnetic field. Eq. 1.1 can be derived by using the Maxwell's equation with magnetostatic condition and Lorentz sphere correction (See Appendix for the detail derivation).

Note that Eq. 1.1 is the 1st order Taylor expansion result from the Maxwell's equation (Eq. A5). It means that current QSM algorithms approximate b to be dipole field and assume a uniform susceptibility distribution within a voxel. More generally, tissue magnetic susceptibility sources can be expressed in a multipole expansion. The dipole model in current QSM may be improved by including the quadrupole moments, defined as the first moment of susceptibility distribution within a voxel (2nd order in Eq. A5). In regions with non-uniform susceptibility distribution such as gray-white matter interfaces, the quadrupole moments can be substantial and their field contribution is non-negligible compared to susceptibility anisotropy field contributions. The quadrupole moment might need to be considered for a comprehensive field model. We developed the inclusion of the quadrupole moment (23), in addition to the thesis topic.

QSM-based CMRO2 method contains the signal equation for the susceptibility of a voxel, F_{QSM} , which is the sum of three terms: the non-blood tissue susceptibility (χ_{nb}), the plasma susceptibility and the hemoglobin susceptibility (18,19):

$$\begin{aligned}
F_{QSM} = & (1 - CBV) \cdot \chi_{nb} \\
& + CBV \cdot (1 - \psi_{Hb}) \cdot \chi_p \\
& + CBV \cdot \psi_{Hb} \cdot \left[\chi_{oHb} + \Delta\chi_{Hb} \cdot \frac{v \cdot [dH]_v + (CBV - v) \cdot [dH]_a}{CBV \cdot [H]} \right] \quad [1.3]
\end{aligned}$$

where CBV is total blood volume (dimensionless fraction), ψ_{Hb} the hemoglobin volume fraction (dimensionless) which was set to 0.0909 for tissue based on Hct 0.357 (18,24-26), χ_p the blood plasma susceptibility, set to -37.7 ppb (27), χ_{oHb} the oxyhemoglobin susceptibility (-813 ppb) (18,25,28), $[dH]_v$ and $[dH]_a$ the concentration ($\mu\text{mol/ml}$) of deoxyhemoglobin in venules and arterioles, respectively. $[dH]_v$ and $[dH]_a$ will be expressed in terms of Y and Y_a below. $\Delta\chi_{Hb}$ is the susceptibility difference between deoxy- and oxy-hemoglobin (12522 ppb) (17,27).

Eq. 1.3 is then expressed in terms of 1) the ratio between the venous and total blood volume $\alpha = v/CBV$, assumed to be constant (0.77) (29), 2) the fully oxygenated blood susceptibility, $\chi_{ba} = \psi_{Hb} \cdot \chi_{oHb} + (1 - \psi_{Hb}) \cdot \chi_p$ (19), 3) the arterial oxygenation $Y_a = \frac{[H] - [dH]_a}{[H]}$, and 4) the venous oxygenation, $Y = \frac{[H] - [dH]_v}{[H]}$. This results in:

$$F_{QSM}(Y, v, \chi_{nb}) = \left(1 - \frac{v}{\alpha}\right) \cdot \chi_{nb} + \left[\frac{\chi_{ba}}{\alpha} + \psi_{Hb} \cdot \Delta\chi_{Hb} \cdot \left(-Y + \frac{1 - (1 - \alpha) \cdot Y_a}{\alpha}\right)\right] \cdot v \quad [1.4]$$

where the two terms represent the contribution of non-blood tissue and blood to the total susceptibility, respectively.

QSM-based CMRO2 methods require estimating two unknowns per voxel (17-19): Y and χ_{nb} (inversion of Eq. 1.4). The venous blood volume fraction (v) is assumed to be known from the linear relationship between cerebral blood flow (CBF) and v (30). The linear relationship was acquired with a linear regression on the total number of voxels in healthy subjects' brain. It, hence, might hold for individual voxels and for patient cases.

1.2 qBOLD-based CMRO2 method

The qBOLD method models mGRE magnitude in a voxel (12):

$$F_{qBOLD}(Y, v, \chi_{nb}, S^0, R_2, TE) = S^0 \cdot e^{-R_2 \cdot TE} \cdot F_{BOLD}(v, Y, \chi_{nb}, TE) \cdot G(TE) \quad [1.5]$$

where S^0 is signal intensity at measurement time $TE=0$, R_2 is transverse relaxation rate, G is the macroscopic field inhomogeneity contributing to the GRE signal and F_{BOLD} is the mGRE signal decay due to deoxygenated blood in vessel network: $F_{BOLD}(Y, v, \chi_{nb}, t) = \exp[-v \cdot f_s(\delta\omega \cdot t)]$.

The function f_s is the signal decay by the blood vessel network (12,31), whose asymptotic behavior is $f_s(\delta\omega \cdot TE) \approx \frac{3}{10}(\delta\omega \cdot TE)^2$ for $TE \ll 1/\delta\omega$, and $f_s(\delta\omega \cdot TE) \approx \delta\omega \cdot TE$ for $TE \gg \frac{1}{\delta\omega}$, where $\delta\omega$ is the characteristic frequency due to the susceptibility difference between deoxygenated blood and the surrounding tissue:

$$\delta\omega(Y, \chi_{nb}) = \frac{1}{3} \cdot \gamma \cdot B_0 \cdot [\text{Hct} \cdot \Delta\chi_0 \cdot (1 - Y) + \chi_{ba} - \chi_{nb}] \quad [1.6]$$

where γ is the gyromagnetic ratio (267.513 MHz/T), B_0 is the main magnetic field (3T in our study), Hct is hematocrit (0.357) (18), $\Delta\chi_0$ is the susceptibility difference between fully

oxygenated and fully deoxygenated red blood cell ($4\pi \times 0.27\text{ppm}$) (32), χ_{ba} is the susceptibility of fully oxygenated blood, -108.3 ppb estimated with using Hct 0.357 (19).

From the magnitude of the mGRE signal of each voxel, the qBOLD-based CMRO2 methods (12) have solved four unknowns: signal intensity at TE=0 (S^0), transverse relaxation rate (R_2), v , and Y (10-12) (inversion of Eq. 1.5). qBOLD assumes χ_{nb} to be the same as that of fully oxygenated blood ($\chi_{ba} = \chi_{nb}$) (10-12,33). This constant χ_{nb} assumption might not be true because it ignores regional variation, such as highly positive tissue susceptibility in deep gray matters by ferritin and negative tissue susceptibility in white matter by myelin (22).

1.3 Summary of Contributions

The work in this thesis is designed to improve individual QSM-based and qBOLD-based CMRO2 method. First, we combined the two models. Second, we improved the robustness of the combined model. These developments are described in a separate chapter.

1. CMRO2 Mapping by Combining QSM and qBOLD. Chapter 3 presents the model combination of QSM and qBOLD (34). It removes unnecessary assumptions in each individual methods, such as linear assumption between v and CBF in the QSM-based model and constant χ_{nb} assumption in the qBOLD-based model. It also utilizes both phase (QSM-based modeling) and magnitude (qBOLD-based modeling) signal from the same mGRE data. The combined model provided clearer gray and white matter contrast in CMRO2, more uniform OEF than QSM, and less noisy OEF than qBOLD. These agree well with reference PET studies.

2. Cluster analysis of time evolution for QSM+qBOLD. Chapter 4 proposes cluster analysis of time evolution (CAT) for the combined QSM+qBOLD (QQ) model to improve the robustness

again noise (35). QQ model is involved with highly non-convex optimization, and so susceptible to substantial errors in OEF at typical signal-to-noise (SNR). CAT method assumes that voxels with a similar mGRE signal evolution have similar model parameter values and that the number of clusters is much smaller than the number of voxels. Consequently, averaging over a cluster can substantially increase SNR for a cluster-wise inverse solution. QQ with CAT showed more accurate OEF in simulations, more uniform and less noisy OEF in healthy subjects. In ischemic stroke patients, regions of low OEF were confined within the lesions defined on diffusion weighted image (DWI) when using CAT, which was not observed without CAT.

CHAPTER 2

2 BACKGROUND

QSM-based and qBOLD method can be derived from a MRI voxel signal model (36).

$$S(TE) \approx \bar{m} \cdot \Delta V \cdot e^{-R_2 \cdot TE} \cdot \langle e^{ib \cdot \omega_0 \cdot TE} \rangle \quad [2.1]$$

Where \bar{m} is average spin distribution in a voxel, ΔV is voxel volume, R_2 is the signal decay rate by irreversible spin-spin interaction, TE is measurement time, b is susceptibility field scaled to the main magnetic field, ω_0 . $\langle \cdot \rangle$ is the average over a voxel.

In this chapter, Eq. 2.1 will be derived from MRI principle (36). Then, QSM-based (Eq. 1.3) and qBOLD (Eq. 1.5) modeling will be obtained from Eq. 2.1 (11,17,22,36).

2.1 MRI principle to signal model

Our body consists of ~ 60% water. Hydrogen nucleus in the water molecule has intrinsic property, spin s , due to single unpaired proton. Proton has one-half spin, hence two states can exist, spin-up and spin-down. Without an external field, the energy levels of the two states are the same, i.e. degenerated. Under an external field, e.g. our body is located in MRI, the energy level of spin-up state (parallel to the external field) becomes lower than the one of spin-down state. A small difference in the spin population between two states creates a net magnetization, m .

2.1.1 Larmor frequency and transverse magnetization

In an external field \mathbf{B} , m precesses clockwise around \mathbf{B} with an angular velocity ω .

$$\boldsymbol{\omega} = -\gamma\mathbf{B} \quad [2.2]$$

Where the magnitude of $\boldsymbol{\omega}$ is precession frequency or Larmor frequency, γ is the proportionality constant between $\boldsymbol{\omega}$ and \mathbf{B} , referred to as the gyromagnetic ratio, e.g. 42.58 MHz/T for ^1H .

The magnetization vector \mathbf{m} can be expressed in the z -direction (along \mathbf{B} direction) component, m_z , and the transverse (x, y) plane component, m_{\perp} .

$$m_{\perp} = m e^{-i\omega t} \quad [2.3]$$

Eq. 2.3 describes a solution to the first-order differential equation.

$$\frac{dm_{\perp}}{dt} = -i\omega m_{\perp} \quad [2.4]$$

Eq. 2.4 can be expressed in a vector form with using \mathbf{B} .

$$\frac{d\mathbf{m}}{dt} = \gamma\mathbf{m} \times \mathbf{B} \quad [2.5]$$

2.1.2 Signal detection

Suppose a loop coil is located nearby the precessing magnetization \mathbf{m} . The magnetic flux ϕ through the area of the loop by \mathbf{m} would oscillate at the frequency ω . Then, the voltage signal in the coil, s , can be induced based on Faraday's Law.

$$s = -\frac{d\phi}{dt} = i\omega\phi \quad [2.6]$$

The flux ϕ can be expressed as m_{\perp} with the assumption that the coil sensitivity is unity for simplicity.

$$s = i\omega m_{\perp} \quad [2.7]$$

The detected signal in a coil is the summation of the flux contributions from all spin. Hence, a general signal equation can be expressed by taking a spatial integral.

$$s = i \int \omega(\mathbf{r}) m_{\perp}(\mathbf{r}) e^{-i\omega(\mathbf{r})t} d^3\mathbf{r} \quad [2.8]$$

2.1.3 Signal in time

The $\omega(\mathbf{r})$ in Eq. 2.8 can be divided into three contributions.

$$\omega(\mathbf{r}) = \omega_0 + \gamma\mathbf{G} \cdot \mathbf{r} + b(\mathbf{r})\omega_0 \quad [2.9]$$

Where ω_0 is the main magnetic field, e.g. 3T, $\gamma\mathbf{G} \cdot \mathbf{r} = 2\pi\mathbf{k} \cdot \mathbf{r}$ is the imaging gradient, and $b(\mathbf{r})\omega_0$ is a susceptibility field scaled to the main magnetic field.

Eq. 2.8 becomes Eq. 2.10 with 1) Eq. 2.9, 2) the assumption that the main magnetic field is much greater than the other fields, $\omega_0 \gg \gamma\mathbf{G} \cdot \mathbf{r} + b(\mathbf{r})\omega_0$, and 3) ω_0 modulation.

$$s \approx \int m(\mathbf{r}) m_{\perp}(\mathbf{r}) e^{-ib(\mathbf{r})\omega t} \cdot e^{-2\pi i\mathbf{k} \cdot \mathbf{r}} d^3\mathbf{r} \quad [2.10]$$

Note that $\omega_0 + \gamma\mathbf{G} \cdot \mathbf{r} + b(\mathbf{r})\omega_0 \approx \omega_0$ but $e^{-i\omega t} \neq e^{-i\omega_0 t}$ because $e^{-ib(\mathbf{r})\omega t}$ and $e^{-2\pi i\mathbf{k} \cdot \mathbf{r}}$ oscillate.

2.1.4 Signal in time with relaxation

Eq. 2.10 is the result from considering only precession as in Eq. 2.5. With taking the longitudinal and transverse relaxation, R_1 and R_2 into account, Eq. 2.5 can be generalized.

$$\frac{d\mathbf{m}}{dt} = \gamma\mathbf{m} \times \mathbf{B} - R_1(m_z - m_z^0)\hat{\mathbf{z}} - R_2(m_x\hat{\mathbf{x}} + m_y\hat{\mathbf{y}}) \quad [2.11]$$

Where m_z^0 the magnetization at thermal equilibrium.

Accordingly, Eq. 2.10 can be generalized with R_2 term from Eq. 2.11.

$$s(t) \approx \int m(\mathbf{r})e^{-R_2(\mathbf{r})t} e^{-ib(\mathbf{r})\omega_0 t} \cdot e^{-2\pi i \mathbf{k} \cdot \mathbf{r}} d^3\mathbf{r} \quad [2.12]$$

Eq. 2.12 can be approximated as Eq. 2.13 with the assumption that R_2 is much smaller the readout duration ($e^{-R_2(\mathbf{r})t} \approx e^{-R_2(\mathbf{r})TE}$) and the imaging gradient is much greater than the susceptibility induced field ($e^{-ib(\mathbf{r})\omega_0 t} \approx e^{-ib(\mathbf{r})\omega_0 TE}$).

$$s(t) \approx \int m(\mathbf{r})e^{-R_2(\mathbf{r})TE} e^{-ib(\mathbf{r})\omega_0 TE} \cdot e^{-2\pi i \mathbf{k} \cdot \mathbf{r}} d^3\mathbf{r} \quad [2.13]$$

Eq. 2.13 can be considered as the Fourier transform of a magnetization with amplitude attenuation ($e^{-R_2(\mathbf{r})TE}$) and phase dispersion ($e^{-ib(\mathbf{r})\omega_0 TE}$).

2.1.5 Signal in image domain

Eq. 2.13 is a signal intensity in time. Signal intensity in the image domain (at location \mathbf{r}) can be obtained with taking the inverse Fourier transform in terms of the imaging gradient \mathbf{k} and \mathbf{r} .

$$s(\mathbf{r}) \approx \int_{r-\frac{\Delta r}{2}}^{r+\frac{\Delta r}{2}} q(\mathbf{r} - \mathbf{r}') m(\mathbf{r}') e^{-R_2(\mathbf{r}')TE} e^{-ib(\mathbf{r}')\omega_0 TE} d^3\mathbf{r}' \quad [2.14]$$

Where $q(\mathbf{r} - \mathbf{r}')$ is voxel sensitivity function due to Fourier encoding, which assumes to be the

voxel box for simplicity. In addition, the average spin distribution, $\bar{m}(\mathbf{r}) = \int_{r-\frac{\Delta r}{2}}^{r+\frac{\Delta r}{2}} \frac{m(\mathbf{r}')}{\Delta V} d^3\mathbf{r}'$, can

be defined since the phase variation in the voxel dominates the integral. Then, Eq. 2.14 can be expressed as Eq. 2.15.

$$s(\mathbf{r}) \approx \bar{m}(\mathbf{r}) \cdot \Delta V \cdot e^{-R_2 TE} \cdot \int_{r-\frac{\Delta r}{2}}^{r+\frac{\Delta r}{2}} \frac{d^3 \mathbf{r}' m(\mathbf{r}')}{\Delta V \bar{m}(\mathbf{r})} e^{-ib(\mathbf{r}')\omega_0 TE} \quad [2.15]$$

This integral can be treated as a probability $\frac{d^3 \mathbf{r}' m(\mathbf{r}')}{\Delta V \bar{m}(\mathbf{r})} = p(b)db$ average of $e^{-ib\omega_0 TE}$. Eq. 2.15, then, becomes Eq. 2.16.

$$s(\mathbf{r}) \approx \bar{m}(\mathbf{r}) \cdot \Delta V \cdot e^{-R_2 TE} \cdot \langle e^{-ib\omega_0 TE} \rangle \quad [2.16]$$

Eq. 2.16 is identical to Eq. 2.1, the starting point of our QSM-based and qBOLD modeling.

2.2 Signal model to QSM-based and qBOLD modeling

2.2.1 QSM-based modeling

This chapter describes how QSM-based CMRO2 modeling, Eq. 1.3 in Chapter 1.1, can be obtained from the signal model, Eq. 2.16.

Eq. 2.16 can be further approximated by Cumulant expansion upto the 2nd order.

$$s(\mathbf{r}) \approx \bar{m}(\mathbf{r}) \cdot \Delta V \cdot e^{-R_2^* TE} \cdot e^{-i\langle b \rangle \omega_0 TE} \quad [2.17]$$

Where $R_2^* = R_2 + \frac{1}{2} \omega_0^2 TE (\langle b^2 \rangle - \langle b \rangle^2)$.

In QSM, $\langle b \rangle$ can be obtained voxel-wise, and approximated as dipole field, $b \approx d * \chi$ (Eq. 1.1).

Since the inversion from field (b) to source (χ) is ill-posed, a small amount of noise in b would induce a substantial artifact in χ . Bayesian approach can be employed to alleviate the issue (37).

Voxel-wise χ can be divided into blood contribution (related to venous oxygenation) and non-blood contribution (Eq. 1.3).

2.2.2 qBOLD modeling

This chapter explains how qBOLD modeling, Eq. 1.5 in Chapter 1.2, can be achieved from the signal model, Eq. 2.16.

The magnitude signal contribution of the average term in Eq. 2.16, $\langle e^{-ib\omega_0TE} \rangle$, can be modeled by using a priori assumption for b , not by taking Cumulant expansion. In qBOLD, b can be divided into two contributions: mesoscopic field (b_{messo}) and macroscopic field (b_{macro}). b_{messo} assumes to be caused by numerous long cylindrical sources and b_{macro} is approximated as a linearly varying field across a voxel. Then, Eq. 2.16 can be expressed as Eq. 2.18.

$$s(\mathbf{r}) \approx \bar{m}(\mathbf{r}) \cdot \Delta V \cdot e^{-R_2TE} \cdot \langle e^{-i(b_{messo}+b_{macro})\omega_0TE} \rangle \quad [2.18]$$

The scale of the mesoscopic field is much smaller than a voxel size, similar to vessel size (~ several microns). The field is caused by the susceptibility difference between deoxyhemoglobin in vein and the surrounding tissue. On the other hand, the macroscopic field scale is larger than a voxel size. The field arises from the susceptibility difference at air-tissue interfaces and different brain tissue boundaries. Since the two fields are in different scales, the probability distribution of the two fields may be approximated to be independent. Consequently, the signal contribution

$$\begin{aligned} \text{from } b_{messo} \text{ and } b_{macro} \text{ can be treated separately based on } \langle e^{-ib\omega_0TE} \rangle &= \int P_b e^{-ib\omega_0TE} \approx \\ \int P_{b_{messo}} \cdot P_{b_{macro}} e^{-i(b_{messo}+b_{macro})\omega_0TE} db_{messo} db_{macro} &\approx \int P_{b_{messo}} e^{-ib_{messo}\omega_0TE} db_{messo} \cdot \\ \int P_{b_{macro}} e^{-ib_{macro}\omega_0TE} db_{macro} &= \langle e^{-ib_{messo}\omega_0TE} \rangle \cdot \langle e^{-ib_{macro}\omega_0TE} \rangle. \end{aligned}$$

2.2.2.1 Singal contribution from the mesoscopic field

For b_{messo} singal modeling, vessels assume to be long cylinders uniformly filled with deoxyhemoglobin. The analytic field solution exists for the infinitely long cylindrical object (38).

$$b_{messo}(r) = \delta\omega_{\theta} \cdot \frac{R^2}{r^2} \cdot \cos 2\phi \quad [2.19]$$

Where $\delta\omega_{\theta}$ is the characterstic frequency shift for the cylinder (\hat{z}) titled from \mathbf{B}_0 by the angle θ , $\delta\omega_{\theta} = \gamma \cdot 2\pi \cdot (\chi_{cyl} - \chi_0)B_0 \sin^2 \theta$, χ_{cyl} is the susceptibility of cylindrical source, χ_0 is the susceptibility of medium, R is the radius of the cylinder, r is distance in x-y plane between the measuring point and the cylinder center, ϕ is polar angle in the x-y plane.

The mesoscopic field contributing to the GRE signal, F_{BOLD} , can be estimated by taking the average of $e^{-ib_{messo}\omega_0TE}$ over 1) the position of numerous cylinders with the assumption of random and independent distribution, 2) the cylinder radius (R), and 3) the cylinder orientation (θ) (32).

$$F_{BOLD}(Y, v, \chi_{nb}, t) = \exp[-v \cdot f_s(\delta\omega \cdot t)] \quad [2.20]$$

f_s is the signal decay by the blood vessel network (12,31) and $\delta\omega$ is the characteristic frequency due to the susceptibility difference between deoxygenated blood and the surrounding tissue (Eq 1.6).

2.2.2.2 Signal contribution from the macroscopic field

For b_{macro} singal modeling, b_{macro} is assumed to vary linearly across a voxel.

$$b_{macro}(r) = b_0 + g_x x + g_y y + g_z z \quad [2.21]$$

Where b_0 provides the average voxel phase, and g_x, g_y, g_z are the field gradient along each direction.

Then, the macroscopic field inhomogeneity contribution to the GRE signal, G , can be estimated via the voxel spread function (12,39,40). The gradient of the linear field and phase leads to the shift in voxel spread function.

$$G_n(TE) = \frac{\sum_m |S_m(TE_1)| \cdot e^{(-R_{2,m}^* + i\gamma b_m) \cdot TE} \cdot \prod_{j=1}^3 \eta_{nm,j}}{|S_n(TE_1)| \cdot e^{-R_{2,n}^* \cdot TE}} \quad [2.22]$$

where TE_1 is the first echo time, b_m is the average magnetic field in the voxel m , $\eta_{nm,j}$ is the voxel spread function (the contribution of voxel m to voxel n) in j th direction (x, y , and z):

$$\eta_{nm,j} = \sum_{q_j} \text{sinc} \left(q_j - q_{m,j}(TE) \right) \cdot e^{2\pi i \cdot q_j(n-m)} \text{ where } q_j = k_j \cdot a_j, q_{m,j} = \frac{(\gamma \cdot g_{m,j} \cdot TE + \phi_{m,j}) \cdot a_j}{2\pi},$$

$g_{m,j}$ and $\phi_{m,j}$ are the gradient of the background field and the first echo phase, respectively, and

k_j is k-space $\left(-\frac{1}{2a_j} + \frac{1}{N_j \cdot a_j}, -\frac{1}{2a_j} + \frac{2}{N_j \cdot a_j}, \dots, \frac{1}{2a_j} \right)$, N_j and a_j are matrix size and voxel size in

the j th direction, respectively.

CHAPTER 3

3 CMRO2 MAPPING BY COMBINING QSM AND QBOLD

3.1 Abstract

In this chapter, we combined a quantitative susceptibility mapping (QSM)-based CMRO2 method and quantitative blood oxygenation level dependent magnitude (qBOLD) to remove unnecessary assumptions in the individual models and to utilize both magnitude and phase information.

3.2 Introduction

Cerebral metabolic rate of oxygen (CMRO2) and oxygen extraction fraction (OEF) maps are valuable for evaluating neurologic disorders such as ischemic stroke (3,41). Quantitative MRI modeling have been proposed to estimate these maps either magnitude, e.g. qBOLD (10,11), or phase data, e.g. QSM (17-19).

There are several challenges to the current CMRO2 mapping methods. qBOLD approximates χ_{nb} from fully oxygenated blood (11,39), but it ignores tissue iron stored in ferritin or myelin that contributes to the rich χ_{nb} contrast in the brain. QSM-based methods assume a fixed and empirical linear relationship between the venous blood volume fraction (v) and cerebral blood flow (CBF) to obtain v (30), but this relationship may vary with tissues and diseases. While qBOLD estimates v directly from the data, it assumes that χ_{nb} is constant. On the contrary, QSM-based methods assume v from CBF, whereas χ_{nb} is estimated from the data. Since both methods use the same underlying mGRE data, we propose to combine QSM and qBOLD (QSM+qBOLD) to map the OEF and CMRO2 overcoming these assumptions.

3.3 Theory

CMRO2 ($\mu\text{mol}/100\text{g}/\text{min}$) and OEF (%) can be expressed as

$$CMRO2 = CBF \cdot OEF \cdot [H]_a \quad [3.1]$$

$$OEF = 1 - \frac{Y}{Y_a} \quad [3.2]$$

where CBF is the cerebral blood flow ($\text{ml}/100\text{g}/\text{min}$), $[H]_a$ is the oxygenated heme molar concentration in the arteriole ($7.377 \mu\text{mol}/\text{ml}$) estimated from $[H]_a = [H] \cdot Y_a$, where $[H] = 7.53 \mu\text{mol}/\text{ml}$ is the heme molar concentration in tissue blood assuming a hematocrit of $\text{Hct} = 0.357$ (18). Y_a and Y are the arterial (assumed to be 0.98) and venous oxygenation. Hct , Y , and Y_a are dimensionless fractions.

QSM-based CMRO2 methods estimate two unknowns per voxel (Eq. 1.4) (17-19): Y and χ_{nb} . The venous blood volume fraction (v) is assumed to be known by an empirically derived linear relationship between cerebral blood flow (CBF) and v (30). However, since this assumption may break down in disease such as stroke (42), v should be treated as a parameter estimated from data. The qBOLD-based CMRO2 method (12) expresses the magnitude of the GRE signal of each voxel as a function of four unknowns: S^0 , R_2 , v , and Y (Eq. 1.5) (10-12). qBOLD treats χ_{nb} , which varies spatially due to iron and myelin content, as the same as that of fully oxygenated blood. In the proposed QSM+qBOLD method, both v and χ_{nb} are treated as unknowns, and the QSM and qBOLD signal equations are combined according to maximum likelihood under Gaussian noise approximation (43). The maximum likelihood estimation finds the parameter set $(Y, v, \chi_{nb}, S^0, R_2)$ which maximizes the probability of observing the voxel-wise

susceptibility QSM and the magnitude signals $S(TE)$ assuming respective signal models $F_{QSM}(Y, v, \chi_{nb})$ and $F_{qBOLD}(Y, v, \chi_{nb}, S^0, R_2, TE)$. These signal models build upon prior QSM (18) and qBOLD models (12) but are modified to properly models v and χ_{nb} in Eqs. 1.4 and 1.5. Assuming Gaussian noise, this is equivalent to minimizing the cost function:

$$Y^*, v^*, \chi_{nb}^*, S^{0*}, R_2^* = \underset{Y, v, R_2, S_0, \chi_{nb}}{\operatorname{argmin}} \left\{ \begin{array}{l} w \|F_{QSM}(Y, v, \chi_{nb}) - \chi\|_2^2 + \\ \left\| S(t) - S_{qBOLD}(S_0, Y, v, R_2, \chi_{nb}, t) \right\|_2^2 \end{array} \right\} \quad [3.3]$$

where $\|\cdot\|_2$ is the L2 norm and w the weight on the QSM model of phase data. The first term is the QSM-based modeling of phase data, Eq. 1.4 (18,19). Note that v , which was estimated from CBF in QSM-based CMRO2 mapping methods (17-19), is now an unknown to be determined by data. The second term is the qBOLD model of magnitude data, Eq. 1.5 (12). Note that the qBOLD assumption of neglecting susceptibility differences between non-blood tissue and fully oxygenated blood ($\chi_{ba} = \chi_{nb}$) (10-12,33) is not made here.

This QSM+qBOLD model is compared with two previous methods: 1) QSM method with minimum local variance (MLV) (18) (“QSM” hereafter), and 2) qBOLD that models the complex multi-echo gradient echo data as (12) (“qBOLD” hereafter):

$$S(TE) = S^0 \cdot e^{-R_2 \cdot TE} \cdot e^{i\Delta f \cdot TE} \cdot F_{BOLD}(v, Y, \chi_{ba}, TE) \cdot G(TE) \quad [3.4]$$

3.4 Methods and Materials

3.4.1 Data Acquisition

This study was approved by the local Institutional Review Board. Healthy volunteers were recruited (n=11; 10 males, 1 female, mean age 34 ± 12 years) for brain MRI on a 3T scanner (HDxt, GE Healthcare) using an 8-channel brain receiver coil. After obtaining consent, all subjects were instructed to avoid caffeine or alcohol intake 24 hours prior to the MRI.

MRI was performed in the resting state (19) using a 3D fast spin echo (FSE) arterial spin labeling (ASL) sequence (44-46), a 3D multi-echo spoiled gradient echo (GRE) sequence (22,47,48), and an inversion prepared T1w SPGR sequence (BRAVO) (49). The 3D FSE ASL sequence parameters were: 20 cm field of view (FOV), 1.56 mm in-plane resolution, 3.5 mm slice thickness, 1500 ms labeling period, 1525 ms post-label delay, 976.6 Hz/pixel bandwidth, spiral sampling of 8 interleaves with 512 readout points per leaf, 35 axial slices, 10.1 ms TE, 4533 ms TR, and 3 signal averages. The 3D GRE sequence parameters were: 0.78 mm in-plane resolution, 1.2 mm slice thickness, volume coverage identical to the 3D FSE ASL sequence, 7 equally spaced echoes, 2.3 ms for the first TE, 3.9 ms echo spacing, 30.5 ms TR, 488.3 Hz/pixel band width, and 15° flip angle. The pulse sequence was flow-compensated in all three directions (47). The inversion prepared T1w SPGR sequence parameters were: 0.78 mm in-plane resolution, 1.2 mm slice thickness, volume coverage identical to the 3D FSE ASL sequence, 2.92 ms TE, 7.69 ms TR, 450 ms prep time, 195.2 Hz/pixel bandwidth, and 15° flip angle.

3.4.2 Image Processing

QSM reconstruction was performed as follows: first, an adaptive quadratic-fit of the GRE phase was used to estimate the total field (47). Second, the Projection onto dipole fields (PDF) method was used to obtain the local field (48). Finally, the Morphology Enabled Dipole Inversion

(MEDI) algorithm was used to compute susceptibility (21,22,50). The susceptibility values were referenced to the susceptibility of cerebrospinal fluid (CSF) averaged over a manually drawn ROI on the first echo of the GRE acquisition. CBF maps (ml/100g/min) were generated from the ASL data using the FuncTool software package (GE Healthcare, Waukesha, WI, USA). All images were co-registered and interpolated to the resolution of the QSM maps using the FSL FLIRT algorithm (51,52).

3.4.3 Optimization

To improve convergence behavior during nonlinear fitting, the five unknowns $v, Y, \chi_{nb}, S^0, R_2$ were scaled to have roughly the same order of magnitude as the initial guess: $x \mapsto \frac{x}{|x_0|}$, where x is the unknown in the original scale and x_0 is the corresponding initial guess. Initial guesses were obtained as follows: Y_0 was estimated from the straight sinus (SS) as the global constraint in previous QSM-based CMRO2 studies (18,19), $Y_0 = Y_a \cdot (1 - OEF_{ss}/Hct_{ratio})$ where Hct_{ratio} is the hematocrit ratio (0.759) between large vessels and brain tissue (24) and $OEF_{ss} = 1 - Y_{ss}/Y_a$ (Y_{ss} was estimated from QSM in SS with setting $\psi_{Hb} = 0.1197$ for large veins (18,25,26), $v = 1$ and $\chi_{nb} = 0$ in Eq. 1.4). v_0 was set using the linear relationship between CBF and v (17-19). $\chi_{nb,0}$ was set as the susceptibility of fullyoxygenated blood as in the qBOLD methods (10-12). S_0^0 and $R_{2,0}$ were obtained by performing a mono-exponential fit against Eq. 1.5 after fixing the values of G (39) and F_{BOLD} with the initial values $Y_0, v_0,$ and $\chi_{nb,0}$. The function G was calculated using the voxel spread function (VSF) method (40). For some voxels the initials guess for Y was not appropriate leading to an increase in signal as a function of TE

after dividing out the F_{BOLD} contribution. This then led to a negative $R_{2,0}$. To avoid this situation, Y was gradually increased to insure a positive $R_{2,0}$.

To speed up the F_{BOLD} calculation, we used a Taylor expansion of ${}_1F_2$ up to the 60th order (12). The lower and upper bounds were set to 0.5 and 2 for each scaled unknown, except for Y , which used the 0.1 and 0.9 bounds before scaling. At the start of each optimization, both the QSM and qBOLD terms in Eq. 3.3 were normalized by their respective values evaluated with the initial guess to compensate for the arbitrary scale of input MRI data. The tuning parameter w was selected using the L-curve method (53). Corners of the L-curves for two randomly chosen subjects were both located at $w = 100$ (Figure 3.1). The limited-memory Broyden-Fletcher-Goldfarb-Shanno-Bound (L-BFGS-B) algorithm was used for the constrained optimization (54,55). The optimization was stopped when the relative residual $r_i = \frac{E_i - E_{i-1}}{E_i}$, with E_i as the energy of the i th iteration, was smaller than 0.005.

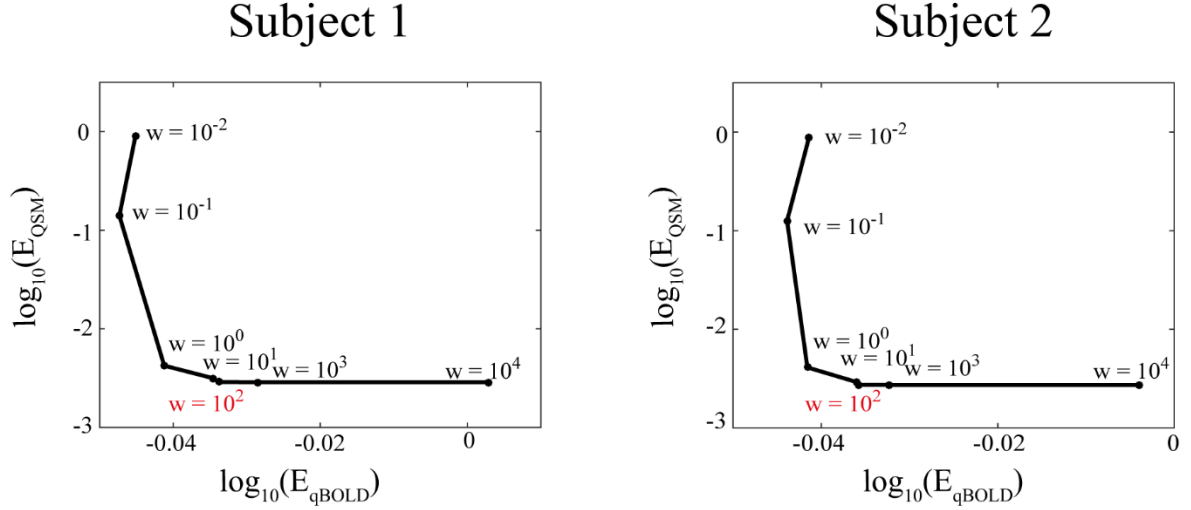


Figure 3.1. L-curve analysis.

Performed in two randomly selected subjects to determine tuning parameter w . The L-curve corners were located at $w=100$ in both subjects. E_{qBOLD} and E_{QSM} indicate the energy terms in

Eq. 3.3.

For “QSM”, the optimization followed the previous QSM-based method using the MLV method and global CMRO2 constraint (18). For “qBOLD”, the optimization was performed voxel-wise, following (12). The parameter scaling, initial guess, and boundary conditions were set in the same manner as for QSM+qBOLD. In addition, the initial frequency shift Δf_0 was set to the total field value as obtained in the QSM process (22).

3.4.4 Statistical Analysis

ROI analyses (mean and standard deviation), paired t-tests (at 0.01 significance level), and Bland-Altman analyses were performed to compare CMRO₂ and OEF values between the QSM-based (18), qBOLD (12), and QSM+qBOLD methods. For the ROIs, the bilateral anterior (ACA), middle (MCA) and posterior (PCA) cerebral artery vascular territories (VT) in the cortical gray matter (CGM) and white matter (WM) masks were constructed based on T1-weighted images by a neuroradiologist with 10 years of experience.

3.5 Results

The CMRO₂ in CGM were 140.4 ± 14.9 , 134.1 ± 12.5 , 184.6 ± 17.9 $\mu\text{mol}/100\text{g}/\text{min}$ (N=11) for the QSM, qBOLD, and QSM+qBOLD models, respectively. These corresponded to OEFs of $30.9 \pm 3.4\%$, $30.0 \pm 1.8\%$, $40.9 \pm 2.2\%$, respectively.

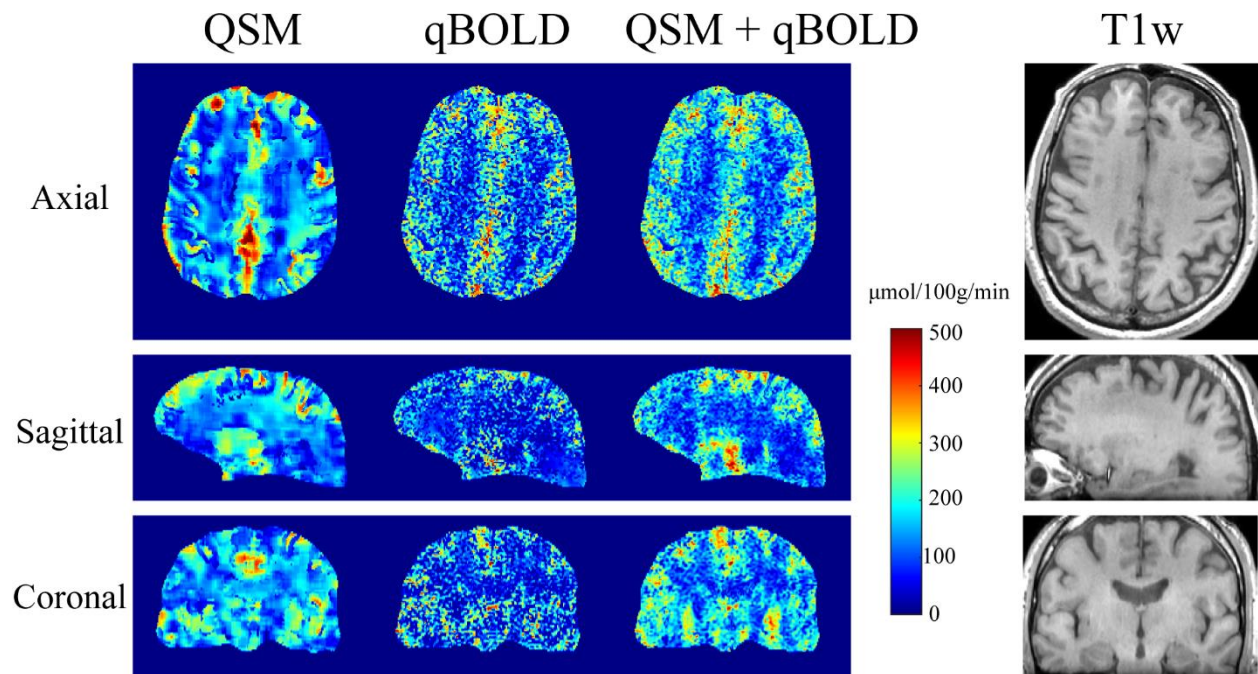


Figure 3.2. CMRO2 maps in axial, sagittal, and coronal sections.

A healthy subject reconstructed using QSM, qBOLD, and QSM+qBOLD methods. The corresponding T1-weighted anatomical images are shown on the right. QSM+qBOLD shows higher GM/WM contrast than QSM or qBOLD.

In Figure 3.2, compared to QSM and qBOLD, QSM+qBOLD showed higher CMRO2 contrast between CGM and WM: 21.9 ± 9.4 ($p < 0.01$), 36.0 ± 6.4 ($p < 0.01$), 54.6 ± 10.3 $\mu\text{mol}/100\text{g}/\text{min}$ ($N=11$) for the QSM, qBOLD, and QSM+qBOLD models, respectively. QSM showed a smoother CMRO2 map than QSM+qBOLD, except for a sharp transition at the GM/WM boundary.

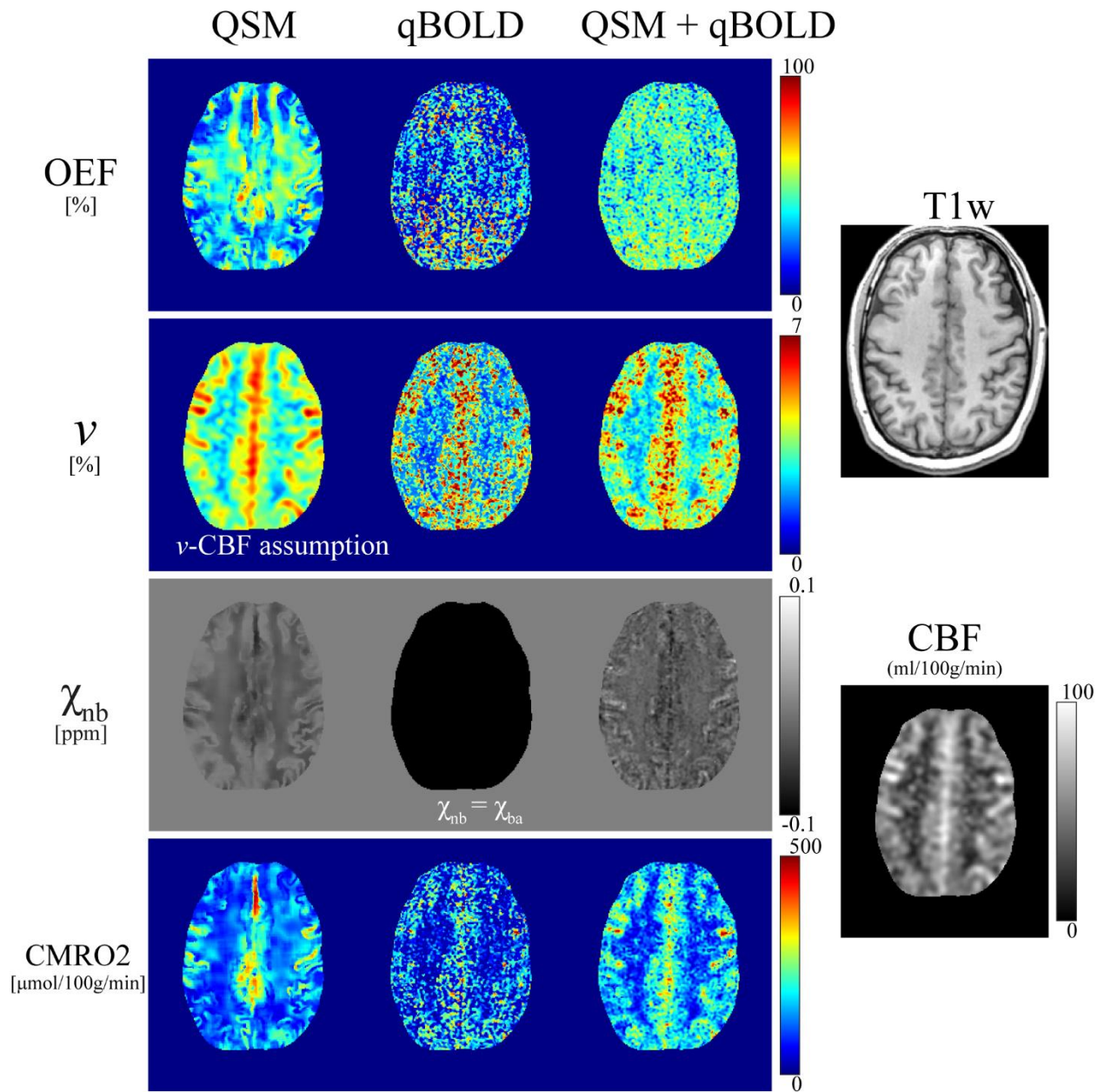


Figure 3.3. OEF, v , χ_{nb} , and CMRO2 maps.

A second subject reconstructed using QSM, qBOLD, and QSM+qBOLD models. The OEF obtained using QSM+qBOLD is more uniform than that of QSM, and is greater than that of qBOLD.

In Figure 3.3, QSM+qBOLD showed higher OEF than the two individual methods; the OEF values for whole brain were $34.5 \pm 3.1 \%$ ($p < 0.01$), $29.8 \pm 2.1 \%$ ($p < 0.01$), and $39.3 \pm 2.2 \%$ ($N=11$) for QSM, qBOLD, and QSM+qBOLD, respectively. QSM+qBOLD showed a relatively uniform OEF map as compared to QSM, and a less noisy OEF map than qBOLD. The OEF standard deviations in CGM was lower for QSM+qBOLD than for each individual methods: $16.3 \pm 0.9 \%$ ($p < 0.01$), $19.4 \pm 1.5 \%$ ($p < 0.01$), and $12.3 \pm 1.2 \%$ ($N=11$) for QSM, qBOLD, and QSM+qBOLD, respectively. The venous blood volume v was slightly higher for QSM+qBOLD as compared to QSM and qBOLD: in CGM, the values were $4.3 \pm 0.4 \%$ ($p < 0.01$), $4.1 \pm 0.4 \%$ ($p < 0.01$), and $4.5 \pm 0.4 \%$, and in WM, $3.5 \pm 0.3 \%$ ($p = 0.011$) and $3.2 \pm 0.3 \%$ ($p < 0.01$), and $3.5 \pm 0.3 \%$ for QSM, qBOLD and QSM+qBOLD, respectively. χ_{nb} from QSM and QSM+qBOLD showed similar contrast at the CGM/WM boundary, it was higher in CGM than in nearby WM. Average χ_{nb} values were similar between QSM and QSM+qBOLD as compared to qBOLD (-108.3 ppb assumed for the whole brain): -12.3 ± 3.7 ppb ($p < 0.01$) and -19.8 ± 3.5 ppb in CGM, and -15.3 ± 3.9 ppb ($p < 0.01$) and -18.7 ± 3.5 ppb in WM ($N=11$) for QSM and QSM+qBOLD, respectively. The v map of the QSM model and the χ_{nb} of the qBOLD model were not obtained through optimization, but given by a priori assumptions.

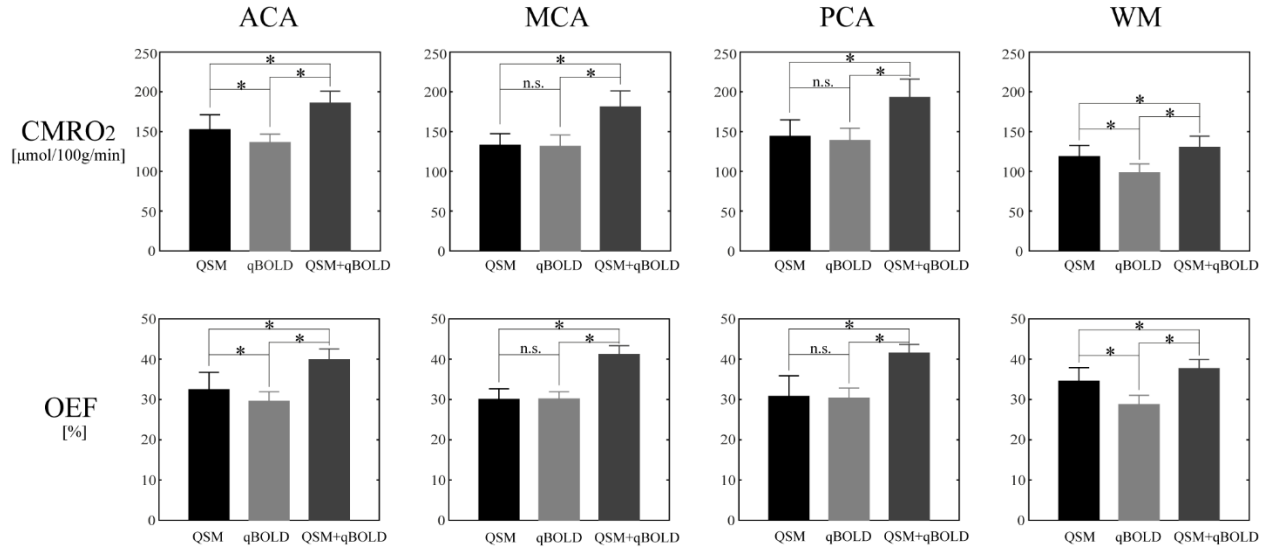


Figure 3.4. ROI comparisons.

CMRO2 and OEF in ACA, MCA, PCA, and WM among QSM (black), qBOLD (gray), and QSM+qBOLD (dark gray). In all ROIs, QSM+qBOLD provides higher CMRO2 and OEF values than QSM or qBOLD ($p < 0.01$). * $p < 0.01$ (paired t -test). "n.s." indicates that the difference is not significant ($p > 0.1$).

In Figure 3.4, QSM+qBOLD showed higher CMRO2 and OEF values than both QSM and qBOLD in all ACA, MCA, PCA, and WM ROIs ($p < 0.01$). All three methods showed lower CMRO2 in WM than in ACA, MCA, and PCA ($p < 0.01$).

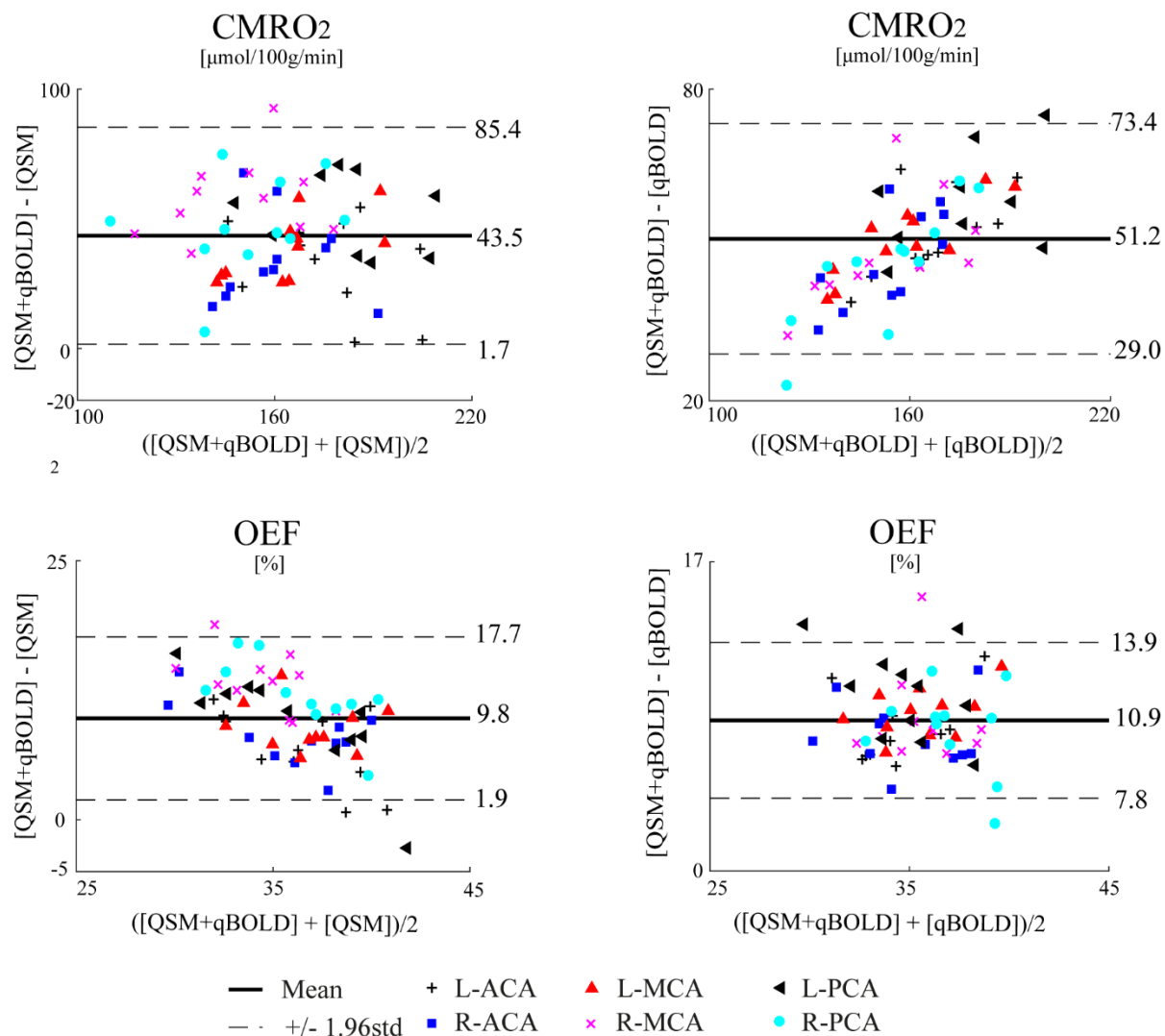


Figure 3.5. . Bland-Altman plots.

Comparison of OEF and CMRO2 values in VT ROIs between QSM+qBOLD and the two reference methods, QSM and qBOLD. The mean differences are $43.5 \mu\text{mol}/100\text{g}/\text{min}$ (QSM vs QSM+qBOLD) and $51.2 \mu\text{mol}/100\text{g}/\text{min}$ (qBOLD vs QSM+qBOLD) for CMRO2 ($p < 0.01$), and 9.8% (QSM vs QSM+qBOLD) and 10.9% (qBOLD vs QSM+qBOLD) for OEF ($p < 0.01$).

In the Bland-Altman plots (Figure 3.5), the mean differences were 43.5 $\mu\text{mol}/100\text{g}/\text{min}$ (QSM vs QSM+qBOLD) and 51.2 $\mu\text{mol}/100\text{g}/\text{min}$ (qBOLD vs QSM+qBOLD) for CMRO2 ($p<0.01$), and 9.8 % (QSM vs QSM+qBOLD) and 10.9 % (qBOLD vs QSM+qBOLD) for OEF ($p<0.01$).

3.6 Discussion

Our results demonstrate the feasibility of a QSM+qBOLD method for mapping CMRO2 by comprehensive modeling of both the magnitude and phase of multi-echo gradient echo data. When either QSM modeling phase or qBOLD modeling magnitude are used individually to estimate CMRO2, a number of assumptions are required: a linear relationship between CBF and v and the minimum local variance of the estimated parameters within a tissue block for the QSM-based method (18), and constant non-blood tissue susceptibility for the qBOLD method (11,12). These assumptions may cause errors and are eliminated in the proposed QSM+qBOLD method.

Compared to QSM and qBOLD alone, the proposed QSM+qBOLD shows clearer GM/WM CMRO2 contrasts (Figure 3.2), more uniform OEF compared to QSM (Figure 3.3), and better agreement with results presented using other independent CMRO2 estimation methods such as positron emission tomography (PET) (56). By overcoming the limited availability of PET, MRI provides greater accessibility for patient studies. Without any vascular challenge, QSM+qBOLD can be readily applied to study damage to vital organs caused by oxygen-deficiency, including Alzheimer's disease (AD) (57,58), multiple sclerosis (59,60), and ischemia in stroke (41,61).

Compared to qBOLD, QSM+qBOLD shows higher OEF (Figures. 3.3, 3.4, and 3.5), with $39.3 \pm$

2.2 % for the whole brain; this is in a good agreement with results from previous PET studies which have OEFs of 35 ± 7 % (62), 42.6 ± 5.1 % (63), 41 ± 6 % (64), and 40 ± 9 % (65). This difference is not driven by venous blood volume (v), which was found to be similar between qBOLD and QSM+qBOLD (Figure 3.3). Instead, the higher OEF may be explained by the inclusion of non-blood tissue susceptibility (χ_{nb}) as a variable, which, in qBOLD, is assumed to be equal to the susceptibility of fully oxygenated blood (χ_{ba}). The resulting χ_{nb} (-19.8 ± 3.5 ppb in CGM) is greater than χ_{ba} (-108.3 ppb). To obtain the same measured susceptibility difference $\delta\omega$ in Eq. 1.6 when $\chi_{ba} - \chi_{nb} < 0$, the venous oxygenation Y needs to decrease, which leads to a higher OEF (Equations 1.6 and 3.2). This suggests that inclusion of χ_{nb} was a factor in the observed OEF increase.

QSM+qBOLD shows higher OEF average than QSM for whole brain (39.3 ± 2.2 % vs 34.5 ± 3.1 %). A likely cause of this may lie in the use of the global constraint in QSM (18), which is not used in QSM+qBOLD. The global constraint from straight sinus (SS) might not precisely estimate the average oxygenation in the whole brain because SS may not represent all the draining veins (66,67) that are known to have considerable variation, e.g. 47.7% ~ 75.3% (68).

At the GM/WM boundary in the CMRO2 map, the QSM method shows a sharp transition, whereas the QSM+qBOLD method reveals a gradual change (Figures 3.2 and 3.3). The sharp GM/WM edge in QSM may be caused by separate optimization for the GM and WM (18); in the QSM+qBOLD method, the optimization was performed for whole brain. The CMRO2 GM/WM contrast in QSM+qBOLD is primarily driven by CBF since OEF map looks fairly uniform (Figure 3.3). A lack of CMRO2 GM/WM contrast in QSM is not uniform and more prominent in areas where OEF appears underestimated (Figure 3.3, top and bottom left). Errors in GM/WM

segmentation or smoothing by the MLV assumption may have caused these local underestimations.

The CMRO2 and OEF maps are smoother using the QSM method (Figures 3.2 and 3.3). This may be caused by the use of MLV in the QSM method (18), which assumes that CMRO2 and χ_{nb} are constant within small blocks of brain tissue, to overcome the underdetermined system (2 unknowns and 1 equation per voxel) when no challenge is used. The MLV assumption in the QSM method is highly dependent on the block setting, e.g. block size and number of block shifts. The QSM+qBOLD model eliminates this MLV assumption using qBOLD modeling of the magnitude data.

The non-blood tissue susceptibility χ_{nb} shows a clear GM/WM contrast using QSM+qBOLD (Figure 3.3). This is consistent with the difference in myelin content between CGM and WM (69).

The QSM+qBOLD model may still be affected by residual limitations in QSM and qBOLD models. The qBOLD term ignores the detailed microstructure of brain tissue, including myelin water components and magnetic anisotropy of myelin in white matter. The qBOLD Eq. 1.5 may be expanded with 2 different R_2 s to account for myelin water, and fiber orientation dependent effects in Eq. 1.6 to consider myelin magnetic anisotropy. The empirical L-curve analysis was used to determine relative weighting (w) in Eq. 3.3. Additional studies are needed to investigate the influence of the weighting w , measurement error and differences in acquisition schemes. For instance, the propagation of bias and error in the estimated susceptibility into QSM+qBOLD measurements will depend on the choice of w . Spatial resolution will play a role in the choice of

w : while smaller voxels typically improve QSM estimates (18), the resulting signal to noise ratio (SNR) loss may affect qBOLD estimates negatively, since it requires high SNR (11).

While QSM+qBOLD removed the linear CBF/CBV assumption in QSM and the constant non-blood tissue susceptibility assumption in qBOLD, it retains a constant ratio between venous and total blood volume (0.77), constant tissue hematocrit (0.357) and constant oxygenated heme molar concentration in the arteriole ($7.377 \mu\text{mol/ml}$) for the whole brain, which may vary among subjects and diseases. The ASL-measured CBF is known to contain errors, particularly in WM (70) and maybe deteriorated with the usage of shorter post-label delay in this study (1525 ms as used in the clinical protocol at our institution) than the recommended value of 2000 ms (45), which will propagate to CMRO₂. The OEF and v estimation in large veins might be errorous because they were treated in the same way as normal brain tissue. This error could be suppressed using the $v = 1$ prior for large veins. The QSM+qBOLD optimization (Eq. 3.3) is non-convex, with convergence susceptible to dependency on solver implementation, initial guesses, parameter scaling, and stopping criterion. A reference standard such as ¹⁵O PET is needed to validate CMRO₂ methods. Finally, the application of this method and its validation for a general patient population remains to be investigated.

3.7 Conclusion

Our study demonstrated the feasibility of a comprehensive quantitative CMRO₂ mapping method by combining QSM and qBOLD-based methods. In healthy subjects, the CMRO₂ map obtained with QSM+qBOLD shows better GM/WM contrast as compared to an individual QSM or qBOLD-based method, while the OEF map appeared more uniform compared to the QSM-based method.

CHAPTER 4

4 CLUSTER ANALYSIS OF TIME EVOLUTION FOR QSM+QBOLD

4.1 Abstract

In this chapter, we introduce cluster analysis of time evolution (CAT) to improve the robustness of quantitative susceptibility mapping plus quantitative blood oxygen level-dependent magnitude (QSM+qBOLD or QQ) against noise.

4.2 Introduction

In previous chapter, QSM and qBOLD (QSM+qBOLD=QQ) have been combined to model the effect of OEF on the magnitude and phase of multi-echo gradient echo (mGRE) data (34). This QQ approach enables OEF and CMRO₂ mapping without vascular challenges that are difficult to administer in clinic practice. However, QQ remains challenging, because qBOLD with a strong coupling between venous oxygenation (Y) and venous blood volume (v) is very difficult to invert (11). The qBOLD inversion is highly sensitive to noise, and susceptible to substantial errors in OEF at typical signal-to-noise (SNR) levels (11,71).

We introduce here a cluster analysis of time evolution (CAT) method to overcome the noise sensitivity of QQ-based OEF by improving the effective SNR (35). The basic idea of the CAT method is that voxels with a similar mGRE signal evolution have similar model parameter values and that the number of clusters as determined by machine learning is much smaller than the number of voxels. Consequently, averaging over a cluster can substantially increase SNR for a cluster-wise inverse solution that can be used as a robust initial guess for voxel-wise QQ

optimization. In this study, QQ-based OEF and CMRO2 with and without CAT (34) were compared in simulations, healthy subjects and ischemic stroke patients.

4.3 Theory

Due to the non-linear nature of Eq. 1.5, qBOLD-based OEF estimates are highly dependent on initialization and SNR (71). To increase the effective SNR, we propose a novel Cluster Analysis of Time evolution (CAT) method for QSM+qBOLD (“QQ with CAT” hereafter). This method is based on the following insights. Voxels with similar signal time-course $S_{qBOLD}(t)/G(t)$ have similar tissue parameters (Y, v, R_2). Many voxels have very similar signal time-courses and form a cluster for an effective signal averaging or SNR improvement (72). K-means clustering can be used to identify these clusters (73). The QQ problem is solved first with a cluster-wise optimization by assuming parameters Y, v , and R_2 to be constant within each cluster while S_0 and χ_{nb} are allowed to vary from voxel to voxel, since the magnitude and phase signals depend predominantly on S_0 and χ_{nb} , respectively. Next, a voxel-wise optimization is performed by using the solution from the cluster-wise optimization as the initial guess.

QQ is formulated as:

$$Y^*, v^*, R_2^*, S_0^*, \chi_{nb}^* = \underset{Y, v, R_2, S_0, \chi_{nb}}{\operatorname{argmin}} \left\{ \begin{array}{l} w \|F_{QSM}(Y, v, \chi_{nb}) - \chi\|_2^2 + \\ \left\| S(t) - S_{qBOLD}(S_0, Y, v, R_2, \chi_{nb}, t) \right\|_2^2 + \lambda (\overline{OEF(Y)} - OEF_{wb})^2 \end{array} \right\} \quad [4.1]$$

where w is the weighting on the QSM term. The first term is the QSM-based modeling of phase data, Eq. 1.4 (18,19). The second term is the qBOLD model of magnitude data, Eq. 1.5 (12).

The third term used the physiological constraint that the OEF averaged over the brain, $\overline{OEF(Y)}$, should be similar to OEF_{wb} , the brain OEF value estimated from the main draining vein, the straight sinus: $OEF_{wb} = Hct_{vt} \cdot OEF_{ss}$ where $Hct_{vt} = 0.759$ is the hematocrit ratio between large vessels (24) and brain tissue, and $OEF_{ss} = 1 - Y_{ss}/Y_a$ with Y_{ss} estimated from the average susceptibility in the straight sinus with $\psi_{Hb} = 0.1197$ (25,26,34), $v = 1$ and $\chi_{nb} = 0$ in Eq. 1.4. In Eq. 4.1, $S(t)$ is the measured mGRE data, and λ the regularization strength.

4.4 Methods and Materials

4.4.1 Numerical Simulation 1

To investigate the relationship between SNR and the dependency of OEF on the initial guess, we performed a simulation. The mGRE and susceptibility values were simulated using Eqs. 1.4 and 1.5, respectively. The input (ground truth) was $Y = 60\%$, $\chi_{nb} = -0.1$ ppm, $S_0 = 1000$ au, and $R_2 = 20$ Hz. For the v input, two v values were used: 3% (Case 1) and 1% (Case 2). The same echo times are used as in the healthy subjects ($TE_1/\Delta TE/TE_7 = 2.3/3.9/25.8$ ms). Gaussian noise was added to the mGRE signals and the QSM values to obtain SNR ∞ (no noise), 1000, 100, and 50. For each SNR, the optimization was subsequently performed to estimate Y with different initial guesses for $Y(0.15,0.3,0.45,0.6,0.75,0.9)$ and $v(0.01,0.03,0.05,0.07)$. The ground truth was used for the initial guesses of S_0 , χ_{nb} and R_2 . This was repeated for 500 times for each SNR. $w=5 \times 10^{-3}$ and $\lambda = 0$. A relative error was computed as $\frac{|\overline{Y_{result}} - Y_{true}|}{|Y_{true}|}$.

4.4.2 Numerical Simulation 2

To compare the accuracy of QQ with and without CAT (34), we performed a simulation. First, the mGRE signals and the QSM values for each brain voxel were simulated using Eqs. 1.4 and 1.5, respectively, using the same echo times as in the stroke patients (see below). The input (ground truth) was the result from QQ with CAT method in one stroke patient, who was imaged 6 days post onset (see below). The average OEF and v across the brain was 29% and 0.97%, respectively. Gaussian noise was added to the mGRE signals and the QSM values to obtain SNR ∞ (no noise), 1000, 100, and 50. For each SNR, the simulated data was processed in two ways: 1) QQ without CAT, with a constant OEF initial guess for the whole brain (34) and 2) QQ with CAT. The same optimization, including $w = 5 \times 10^{-3}$ and $\lambda = 10^3$, was performed as in experimental data (see below). OEF_{wb} was set to the average ground truth OEF across the brain (29 %). Root-mean-square error (RMSE) was calculated to measure accuracy.

4.4.3 Data Acquisition

Healthy subjects: This study was approved by the local Institutional Review Board. Healthy volunteers were recruited (n=11; 10 males, 1 female, mean age 34 ± 12 years) for brain MRI on a 3T scanner (HDxt, GE Healthcare) using an 8-channel brain receiver coil. After obtaining consent, all subjects were instructed to avoid caffeine or alcohol intake 24 hours prior to the MRI. MRI was performed in the resting state (15) using a 3D fast spin echo (FSE) arterial spin labeling (ASL) sequence (31-33), a 3D spoiled mGRE sequence (13,34,35), and an inversion prepared T1w SPGR sequence (BRAVO) (36). The 3D FSE ASL sequence parameters were: 20 cm FOV, 1.56 mm in-plane resolution, 3.5 mm slice thickness, 1500 ms labeling period, 1525 ms post-label delay, 976.6 Hz/pixel bandwidth, spiral sampling of 8 interleaves with 512 readout points per leaf, 35 axial slices, TE=10.1 ms, TR=4533 ms, and 3 signal averages. The 3D mGRE

sequence parameters were: 0.78 mm in-plane resolution, 1.2 mm slice thickness, volume coverage identical to the 3D FSE ASL sequence, 7 equally spaced echoes: $TE_1/\Delta TE/TE_7 = 2.3/3.9/25.8$ ms, TR= 30.5 ms, bandwidth 488.3 Hz/pixel and flip angle 15° . The pulse sequence was flow-compensated in all three directions (34). The inversion prepared T1w SPGR sequence parameters were: 0.78 mm in-plane resolution, 1.2 mm slice thickness, volume coverage identical to the 3D FSE ASL sequence, TE=2.92ms, TR=7.69 ms, 450 ms prep time, bandwidth 195.2 Hz/pixel, and flip angle 15° .

Stroke patients: MRI was performed in 5 ischemic stroke patients using 3D ASL, 3D mGRE, DWI on a clinical 3T scanner (GE MR Discovery 750) using a 32-channel brain receiver coil. The time interval between stroke onset and MRI examination ranged between 6 hours and 12 days. All lesions were located in unilateral cerebral artery territory. The 3D FSE ASL sequence parameters were: 24 cm FOV, 1.9 mm in-plane resolution, 2.0mm slice thickness, 1500 ms labeling period, 1525 ms post-label delay, 976.6 Hz/pixel bandwidth, 68 axial slices, TE=14.6 ms, TR=4787 ms, and 3 signal averages. The 3D mGRE sequence parameters were: 0.47mm in-plane resolution, 2mm slice thickness, volume coverage identical to the 3D FSE ASL sequence, 8 equally spaced echoes: $TE_1/\Delta TE/TE_8 = 4.5/5/39.5$ ms, TR= 42.8 ms, bandwidth=244.1 Hz/pixel, and flip angle 20° . DWI sequence parameters were: 24 cm FOV, 0.94 mm in-plane resolution, 3.2 mm slice thickness, 1953.1 Hz/pixel bandwidth, 0, 1000 s/mm^2 b-values, TE=71 ms, TR=3000 ms, and 4 signal averages.

4.4.4 Image Processing

Healthy subjects: QSM reconstruction was performed as follows: first, an adaptive quadratic-fit of the mGRE phase was performed to estimate the total field (47). Second, the Projection onto dipole fields (PDF) method was used to obtain the local field (48). Finally, the Morphology Enabled Dipole Inversion with automatic uniform cerebrospinal fluid zero reference (MEDI+0) algorithm was used to compute susceptibility (21,22,50,74). CBF maps (ml/100g/min) were generated from the ASL data using FuncTool (GE Healthcare, Waukesha, WI, USA). All images were co-registered and interpolated to the resolution of the QSM maps using the FSL FLIRT algorithm (51,52).

Stroke patients: QSM and CBF processing was the same as in the healthy subjects, except a linear-fit of the mGRE phase was used to estimate the total field as 3D flow-compensation was not available on the scanner used in the patient studies.

4.4.5 Clustering

The mGRE magnitude signal $S(t)$ was used for clustering after the macroscopic field inhomogeneity contribution, G was removed. For the purpose of clustering, the mGRE signal for each voxel was normalized by the average signal across echoes. The K-means clustering algorithm using the squared Euclidean distance (75-78) was then applied to cluster voxels with similar normalized signal evolution across echoes. Conventional K-means clustering requires an a priori choice of the number of clusters, denoted by K . Here, we used the X-means method (79) that automatically selects K . In this method, two operations are repeated iteratively. In Step 1, a conventional K-means clustering with a given initial number of clusters is performed and the Bayesian Information Criterion (BIC) measure is computed (80), which is the sum of the

clustering log-likelihood and a penalty on K . As K increases, goodness of fitting (log-likelihood) increases, but the possibility of overfitting also increases. The penalty term on K reduces this possibility. In Step 2, the centroid (the center of mass) for each cluster is replaced by two *child* centroids, and a local K-means ($K = 2$) is performed within that cluster using those child centroids as initial guesses. In order to decide whether each cluster should be replaced by the two obtained child clusters, the BIC is computed for this cluster: a larger BIC indicates a replacement is desired, otherwise the ‘parent’ centroid is kept. Steps 1 and 2 are repeated until the overall BIC stops increasing or until K reaches an a priori set maximum. In this study, 1 and 50 was used for the initial and maximum number of clusters, respectively.

For speed, the X-means algorithm to obtain the optimal number of clusters K was carried out on 10% of the total voxels, randomly selected. This process was repeated 10 times and the K with the largest BIC value among the 10 trials was selected. The corresponding centroids were then used as the initial centroids for the final K-means on all voxels.

4.4.6 Optimization

The QSM+qBOLD (QQ) optimization (Eq. 4.1) was solved by iteratively solving the following subproblems: 1) updating S_0 based on qBOLD (Eq. 4.2); 2) updating χ_{nb} based on QQ optimization (Eq. 4.3) χ , and 3) updating the Y, v, R_2 values based on QQ optimization (Eq. 4.4). Concretely, in the k th step, the subproblems are:

$$S_0^{k+1} = \underset{S_0}{\operatorname{argmin}} \left\| S(t) - S_{qBOLD}(S_0, Y^k, v^k, R_2^k, \chi_{nb}^k) \right\|_2^2 \quad [4.2]$$

$$\chi_{nb}^{k+1} = \underset{\chi_{nb}}{\operatorname{argmin}} \left\{ \begin{array}{l} w \|F_{QSM}(Y^k, v^k, \chi_{nb}) - \chi\|_2^2 \\ + \|S(t) - S_{qBOLD}(S_0^{k+1}, Y^k, v^k, R_2^k, \chi_{nb})\|_2^2 \end{array} \right\} \quad [4.3]$$

$$Y^{k+1}, v^{k+1}, R_2^{k+1} = \underset{Y, v, R_2}{\operatorname{argmin}} \left\{ \begin{array}{l} w \|F_{QSM}(Y, v, \chi_{nb}^{k+1}) - \chi\|_2^2 + \\ \|S(t) - S_{qBOLD}(S_0^{k+1}, Y, v, R_2, \chi_{nb}^{k+1})\|_2^2 + \lambda(\overline{OEF}(Y) - OEF_{wb})^2 \end{array} \right\} \quad [4.4]$$

Eq. 4.2 was solved using closed form expressions, while Eqs. 4.3 and 4.4 were solved iteratively. First, Y, v, R_2 were initialized as follows: Y_0 was estimated from OEF_{wb} in Eq. 4.1. The straight sinus mask was obtained automatically using global and regional thresholding on QSM combined with positional (inferior, posterior brain) and geometrical (straightness of the vein) constraints. For initial guesses for v (v_0), the whole brain was roughly segmented into three parts, gray matter (GM), white matter (WM), and cerebral spinal fluid (CSF) with either T1w (11 healthy subjects and 4 stroke patients) or T2-FLAIR image (1 stroke patient without T1w image) via FSL FAST (81). v_0 was set to 3/1.5/1% for GM/WM/CSF, respectively based on literature (10,11). $\chi_{nb,0}$ was set to satisfy Eq. 1.4 with Y_0 and v_0 . The initial guess $S_{0,0}$ and $R_{2,0}$ were obtained by solving Eq. 1.5, and using Y_0, v_0 and $\chi_{nb,0}$. The resulting mono-exponential fit was performed using ARLO (82). Before fitting, 3D Gaussian smoothing (standard deviation of 0.5 of the diagonal length of the voxel) was performed on S and G to improve SNR. Voxels with $R_2 > 100$ Hz or $R_2 < 2.5$ Hz were considered as outliers and removed from all subsequent processing.

Second, using the resultant clusters obtained in the Clustering section, a cluster-based optimization was performed, in which the unknowns Y, v, R_2 were assumed to be constant within each cluster. The average of the $Y_0, v_0, R_{2,0}$ across each cluster was used as the initial value for that cluster. To improve convergence behavior during non-linear fitting, the unknowns

Y, v, χ_{nb}, R_2 were scaled to have roughly the same order of magnitude: $x \mapsto \frac{x}{c}$, where x is the unknown in the original scale, c is the scaling factor: 0.5, 0.05, $|\chi_{nb,0}|$, $avg(R_{2,0}) + 4 \cdot SD(R_{2,0})$ for Y, v, χ_{nb}, R_2 , respectively. $avg(R_{2,0})$ and $SD(R_{2,0})$ denote the average and standard deviation of $R_{2,0}$ in the cluster, respectively. Lower and upper bounds were set to 0.0 and 0.98 for Y (before scaling), $0.4v_0$ and $2v_0$ for v (before scaling), 0.5 and 1.5 for R_2 (after scaling). For χ_{nb} , the lower and upper bounds were set to the value χ_{nb} calculated from Eq. 1.4 with $Y/v = 0.98/0.1$ and $0.0/0.1$, respectively. The optimization was performed on all clusters jointly. To compensate for the scale of the input MRI data, the qBOLD term in Eq. 4.3 and 4.4 was normalized by $\overline{|S(TE_1)|}^2 \cdot N_{voxel} \cdot N_{TE}$ where $\overline{|S(TE_1)|}$ is the average of the magnitude of the first echo across the whole brain, N_{voxel} the number of voxels, and N_{TE} the number of echoes. The QSM term in Eq. 4.3 and 4.4 was also normalized by $\|\chi\|_2^2$. The regularization weighting factor (λ) and the weighting on the QSM (w) were chosen by performing L-curve analysis (53): λ was first chosen with $w = 0$, then w was chosen with the previously decided λ . The limited-memory Broyden-Fletcher-Goldfarb-Shanno-Bound (L-BFGS-B) algorithm was used for the constrained optimization (54,55). The optimization was stopped when the relative residual $r_{k,n} \stackrel{\text{def}}{=} \frac{E_{k,n} - E_{k,n-1}}{E_{k,n-1}}$, with $E_{k,n}$ the energy of the n th iteration at the k th step, was smaller than 10^{-5} for Eqs. 4.3 and 4.4. For the k th step, the optimization was stopped when $\rho_k \stackrel{\text{def}}{=} \frac{E_{k,n_k} - E_{k-1,n_{k-1}}}{E_{k-1,n_{k-1}}} < 10^{-3}$ with n_k the number of L-BFGS-B iterations at step k after convergence. To prevent L-BFGS-B from not updating the Hessian when the residual falls below a preset threshold, the cost function was multiplied by a factor of 10^4 before L-BFGS-B was started.

Third, voxel-wise QQ optimization was performed using L-BFGS-B, allowing Y , v , and R_2 to vary from voxel to voxel. The cluster-based result was used as initial guess. The scaling was the same as the cluster-wise optimization. The lower and upper bounds were set to 0.7 and 1.3 of the initial guesses. The optimization was stopped when $r_{k,n} < 2 \times 10^{-4}$ for Eqs 4.3 and 4.4, and $\rho_k < 10^{-2}$.

For Numerical Simulation 1, the same optimization settings were used as for experimental data, except for the fixed lower and upper bounds for v , 0.01 and 0.1 before scaling.

QQ with CAT method was compared with QQ without CAT, which uses a constant initial guess OEF for the whole brain (34). For QQ without CAT, we followed the optimization described in (34). The weight on QSM (w) was set to 100 for healthy subjects and stroke patients based on L-curve analysis. The optimization was stopped when the relative residual was smaller than 0.005 for healthy subjects and 0.001 for the stroke patients.

All algorithms were implemented in Matlab R2016a (Mathworks Inc., Natick, MA). All the clustering and optimization were carried out with an Intel Core i7-6900K 3.2 GHz processor.

The computation time of the clustering, cluster-wise and voxel-wise optimization were 2.7 ± 0.7 mins, 3.3 ± 0.7 mins, and 4.6 ± 1.1 mins respectively for the 11 healthy subjects (10^6 voxels and 7 echoes), and 8.8 ± 2.5 mins, 8.8 ± 1.6 mins, 7.6 ± 1.2 mins respectively for the 5 stroke patients (1.8×10^6 voxels and 8 echoes). The code used for the experiments in this work, upon this paper publication, will become available for download from <https://med.cornell.edu/mri>.

4.4.7 Statistical Analysis

ROI analyses (mean and standard deviation) and paired t-tests were performed to compare CMRO₂ and OEF values between QQ with and without CAT. For the ROIs in the healthy subjects, cortical gray matter (CGM) masks were constructed based on T1-weighted images by an experienced neuroradiologist (S.Z. 7 years of experience). For the stroke patients, ROIs for the lesion and its corresponding contralateral side were drawn based on DWI by the same neuroradiologist. To investigate the dependency on the number of clusters, conventional K-means was performed with $K=1,5,10,15, 20$, and the X-means result. QQ with CAT was subsequently performed for each K . The same optimization scheme was used as in experimental data including $w/\lambda = 5 \times 10^{-3}/10^3$. To investigate the OEF difference among different K values, a repeated measures ANOVA was performed.

4.5 Results

In the optimal number of clusters determined by X-means, the difference between the 10% sub-sampling scheme and 100% sampling was on average <1 in 11 healthy subjects and 5 stroke patients (N=16). The 10% sub-sampling scheme (including the 10 trials) was 5~10 times faster than 100% sampling. The optimal number of clusters by the X-means method was 10 ± 2 in healthy subjects (N=11) and 16 ± 0 in stroke patients (N=5).

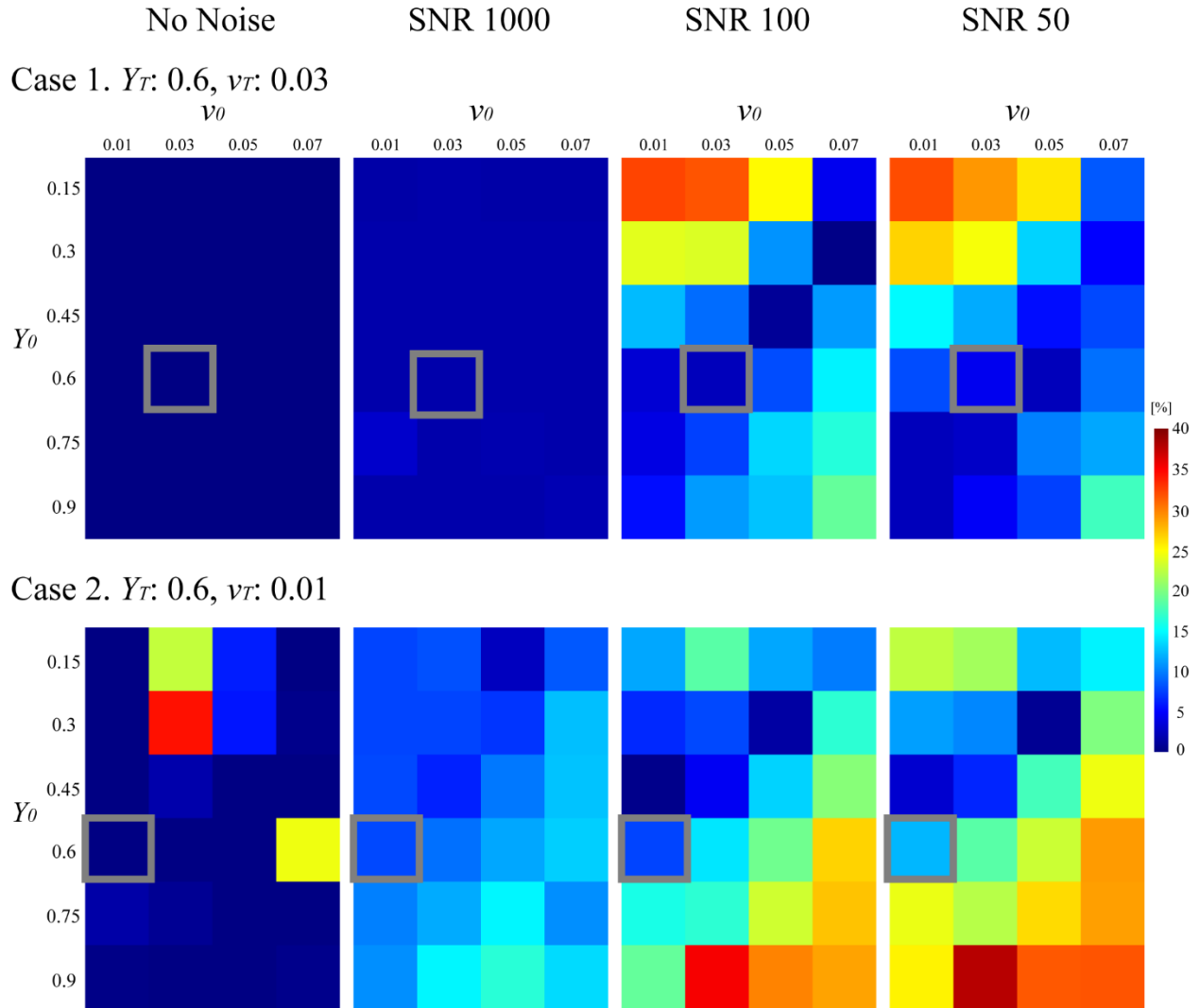


Figure 4.1. Influence of SNR on the estimated Y (Numerical Simulation 1).

Shown is the relative error between the estimated Y and the ground truth (Y_T). Y_0 and v_0 are the initial guesses of Y and v , respectively. As SNR decreases, Y becomes increasingly more sensitive to the initial guess, resulting in larger errors when the initial guess is away from the ground truth value. This seems more severe in the case with smaller v : $v_T = 0.03$ (Case 1) vs.

0.01 (Case 2). The gray box indicates the ground truth values (Y_T and v_T).

In the L-curve analysis, the corners for 4 randomly chosen subjects (2 healthy subjects and 2 stroke patients) were located at $\lambda = 10^3$ and $w = 5 \times 10^{-3}$. Figure 4.1 shows the influence of SNR on the sensitivity of the estimated Y on the initial guess (Numerical Simulation 1). Without noise, the relative error was low, but as SNR decreased from 1000 to 50, the relative error tended to increase when the initial guess deviated from the ground truth. For instance, at SNR 50 in Case 1, the relative error was 7.5% when $Y_0 = 0.6$ and $v_0 = 0.03$, but it was 29.1 % when $Y_0 = 0.15$ and $v_0 = 0.03$.

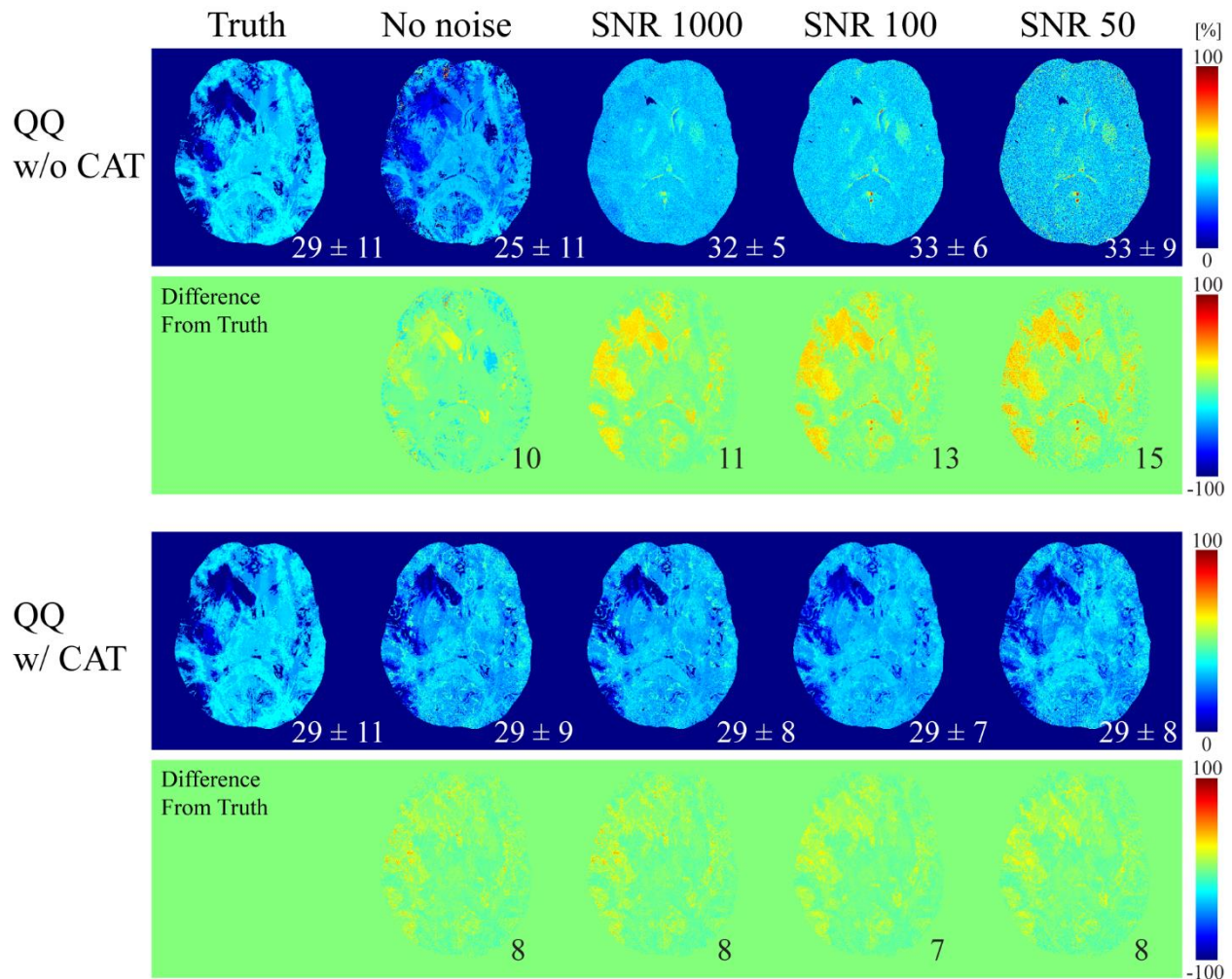


Figure 4.2. Comparison between QQ w/o and w/ CAT (Numerical Simulation 2).

At all SNRs, QQ with CAT captures low OEF values, whereas QQ without CAT is not sensitive to low OEF values at low SNRs. The numbers in white indicate the OEF average and standard deviation in the whole brain, and black represents the root-mean-square error (RMSE).

Figure 4.2 shows the comparison of the OEF maps obtained using QQ with and without CAT in the simulated stroke brain (Numerical Simulation 2). QQ with CAT provided a more accurate

OEF map than that without CAT, especially at low SNRs. For instance, at SNR 50, QQ with CAT captured the low OEF region, whereas QQ without CAT did not accurately depict low OEF values. QQ with CAT provided lower RMSE than QQ without CAT for all SNRs.

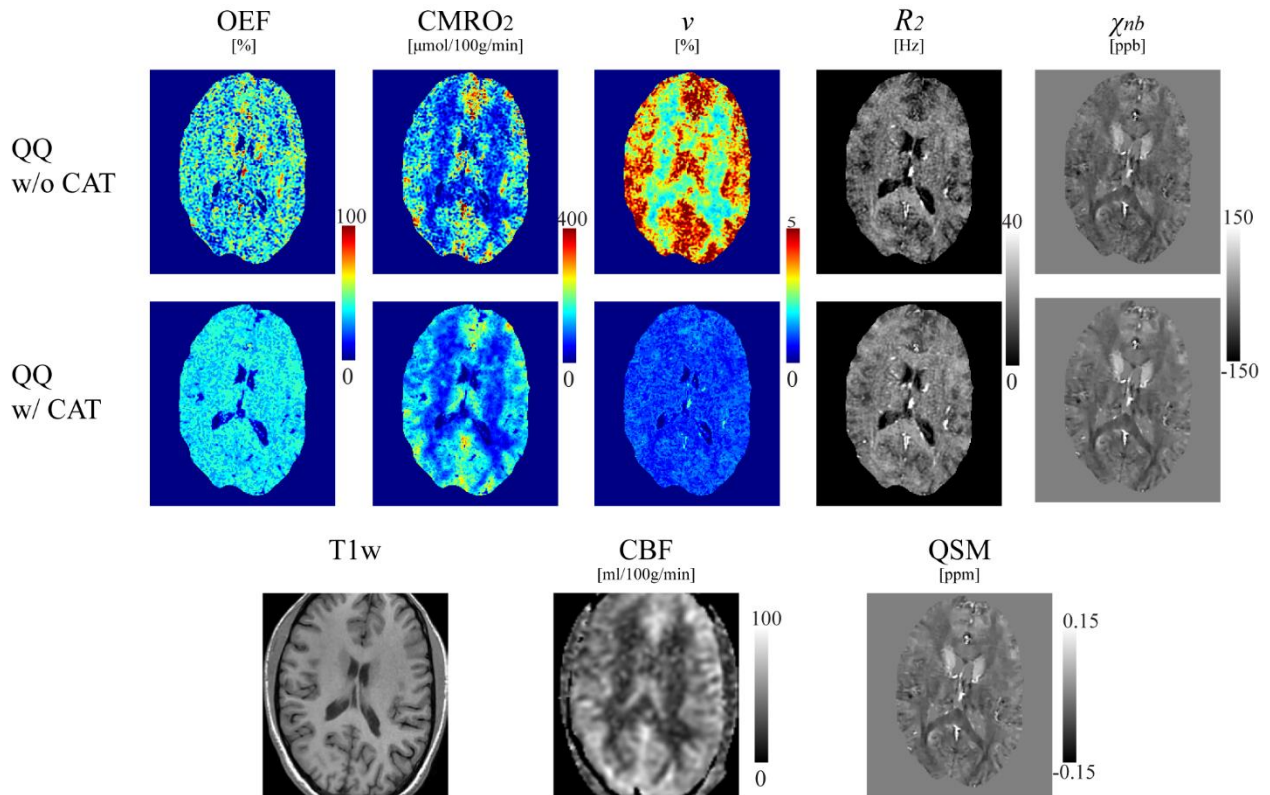


Figure 4.3. Parameter maps between QQ w/o and w/ CAT (healthy subject).

QQ with CAT shows a less noisy and more uniform OEF, and a good CMRO2 contrast between cortical gray matter and white matter without extreme values. The corresponding anatomy as depicted on a T1-weighted image, CBF map and susceptibility map are shown for reference.

Figure 4.3 shows a comparison between QQ with and without CAT in a healthy subject. The OEF with CAT appeared less noisy and more uniform, whereas OEF without CAT was noisy and had extreme values, for example $>80\%$ in deep gray matters. QQ with CAT showed a good CMRO₂ contrast between CGM and WM without extreme values seen in QQ without CAT. v showed CGM/WM contrast and generally had lower values than QQ without CAT.

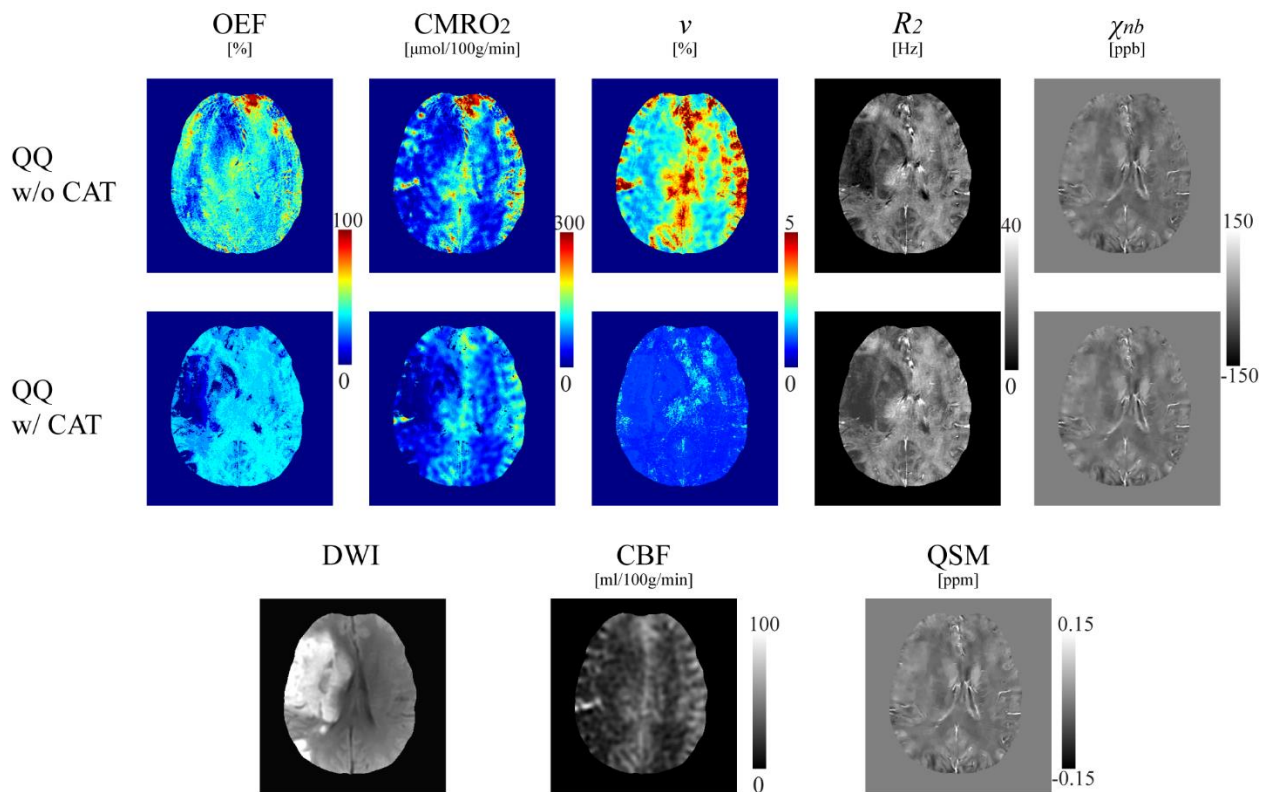


Figure 4.4. Parameter maps between QQ w/o and w/ CAT (6 d post onset).

In the CMRO2 and OEF maps, the lesion can be distinguished more clearly with QQ with CAT. For QQ with CAT, a low OEF region is clearly visualized and contained within the lesion region as defined on DWI, but a low OEF region obtained with QQ without CAT is not as well localized nor contained within the lesion as defined on DWI. QQ with CAT generally shows lower v in the DWI-defined lesion. The contrast in v in QQ without CAT result is similar in appearance to that of CBF. QQ with CAT shows generally higher R_2 and χ_{nb} maps.

Figure 4.4 shows the OEF, CMRO2, v , R_2 , and χ_{nb} maps in one stroke patient (6 days post stroke onset) using QQ with and without CAT. In the OEF and CMRO2 maps, the lesion was distinguished more clearly using QQ with CAT than without. A low OEF region was clearly contained within the lesion as defined on DWI. However, QQ without CAT did not show a clearly localized low OEF region, neither within nor outside of the DWI-defined lesion. QQ with CAT generally showed low v regions specific to the DWI defined lesion, while QQ without CAT showed similar v contrast to that of CBF. QQ with CAT generally had higher R_2 and χ_{nb} .

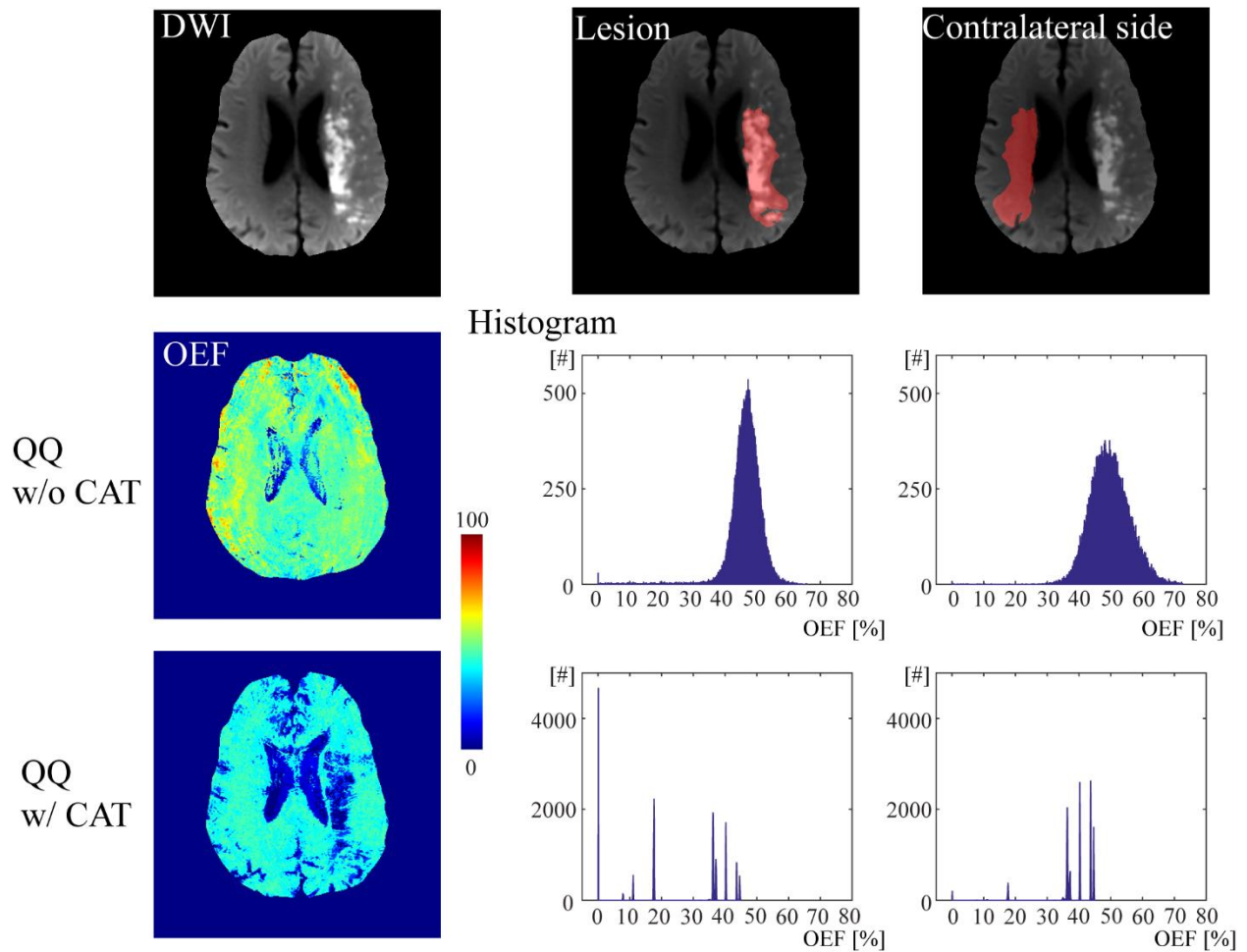


Figure 4.5. OEF histogram in the lesion and its contralateral side (12 d post onset).

QQ with CAT shows a different distribution in the lesion as compared to mirror side. The lesion shows 8 peaks with the strongest two peaks at 0 and 17.5%, while the contralateral side has 6 peaks with dominant peaks at 35 ~ 45%. However, QQ without CAT does not have a distribution specific to low OEF values in the lesion, but there are bell-shaped distributions for both the lesion and contralateral side (broader in the contralateral side) with peaks at 47% and 49%, respectively.

Figure 4.5 shows an OEF histogram in the lesion and in its contralateral region for both QQ with and without CAT in a second stroke patient (12 days post stroke onset). The OEF with CAT was distributed differently in the lesion as compared to the contralateral side. The lesion showed 8 peaks with the strongest two peaks at 0 and 17.5%, while the contralateral side had 6 peaks with dominant peaks at 35 ~ 45%. However, QQ without CAT did not have a distribution specific to low OEF values in the lesion, but there were bell-shaped distributions for both the lesion and contralateral side (broader in the contralateral side) with peaks at 47% and 49%, respectively.

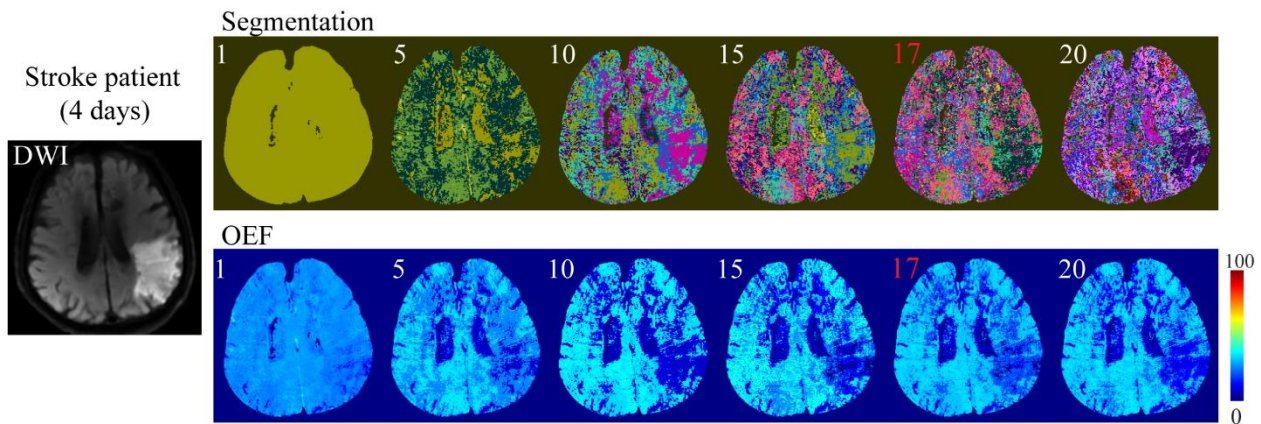


Figure 4.6. The segmentations and resultant OEF maps.

A different number of clusters ($K = 1, 5, 10, 15, 20$, as well as the X-means result, 17 indicated in red) was used in a third stroke patient (4 d post stroke onset). In the segmentations, different colors indicate different clusters. The resulting OEF appearance is nearly constant for $K \geq 5$.

Figure 4.6 shows the segmentations and resulting OEF maps for a range of cluster numbers in a third stroke patient (4 days post stroke onset). The resultant OEF maps had a similar appearance for all K larger than 5, and were not significantly different: $p=0.9999$, $F(5, 8520050)=0.0164$ (repeated measures ANOVA). The X-means selected $K = 17$.

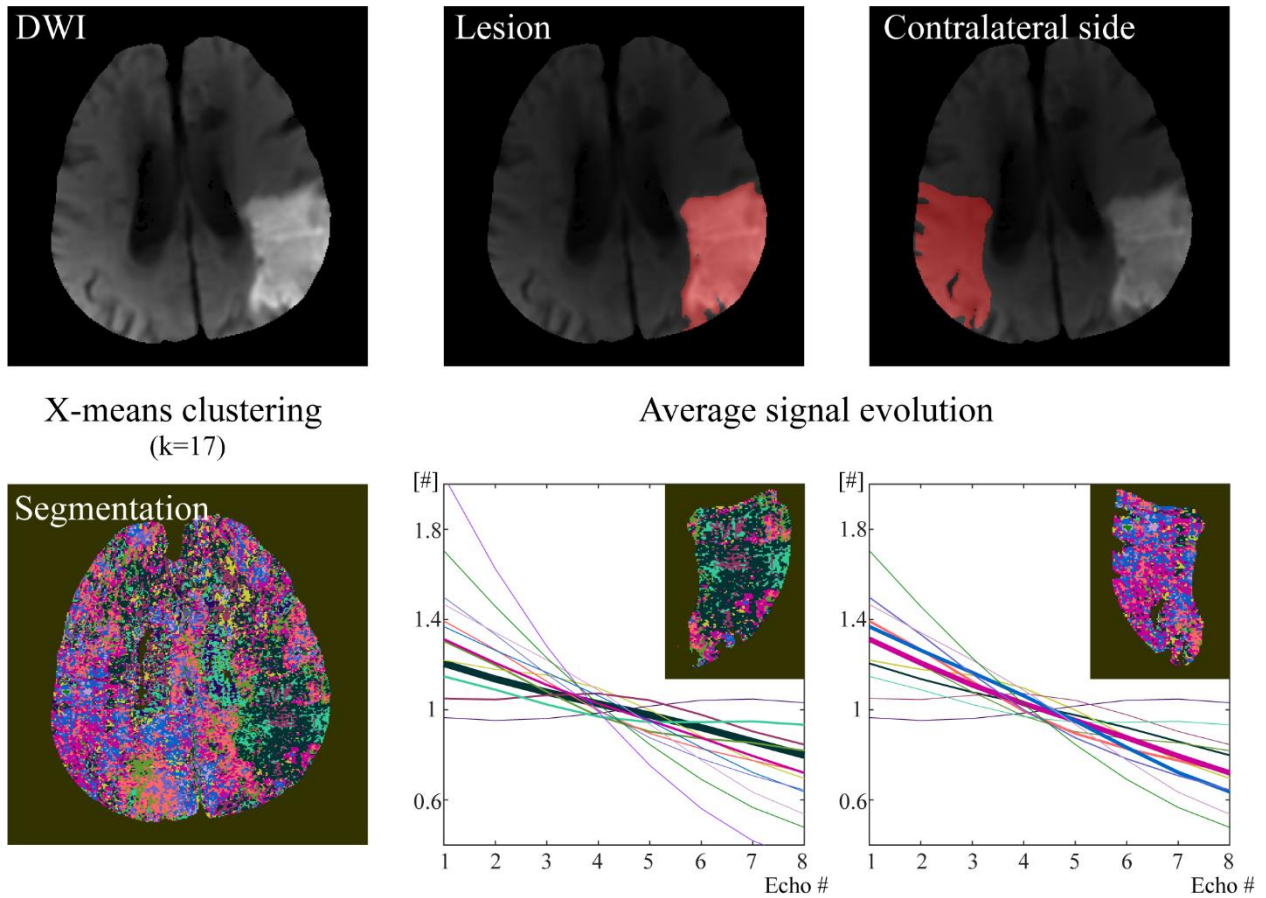


Figure 4.7. X-means clustering ($K = 17$) and the average signal evolution.

In the third stroke patient (4 d post stroke onset), different color indicates different cluster in the segmentation map. The corresponding average signal evolution was shown in the same color as

the cluster color. The width of the signal evolution is proportional to the number of voxels within clusters in the lesion and the contralateral side: The thicker the curve is, the more voxels the corresponding cluster has. For each voxel, the signal evolution was normalized by the average signal across echoes after the macroscopic field inhomogeneity contribution, G was removed. The average of these normalized signal evolutions across each cluster is shown here in different colors.

Figure 4.7 shows the X-means clustering result ($K = 17$) and the average signal evolution for each clusters in the third stroke patient (4 days post stroke onset). The lesion and the contralateral side had distinctively different dominant clusters: green clusters in the lesion and blue and pink clusters in the contralateral side. The corresponding average signal evolution was also different between the lesion and contralateral side.

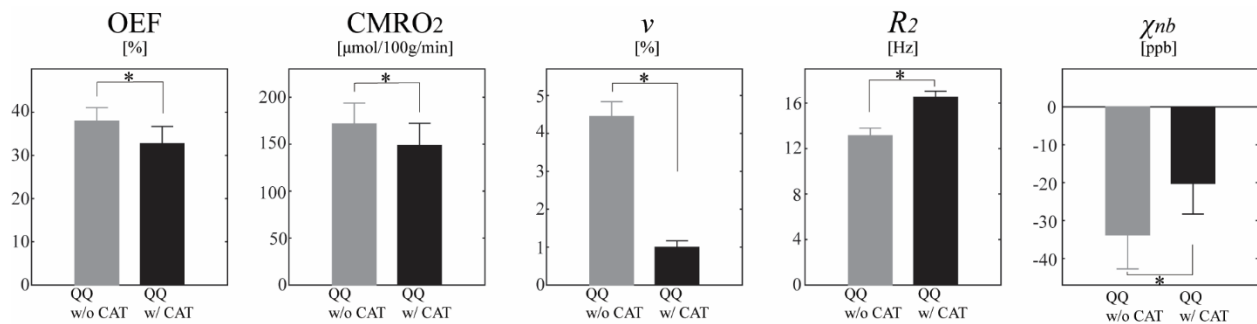


Figure 4.8. ROI analysis.

*Average and standard deviation of OEF, CMRO2, v , R_2 , and χ_{nb} maps between QQ without and with CAT in cortical gray matter from healthy subjects (N=11). QQ with CAT shows smaller average CMRO2, OEF and v than the one without CAT, but QQ with CAT shows higher average R_2 and χ_{nb} values. * $p < 0.01$ (paired t-test).*

Figure 4.8 shows the ROI analysis in the CGM of healthy subjects using QQ with and without CAT. QQ with CAT showed smaller OEF, CMRO2 and v than QQ without CAT (N=11): OEF was 32.7 ± 4.0 % and 37.9 ± 3.1 % ($p < 0.01$), CMRO2 was 148.4 ± 23.8 and 171.4 ± 22.4 $\mu\text{mol}/100\text{g}/\text{min}$ ($p < 0.01$), v was 1.00 ± 0.2 % and 4.45 ± 0.39 % ($p < 0.01$). Meanwhile, QQ with CAT showed higher R_2 and χ_{nb} values than QQ without CAT: R_2 was 16.5 ± 0.5 Hz and 13.1 ± 0.7 Hz ($p < 0.01$), χ_{nb} is -20.2 ± 8.1 ppb and -33.8 ± 9.0 ppb ($p < 0.01$).

4.6 Discussion

Our results indicate that the cluster analysis of time evolution (CAT) substantially improves the robustness against noise of QSM+qBOLD (QQ) based mapping of OEF and CMRO2. Compared to QQ without CAT, the denoised OEF map demonstrates greater accuracy in simulations, appears more uniform in healthy subjects, and depicts a spatial pattern of low values within the DWI- defined ischemic lesions in stroke patients. Therefore, the CAT enables robust QQ-based OEF mapping from mGRE data alone without vascular challenges.

Clustering is an effective tool for dealing with noise in time-series data, as demonstrated in fMRI where the signal change is a very small percentage and very noisy (83,84). The echo-time series data of mGRE is stronger than fMRI time series. However, the QQ model is fundamentally

relying on the separation of deoxyheme in cylindrical geometries from other susceptibility sources diffusely distributed in tissue. Use of two field strengths may also help separation of superparamagnetic ferritin from paramagnetic deoxyheme (50), but this is impractical in a clinical setting. The difference between echo time-series of random cylinders and diffuse distribution in qBOLD is about 10% (12,32), which is stronger than the signal change in fMRI but fundamentally makes QQ inversion sensitive to noise. Clustering as in CAT promises to allow robust QQ-based OEF and CMRO₂ mapping in clinical practice.

Compared to QQ without CAT, OEF maps obtained using the proposed CAT method are more uniform and have less extreme values in healthy subjects (Figure 4.3), in agreement with previous PET studies (56,65). The suppressed noise is likely due to the use of cluster-wise optimization. Unknowns are assumed to be constant throughout the cluster, thereby creating an effective signal averaging. The simulations suggest that the resulting higher SNR makes the estimated parameters less sensitive to measurement noise. The overall noise reduction in Y and v also propagates into χ_{nb} and R_2 maps with noise reduction benefits, compared to QQ without CAT (Figure 4.3).

QQ with CAT shows smaller OEF values (Figure 4.3 and 4.8), e.g. 32.7 ± 4.0 % and 37.9 ± 3.1 % ($p < 0.01$) in CGM for QQ with and without CAT, respectively. The smaller OEF values in QQ with CAT are accompanied by higher R_2 , as compared to the one without CAT (16.5 ± 0.5 Hz vs. 13.1 ± 0.7 Hz). This can be explained by that for the same measured magnitude signal decay, OEF decreases if R_2 increases (Eqs. 1.5 and 1.6). Both OEF values with and without CAT fall within the range previously reported for OEF obtained using PET: 35 ± 7 % (62) and $40 \pm$

9 % (65), and with other MRI based techniques: 26 ± 2 % (5), 31.7 ± 6.1 % (85), 35 ± 4 % (7), and 38 ± 14 % (6).

QQ with CAT shows smaller v values in healthy subjects than QQ without CAT: 1.00 ± 0.2 % vs 4.45 ± 0.39 ($p < 0.01$) in CGM. Compared to PET and other MR techniques, the v from QQ with and without CAT is a bit smaller and larger, respectively: the v values obtained using PET, e.g. 1.9 ± 0.5 % (86) and 2.0 ± 0.2 % (87), and other MR techniques: 1.75 ± 0.13 % (10), 1.9 ± 0.5 2.46 ± 0.28 (88), 2.68 ± 0.47 % (29), 3.6 ± 0.4 % (89). Further studies are needed to investigate the cause of the lower v from QQ with CAT than literature, e.g. performing an experiment that the v truth is known. It is because the ground truth v has not been measured directly and different v estimation methods have their own assumptions to be verified (90). For instance, qBOLD methods set the non-blood tissue susceptibility (χ_{nb}) to be uniform in the whole brain with the fully oxygenated blood susceptibility equal to -108 ppb (10,29), however tissue iron and myelin would cause regional χ_{nb} variation. The gray matter χ_{nb} value in this study, -20.2 ppb, was higher than the χ_{nb} value assumed in qBOLD. The inclusion of QSM in QQ with the greater χ_{nb} value may lead to smaller v value to obtain the same QSM value (Eq. 1.4). Calibrated BOLD methods using gas-inhalation assumes that CBF and CMRO₂ remain constant during hyperoxia (91,92). However, CBF may decrease and/or CMRO₂ may increase during hyperoxia, which leads an v overestimation (90,91). The v values from the PET methods are the difference the between the total and arterial blood volume (86,87), which includes both venous and capillary blood. This may lead to larger v than the one in this study. The R_2 for CGM estimated with CAT, 16.5 ± 0.5 Hz, is greater than that without CAT, 13.1 ± 0.7 Hz; and both

values agree with the values calculated from other MR techniques, 14.9 ± 0.2 Hz (10), 15.1 ± 0.6 Hz (12), 17.1 ± 2 Hz (93).

In ischemic stroke patients, low OEF regions obtained by QQ with CAT are largely contained within the ischemic lesions defined by DWI (Figures 4.4 and 4.5). However, the OEF maps without CAT did not show the DWI lesion spatial pattern. The low v region with CAT generally agrees with the DWI lesion spatial pattern; this observation is consistent with the blood volume decrease in ischemic stroke lesions (94). In contrast, QQ without CAT utilized a constant OEF initial guess, and the v map contrast was similar to that of the CBF map (Figure 4.4). This indicates that the v result without CAT did not change much from the initial guess, which is based on the CBF through a phenomenological relationship (17-19).

In a patient imaged 12 days post stroke onset, QQ with CAT shows a distinctly different lesion OEF histogram compared to the contralateral region (Figure 4.5), including the strongest two peaks OEF at 0% and 17.5%, in addition to several peaks of high OEF at 35~45% that were similar to the contralateral normal OEF. The low OEF region may indicate dead tissue (OEF < 10%), while the high OEF region may represent salvageable tissue (35~45%). QQ without CAT did not show such low OEF values in the lesion. These results suggest that the use of CAT allows QQ to capture the low OEF values expected in stroke lesions.

While this work focuses on OEF and touches v , QQ also outputs R2 and χ_{nb} non-blood susceptibility maps that may provide additional biomedical values. The R2 value is reduced in ischemic regions, which is consistent with literature of elevated T2 values but is not clear in its clinical implication (95). On the other hand, χ_{nb} may be examined in QSM brain applications (96), though χ_{nb} may be difficult to interpret in white matter (97). Particularly in studies dominated by

tissue iron, including multiple sclerosis (60,98), cerebral cavernous malformation (99), and Parkinson's disease (100), it may be interesting to investigate disease effects on OEF (deoxyheme iron in blood) and non-blood (presumably dominated by tissue iron) separately.

There are limitations on using the proposed QQ with CAT. The proper number of clusters was chosen automatically by the X-means method. This is based on a well-known metric, BIC. However, the optimal number of clusters might be different when using a different metric such as the Akaike information criterion, or when using a different clustering method, such as hierarchical clustering (77,101). This might affect the resulting OEF map. However, in our study, the OEF map was not sensitive to the number of clusters (Figure 4.6) chosen for K-means clustering. Furthermore, the voxel-wise optimization was performed after the cluster-wise optimization, which may alleviate the consequences of the imperfect clustering. As this CAT QQ technique translates to applications in sick patients, motion compensation such as by navigators (102-104) may be employed for robustness. To improve CMRO₂ estimation accuracy, CBF measurement accuracy should be increased as well. The ASL-measured CBF used in this study has low spatial resolution and may not be accurate in WM (70). The robustness of the OEF estimation can be further improved by a short first echo time and a small echo spacing since the deviation from mono-exponential decay of extravascular MRI signal predominantly occurs in short TE range. OEF and v estimations in large veins might be inaccurate as they were treated in the same way as normal brain tissue, which could be mitigated by using $v = 1$ for large veins. This may be implemented by segmenting large veins, for example by thresholding the susceptibility map (68,105), similar to the segmentation of the straight sinus. QQ with CAT optimization is still non-linear, which means that convergence may be affected by the solver

implementation, parameter scaling, and stopping criterion. No ground truth or reference measurement was available. An O^{15} PET study on a PET-MR scanner would allow measuring accuracy in vivo.

4.7 Conclusion

Our study demonstrated the feasibility of the cluster analysis of time evolution (CAT) for QSM+qBOLD (QQ) in healthy subjects and in ischemic stroke patients by effectively improving SNR. In simulations, the proposed method was more accurate than QQ without CAT. QQ with CAT provides a less noisy and more uniform OEF in healthy subjects. In ischemic stroke patients, low OEF regions are contained with the stroke lesions defined on DWI. QQ with CAT may be readily applied to investigate tissue viability in various diseases, such as Alzheimer's disease (57,58), multiple sclerosis (59), tumor (106), and ischemic stroke (61).

CHAPTER 5

5 FUTURE DIRECTIONS AND CONCLUSION

5.1 Future directions

The proposed CAT provides the significantly improved accuracy of QQ. Next step would be to apply it to clinical settings, such as stroke and multiple sclerosis (MS). In addition, there is still room for methodological improvement for QQ. Lastly, CAT has not been validated. Future studies may involve with 1) clinical application of QQ, 2) further method improvement for QQ with deep learning algorithm, and 3) validation with independent MR methods or ^{15}O PET. Preliminary results are discussed in each chapter.

5.1.1 Clinical application of QQ

5.1.1.1 Clinical application in ischemic stroke

Ischemic stroke due to the blood flow impairment to the brain is one of the leading cause of mortality and morbidity all over the world (107). In ischemic stroke, defining ischemic penumbral tissue is critical because the intravenous thrombolysis and endovascular thrombectomy could be performed based on its pattern (108-110). The ischemic penumbra is conceptualized as an area with perfusion below a functional threshold (ischemic) but above a preservation threshold (not infarcted). In clinical practice, the penumbra is estimated as the mismatch between perfusion weighted imaging (PWI, indicating a functional threshold) and diffusion weighted imaging (DWI, indicating a preservation threshold). However, the PWI-DWI mismatch does not reliably depict

the penumbra, e.g. overestimated penumbral tissue size compared to the one defined by PET (111). On the other hand, OEF and CMRO₂ mapping are very useful for defining the ischemic penumbral tissue as they provide a direct measurement of tissue oxygen consumption.

The OEF maps in 30 ischemic stroke patients (5, 19, and 6 cases in acute, early subacute, and late subacute phase) was estimated as in (35). Figure 5.1. shows the OEF maps in six patients. In the acute phase, there is some mis-match between low OEF area and the DWI-defined lesion as yellow arrows indicate in 6 and 18 hours post onset. The tissue in the mis-match area might be salvable due to comparable OEF to contralateral side. However, there is little mis-match after 4 days post onset.

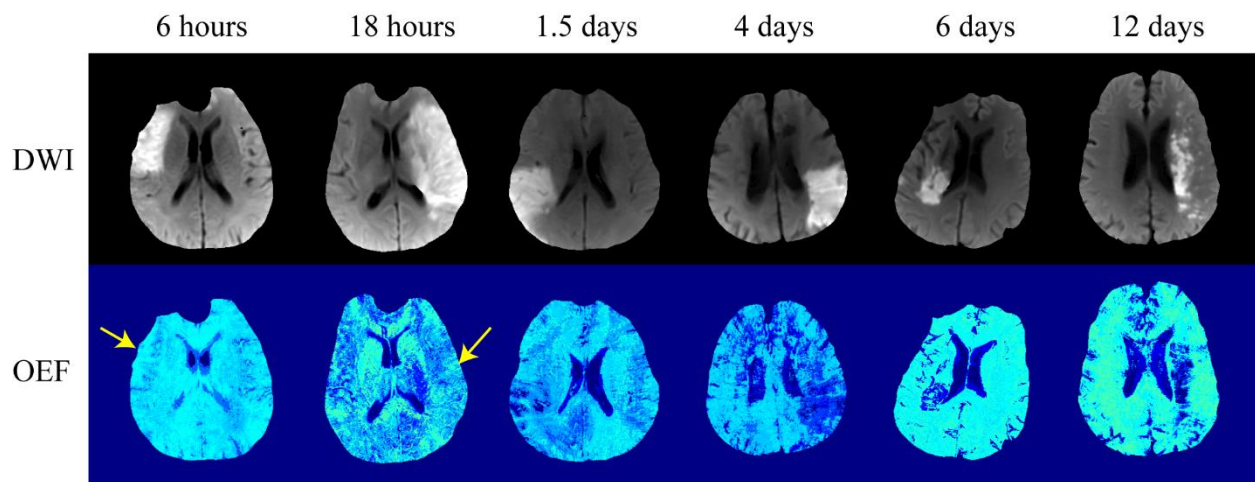


Figure 5.1. OEF maps in six ischemic stroke patients.

In the acute phase, there is some mis-match between low OEF areas and the DWI-defined lesion as yellow arrows indicate in 6 and 18 hours post onset. On the other hand, there is little mis-match after 4 days post onset.

Figure 5.2 shows average OEF values in lesion and contralateral side in each individual 30 cases. The OEF value in the lesion showed a trend of decrease as the post onset time increases. This means the ischemic tissue becomes functional impairment without timely reperfusion, and tends to be death. This agrees well with the dynamic process of the pathophysiological change, including inflammation triggered by oxygen free radicals and hypoxia and apoptosis induced by excessive glutamate-receptor activation, Ca^{2+} overload, oxygen radicals and DNA damage (112,113).

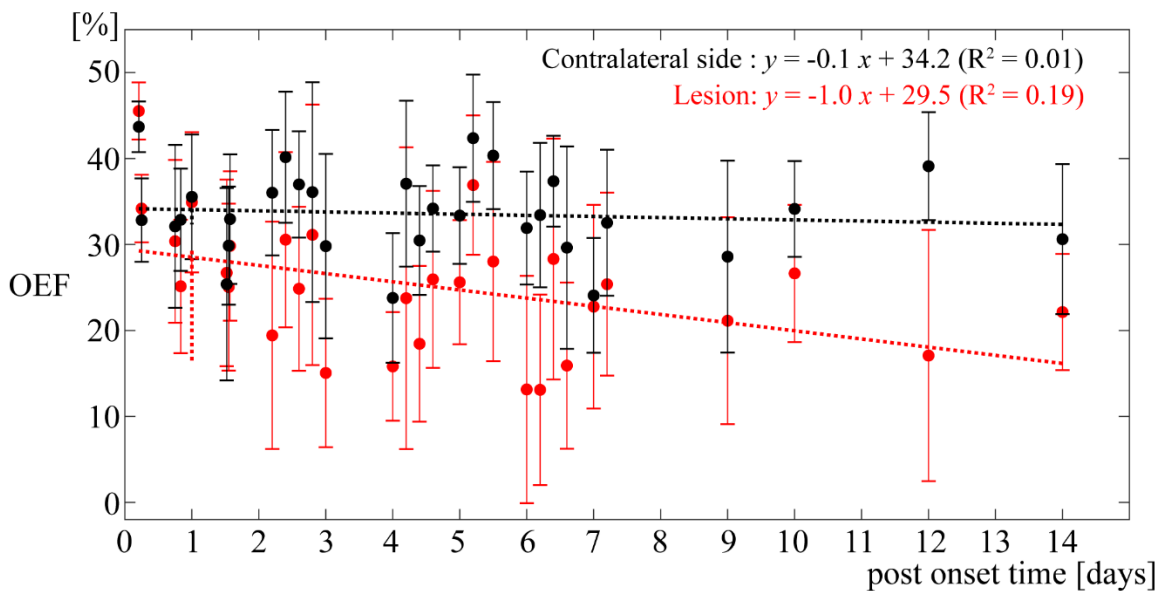


Figure 5.2. Average OEF value in the lesion and the contralateral side.

Each dot indicates each patient (30 patients). Red and black indicates lesion and contralateral side, respectively. The average OEF in the lesion decreases as the post onset time increases.

5.1.1.2 Clinical application in multiple sclerosis

Multiple sclerosis (MS) is an inflammatory demyelinating neurologic disease and the disease progression involves neurodegeneration. Impaired energy metabolism is a major contributor to the ongoing inflammation and neurodegeneration in MS brains, particularly MS lesions, with damaged mitochondrial ATP production (114). A better understanding of neural tissue energy metabolism may pave the way to optimized treatment of neurodegenerative process in MS. A few MRI studies have investigated OEF globally (115) and in cortical venous territories (116). However, voxel-wise regional OEF mapping is critical to allow investigating tissue damage in each MS lesion individually.

The OEF maps of 12 MS patients (39 ± 7 years) was obtained with QQ-CAT. Lesions were identified on T2w, and classified into three types relative to surrounding normal-appearing white matter (NAWM): QSM isointense (QSM-, $n=46$), QSM hyperintense with rim (QSM rim+, $n=32$) and QSM hyperintense without rim (QSM rim-, $n=101$). The OEF values among the three MS types were compared. Additionally, global OEF was compared with similar age 11 healthy controls (34 ± 12 years) using an unpaired t-test.

Global and cortical gray matter OEF of MS patients was significantly lower than healthy controls (33.3 ± 3.3 vs. 28.7 ± 2.9 %, $p<0.01$, and 32.7 ± 4.0 vs. 28.3 ± 2.9 %, $p<0.01$ respectively) (Figure 5.3). Lower global OEF in MS brains compared to healthy controls agrees well with the previously reported reduced OEF (115,116). One possible explanation of the decreased OEF is that mitochondrial ATP production is compromised in MS by increased ambient levels of nitric oxide (NO) (114). The increased NO inhibits cell respiratory chain function in mitochondria (117). The cortical OEF value is quite similar to that in a previous 7T studying using vein

susceptibility modeling (116), but the global OEF is slightly lower than that in a study using vein T2 modeling (115). This discrepancy may be explained by the complexity in estimating oxygenation from T2 model, particularly T2 dependence on red blood cell shape (118).

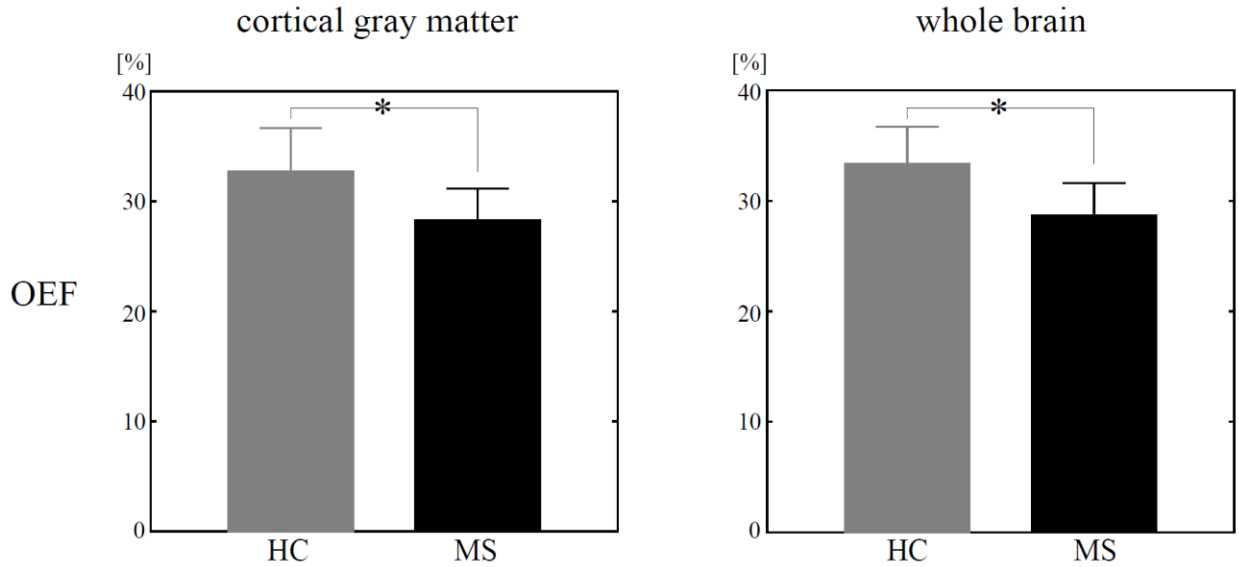


Figure 5.3. Average OEF between healthy controls (HC) and MS patients.

*In cortical gray matter and whole brain, the MS patients shows a significantly lower OEF values. HC: 34 ± 12 years, $n=11$ and MS: 39 ± 7 years, $n=12$. * indicates $p<0.01$ (unpaired *t*-test).*

In a MS patient with all three lesion types, QSM rim- shows heterogeneous OEF with the lesion, whereas QSM rim+ and QSM- shows uniformly low OEF value (Figure 5.4). QSM- represents old chronic lesion with little metabolism. QSM rim+ represents lesion with substantial tissue

damage (98), which is related to that the rim corresponds to iron in proinflammatory activated microglia (60). QSM rim- represents demyelinating lesions that can stay for an extended period of several years before dissipating into isointense level in QSM (chronic silent lesion, QSM-) (119). QSM- and QSM rim+ present lesser OEF compared to QSM rim- type (Figure 5.5), which agrees with tissue damage measured on myelin water fraction mapping (120) and neuroinflammation measured on translocator protein PET (121). The heterogeneous OEF of QSM rim- lesion (Figure 5.4) may reflect remyelination possibilities in the lesion. To the best of our knowledge, this is the first report on MS lesion OEF. In addition to widely used T1w, T2w, and QSM, the OEF map may provide information regarding tissue viability in various MS lesions.

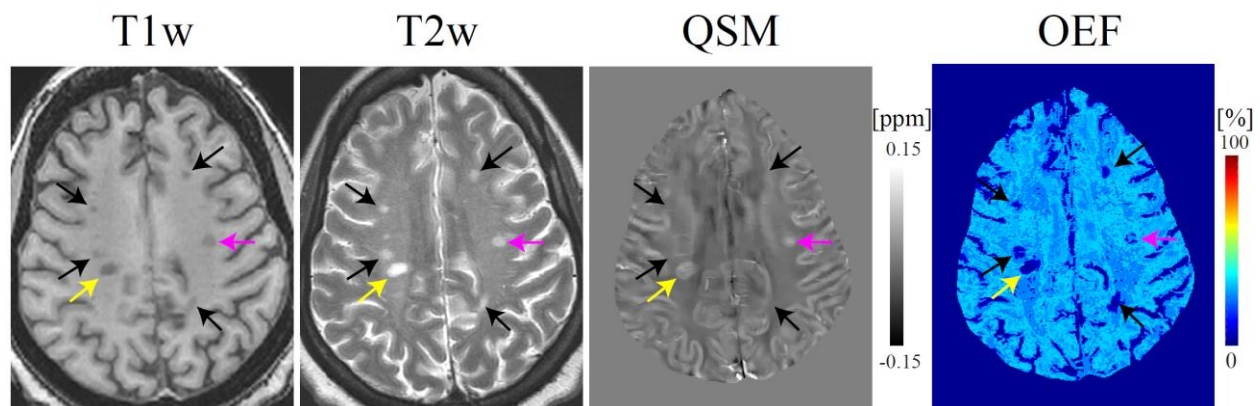


Figure 5.4. T1w, T2w, QSM, and OEF maps for an MS patient.

Arrows indicate QSM rim+ (yellow), QSM rim- (pink), and QSM- (black), respectively. The QSM rim- lesion has heterogeneous OEF. The disease duration for this subject is 122 months.

The QSM rim+ lesion has uniformly low OEF. All lesions are hypointense in T1w and hyperintense in T2w.

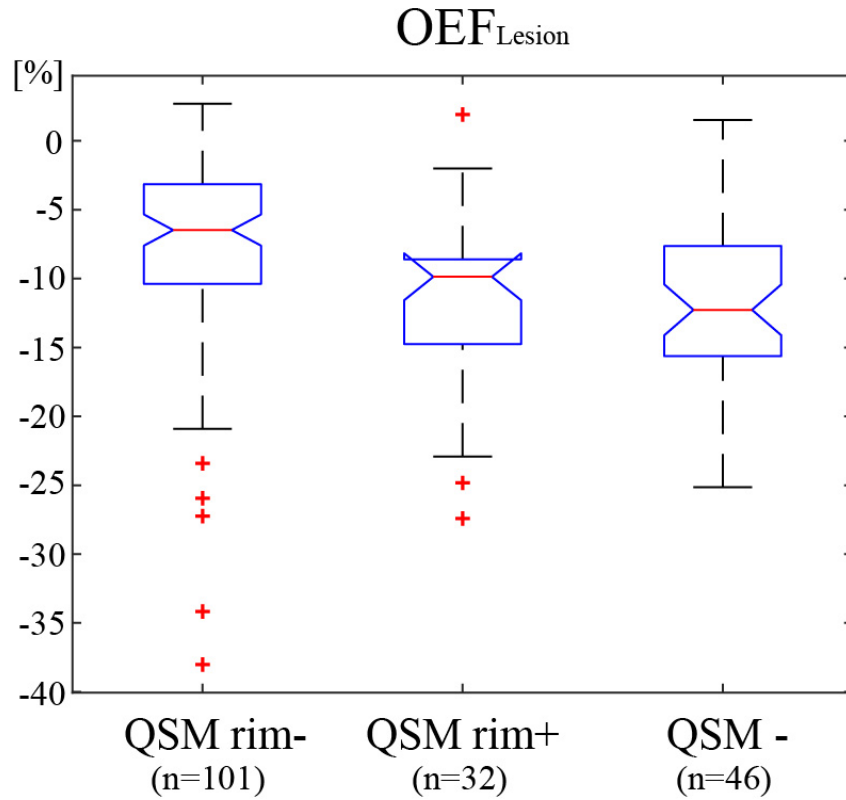


Figure 5.5. Lesion OEF in three MS types

QSM rim-, *QSM rim+*, and *QSM -* showed -8 ± 7 , -11 ± 6 , -12 ± 6 % OEF compared to normal-appearing white matter (NAWM). Red line, blue box, black whisker, and red cross indicates median value, interquartile range, the range extending to 1.5 of the interquartile range, and outlier beyond the whisker range.

5.1.1.3 Possible clinical application

OEF and CMRO₂ mapping would also be useful to investigate the tissue function and viability in various other cerebrovascular diseases, such as Sickle cell disease and Moyamoya disease. These two are commonly occlusive cerebrovascular diseases. First, Sickle cell disease progresses from abnormal (sickle) hemoglobin (122). The sickle hemoglobin is insoluble and undergoes polymerization and aggregation of the polymers into tubulin fibers that then produce sickling. Because of their rigid shape, the cells are prone to being trapped in the microcirculation. The downstream of this blockage are deprived of blood flow and oxygen and suffer ischemic damage or death. This blood flow deprivation leads to tissue necrosis.

Second, Moyamoya disease is also called as spontaneous occlusion of the circle of Willis, which is a classic example of a hemodynamic cause of stroke (123). The name “moyamoya” came from that the growth of small collateral vessels in the bottom of cerebrum is temporally accompanied with the vascular occlusion to compensate for the reduced blood flow, which describes puff of smoke in Japanese (124). However, the compensation mechanism eventually stop working. The treatment is needed to reduce the risk of stroke. Even though several imaging modalities, such as CT, PET, dynamic susceptibility contrast MRI, ASL, and MR angiography, were applied to guide treatment (125), the quantitative measurement of tissue oxygen consumption has not been investigated.

For both Sickle cell disease and Moyamoya diseases, OEF and CMRO₂ mapping would provide valuable information regarding the disease progress.

5.1.2 Deep learning for QQ

Due to non-convex nature of QQ model, the proposed CAT in Chapter 4 might still depend on the optimization details, e.g. initial guess and parameter scaling, in the usage of gradient-based iterative solver. Deep learning would be a good candidate for removing the dependency. Deep neural networks have been widely applied as an alternative to the iterative method for solving inversion (126-129) based on that neural networks can approximate any continuous function with sufficient number of free parameters (130). Also, the reconstruction speed of deep learning approach would be much faster than the gradient-based iterative solver once the training is done.

A fully convolutional neural network (QQ-NET), based on an established architecture, Unet (131), was trained with simulated data based on the QQ-CAT results as ground truth using Equations 1.4 and 1.5 at SNR 100 (29 patients for training and 1 patient for validation). The trained QQ-NET is tested with two datasets: 1) 4 additionally simulated stroke brain datasets constructed in the same way as the training data and 2) 30 real ischemic stroke patient data.

QQ-NET shows generally more accurate OEF map with smaller root mean square error (RMSE) and greater structure similarity index (SSIM) (Figure 5.6). QQ-NET shows slightly smoother OEF maps than QQ-CAT in simulations. The smoother OEF map may be caused by using Unet, a deep convolutional neural network. The network may learn output the average of all plausible explanations, which leads to spatial smoothness for the network prediction (132). Also, QQ-NET and QQ-CAT provides similar OEF maps in real stroke patients (Figure 5.7). In some cases, such as 1.5 and 7 days post onset, QQ-NET shows low OEF areas that agree better with DWI-defined lesions. This may lead to a stronger decreasing pattern of QQ-NET in the ratio scatter plot (Figure 5.8). The greater ratio than 100% from QQ-NET in the acute phase (Figure 5.8) is

consistent with expected OEF elevation (133). With the improved accuracy and speed, QQ-NET can be readily applied in clinical settings.

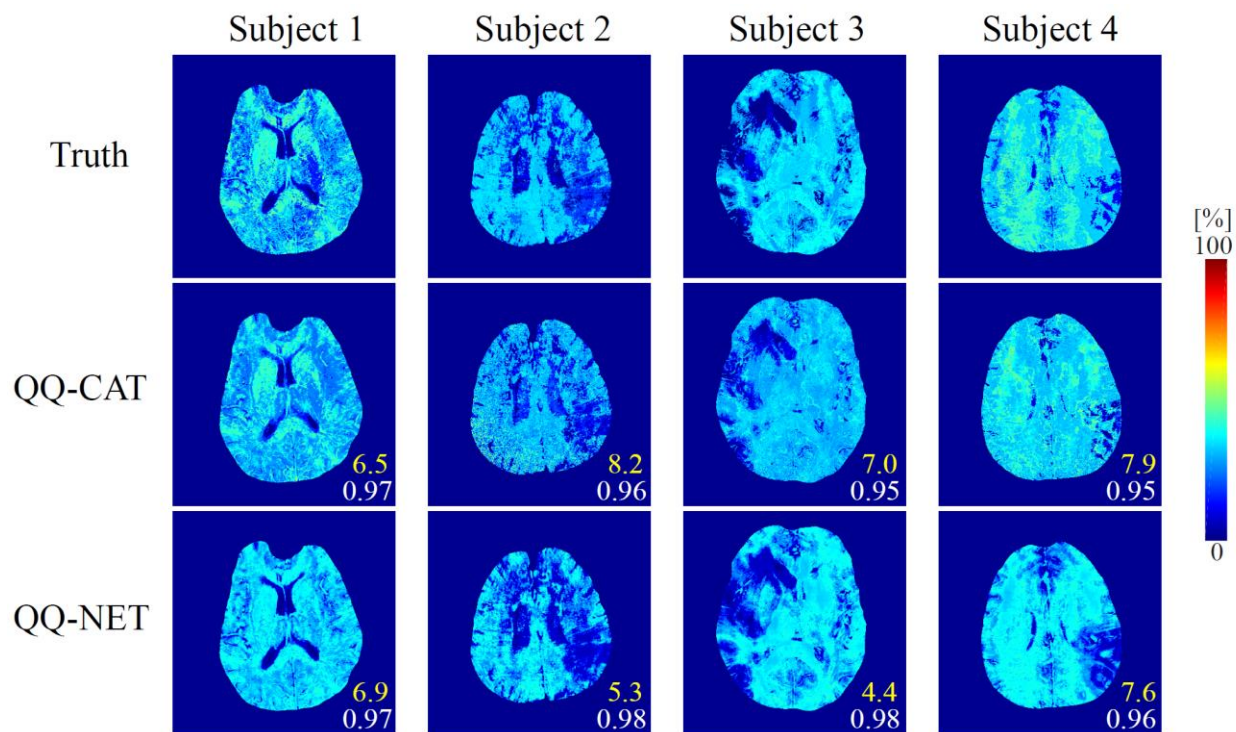


Figure 5.6. Comparison between the OEFs obtained by QQ-CAT and QQ-NET.

The numbers in yellow and white indicate root mean square error (RMSE) and structural similarity index (SSIM), respectively. QQ-NET generally provides smaller RMSE and higher SSIM.

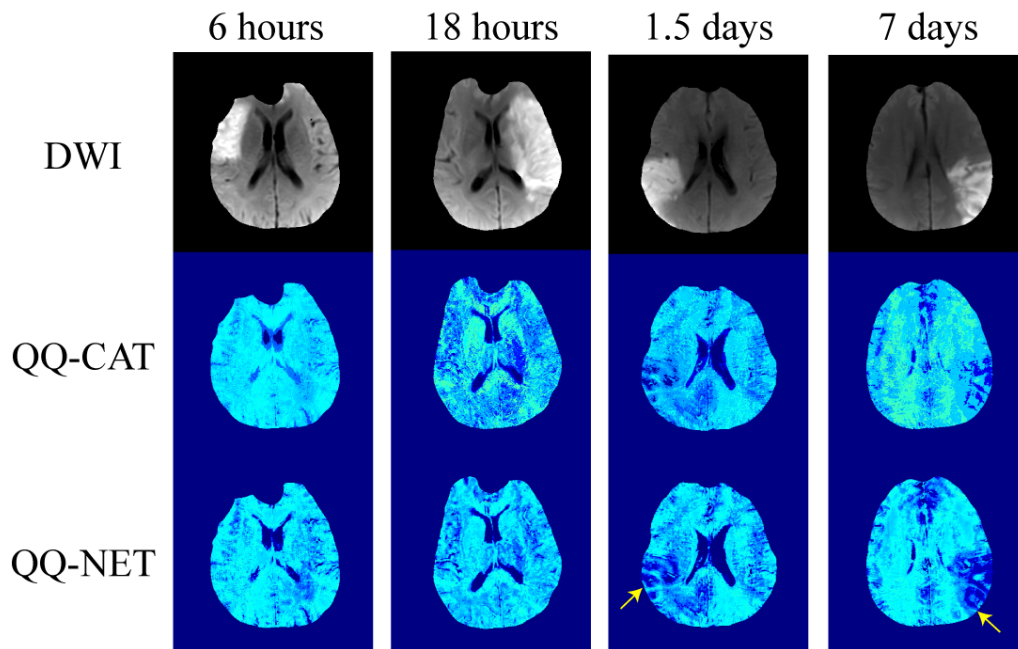


Figure 5.7. OEF Comparison between QQ-CAT and QQ-NET.

QQ-NET generally shows similar OEF maps compared to QQ-CAT, e.g. some parts in the lesion shows similar OEF values compared to contralateral side. In 1.5 and 7 days post-onset patients, low OEF areas in QQ-NET agree better with DWI-defined lesions.

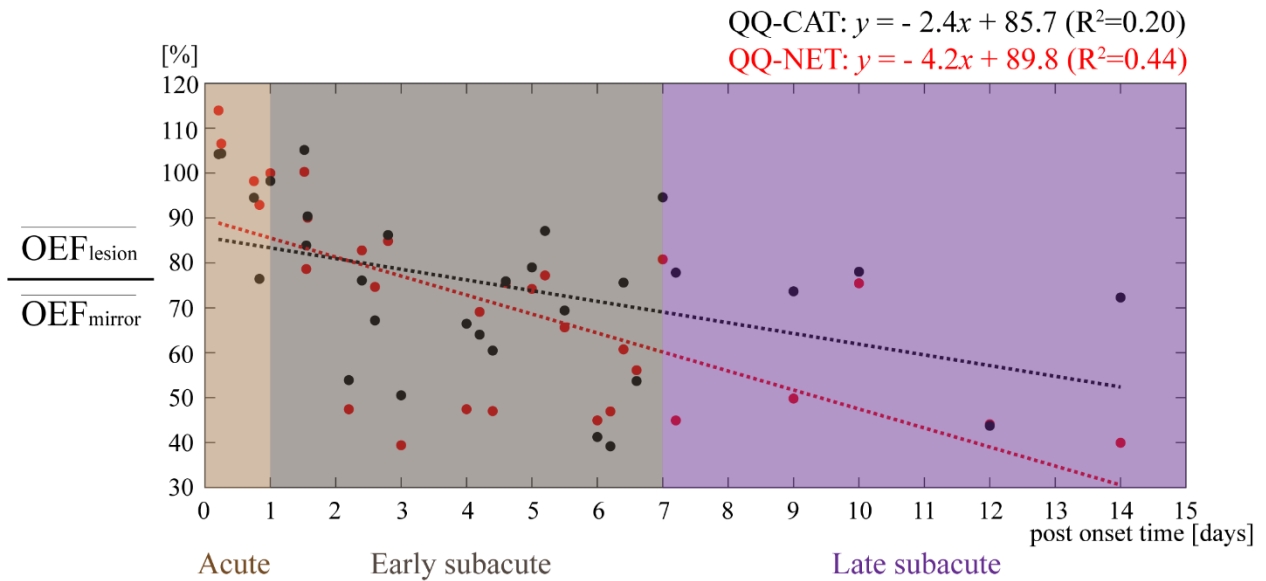


Figure 5.8. Scatter plot of the OEF ratio between lesion and contralateral side.

Each dot indicates each patient. Red and black indicates QQ-CAT and QQ-NET result, respectively. Dotted line indicates the linear regression. Brown, dark brown, and purple box indicates the acute (0~1 day), early subacute (1~7 days), and late subacute (7~14 days) phase, respectively. QQ-NET shows greater slope and R-square value.

5.1.3 Validation of QQ

The proposed CAT has not been validated with independent CMRO₂ methods. ¹⁵O PET has been considered as a reference. The validation of QQ with ¹⁵O-PET would be valuable in order to achieve reliability of QQ in clinical settings. However, the availability of PET data is limited because the short 2 min half-life of ¹⁵O necessitates its production right next to the PET scanner. Instead, a comparison study of QQ with a well-known independent MRI OEF method, dual-gas challenge calibrated-BOLD (DGC) (6,92), was performed.

QQ showed a small and statistically non-significant difference in OEF values compared to DGC (n=10): 36.4 ± 1.9 and 38.0 ± 9.1 % ($P=0.63$), with corresponding CMRO₂ of 151.4 ± 17.6 and 168.2 ± 54.1 $\mu\text{mol O}_2/\text{min}/100\text{g}$ ($P=0.26$) for QQ and DGC, respectively (Figure 5.9). The OEF values from both methods agree with literature values based on PET-OEF: 35 ± 7 % (62) and 40 ± 9 % (65). Also, QQ showed more uniform OEF map than DGC, which is consistent with PET studies (56,65,134). A high inter-subject variation in DGC may be attributed to low SNR in both BOLD and CBF signals, e.g. only 2.3 ± 0.5 % hypercapnia induced BOLD signal increase. The small OEF variation in QQ may have benefited from the usage of cluster analysis of time evolution (CAT) which improves effective SNR (35).

In hypercapnia (n=10), QQ showed lower OEF (36.4 ± 1.9 vs. 22.0 ± 3.6 %, $P<0.01$), higher CBF (57.0 ± 9.9 vs. 80.2 ± 11.6 %, $P<0.01$), slightly lower CMRO₂ maps (151.4 ± 17.6 vs. 130.2 ± 28.6 $\mu\text{mol O}_2/\text{min}/100\text{g}$, $P=0.039$) compared to those at baseline (Figure 5.10). The 14% CMRO₂ due to hypercapnia agrees well with a recent study suggesting 10~15% reduction with the similar hypercapnic level (135). This reduction shall be considered in the calibrated BOLD studies that have used an iso-CMRO₂ assumption during hypercapnia.

This cross-validation study supports the great potential of QQ for clinical use since QQ does not require a gas challenge unlike DGC using multiple gas challenges, hypercapnia and hyperoxia (6,7).

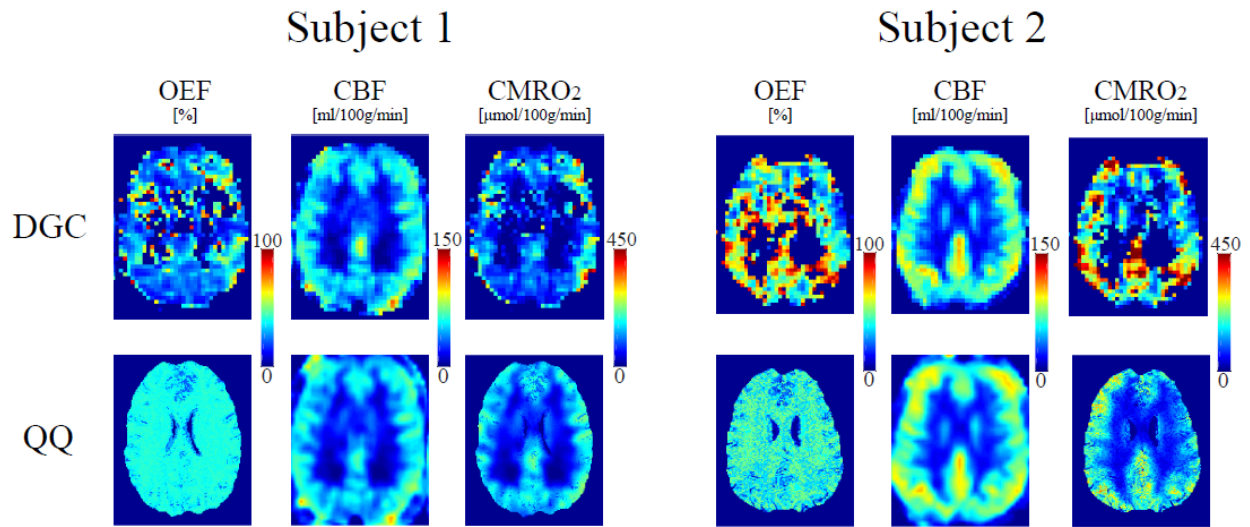


Figure 5.9. Baseline OEF, CBF, CMRO₂ map between DGC and QQ.

QQ CBF map is obtained by registering DGC CBF map to QSM resolution. QQ showed less inter-subject variation in OEF.

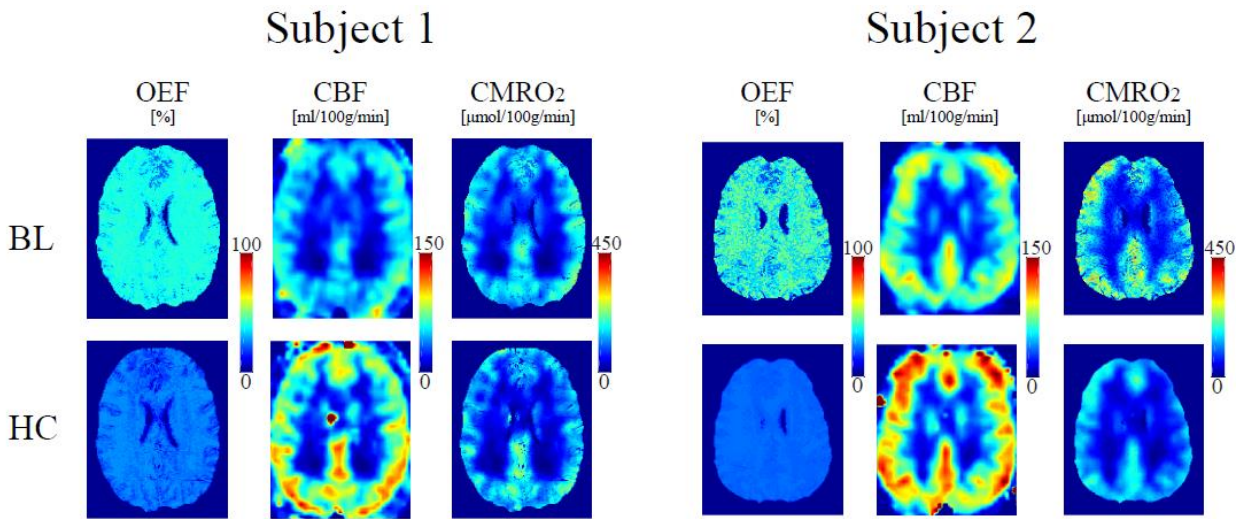


Figure 5.10. OEF, CBF, CMRO2 from QQ between baseline and hypercapnia.

Compared to BL, HC shows lower OEF, higher CBF, slightly lower CRMO2.

5.2 Conclusion

In this thesis, two major improvements in MRI biophysics modeling for improving CMRO2 are presented. First, the QSM- and qBOLD-based CMRO2 method was combined to remove unnecessary assumptions in individual model and to utilize both phase and magnitude signal from the same mGRE data. Second, cluster analysis of time evolution (CAT) was applied to improve robustness of the combined model against noise.

APPENDIX

Dipole and Quadrupole formulism derivation

For derivation of dipole and quadrupole formulism, we start with the “H” field that has a scalar potential Φ solution to the magnetostatics problem (136):

$$\nabla \times \mathcal{H} = 0, \quad \nabla \cdot \mathcal{H} = -\nabla \cdot \mathbf{M}. \quad [\text{A1}]$$

$$\mathcal{H} = -\nabla\Phi \quad [\text{A2}]$$

$$\Phi(\mathbf{x}) = \frac{1}{4\pi} \int \frac{\nabla' \cdot \mathbf{M}(\mathbf{x}')}{|\mathbf{x} - \mathbf{x}'|} d^3x' \quad [\text{A3}]$$

This Φ has singularity at the origin where the measurement point (\mathbf{x}) and source location (\mathbf{x}') are identical. To facilitate calculus on $1/|\mathbf{x} - \mathbf{x}'|$, the origin has to be excluded (137).

$$\Phi(\mathbf{x}) = \lim_{\epsilon \rightarrow 0} \frac{1}{4\pi} \int \frac{\nabla' \cdot \mathbf{M}(\mathbf{x}')}{|\mathbf{x} - \mathbf{x}'|} H(|\mathbf{x} - \mathbf{x}'| - \epsilon) d^3x' \quad [\text{A4}]$$

where H is the Heaviside function defined by

$$H(|\mathbf{x} - \mathbf{x}'| - \epsilon) = \begin{cases} 0, & |\mathbf{x} - \mathbf{x}'| \leq \epsilon \\ 1, & |\mathbf{x} - \mathbf{x}'| > \epsilon \end{cases}$$

The term $H(|\mathbf{x} - \mathbf{x}'| - \epsilon)/|\mathbf{x} - \mathbf{x}'|$ can be expanded up to the 2rd order with Taylor expansion in powers of \mathbf{x}' with the localized source condition (136). This leads to Eq. A5 with the B_0 along \hat{z} .

$$\Phi(\mathbf{x}) = \frac{B_0}{\mu_0} \left(D_\Phi \chi + \sum_{m=1}^3 g_{m\Phi} Q_m \right) \quad [\text{A5}]$$

where the dipole interaction, D_Φ and the susceptibility, χ are as follows:

$$D_\Phi = \lim_{\epsilon \rightarrow 0} \frac{1}{4\pi|\mathbf{x}|^2} \left\{ \frac{x_3}{|\mathbf{x}|} H(|\mathbf{x}| - \epsilon) - x_3 \delta(|\mathbf{x}| - \epsilon) \right\} \quad [\text{A6}]$$

The quadrupole interaction, $g_{m\Phi}$ and the quadrupole moments, Q_m are as follows:

$$g_{m\Phi} = \begin{cases} \lim_{\epsilon \rightarrow 0} \frac{1}{4\pi|\mathbf{x}|^4} \left\{ \frac{3x_m x_3}{|\mathbf{x}|} H(|\mathbf{x}| - \epsilon) - 4x_m x_3 \delta(|\mathbf{x}| - \epsilon) \right\}, & i = 1, 2 \\ \lim_{\epsilon \rightarrow 0} \frac{1}{4\pi|\mathbf{x}|^4} \left\{ \frac{3x_3^2 - |\mathbf{x}|^2}{|\mathbf{x}|} H(|\mathbf{x}| - \epsilon) - (4x_3^2 - |\mathbf{x}|^2) \delta(|\mathbf{x}| - \epsilon) \right\}, & i = 3 \end{cases} \quad [\text{A7}]$$

The \mathcal{H} field z-component can be obtained as follows, based on Eq. A5.

$$\mathcal{H}_z(\mathbf{x}) = -\partial_z \Phi(\mathbf{x}) \quad [\text{A8}]$$

The \mathbf{B} field in Eq. 2 can be obtained with $= \mu_0(\mathcal{H} + \mathbf{M})$. The ϵ limit to 0 was also taken to the $\partial_z D_\Phi$ and $\partial_z g_{i\Phi}$ terms in Eq. A8 (137).

REFERENCE

1. Derdeyn CP, Videen TO, Yundt KD, Fritsch SM, Carpenter DA, Grubb RL, Powers WJ. Variability of cerebral blood volume and oxygen extraction: stages of cerebral haemodynamic impairment revisited. *Brain : a journal of neurology* 2002;125(Pt 3):595-607.
2. Gupta A, Chazen JL, Hartman M, Delgado D, Anumula N, Shao H, Mazumdar M, Segal AZ, Kamel H, Leifer D, Sanelli PC. Cerebrovascular reserve and stroke risk in patients with carotid stenosis or occlusion: a systematic review and meta-analysis. *Stroke* 2012;43(11):2884-2891.
3. Gupta A, Baradaran H, Schweitzer AD, Kamel H, Pandya A, Delgado D, Wright D, Hurtado-Rua S, Wang Y, Sanelli PC. Oxygen Extraction Fraction and Stroke Risk in Patients with Carotid Stenosis or Occlusion: A Systematic Review and Meta-Analysis. *American Journal of Neuroradiology* 2014;35(2):250-255.
4. Rodgers ZB, Detre JA, Wehrli FW. MRI-based methods for quantification of the cerebral metabolic rate of oxygen. *Journal of Cerebral Blood Flow & Metabolism* 2016;36(7):1165-1185.
5. Bolar DS, Rosen BR, Sorensen A, Adalsteinsson E. QUantitative Imaging of eXtraction of oxygen and Tissue consumption (QUIXOTIC) using venular-targeted velocity-selective spin labeling. *Magnetic resonance in medicine* 2011;66(6):1550-1562.
6. Bulte DP, Kelly M, Germuska M, Xie J, Chappell MA, Okell TW, Bright MG, Jezzard P. Quantitative measurement of cerebral physiology using respiratory-calibrated MRI. *Neuroimage* 2012;60(1):582-591.
7. Gauthier CJ, Hoge RD. Magnetic resonance imaging of resting OEF and CMRO₂ using a generalized calibration model for hypercapnia and hyperoxia. *Neuroimage* 2012;60(2):1212-1225.

8. Hoge RD. Calibrated FMRI. *Neuroimage* 2012;62(2):930-937.
9. Wise RG, Harris AD, Stone AJ, Murphy K. Measurement of OEF and absolute CMRO₂: MRI-based methods using interleaved and combined hypercapnia and hyperoxia. *Neuroimage* 2013;83:135-147.
10. He X, Yablonskiy DA. Quantitative BOLD: mapping of human cerebral deoxygenated blood volume and oxygen extraction fraction: default state. *Magn Reson Med* 2007;57(1):115-126.
11. Yablonskiy DA, Sukstanskii AL, He X. BOLD-based Techniques for Quantifying Brain Hemodynamic and Metabolic Properties – Theoretical Models and Experimental Approaches. *NMR in biomedicine* 2013;26(8):963-986.
12. Ulrich X, Yablonskiy DA. Separation of cellular and BOLD contributions to T2* signal relaxation. *Magn Reson Med* 2016;75(2):606-615.
13. Wehrli FW, Fan AP, Rodgers ZB, Englund EK, Langham MC. Susceptibility-based time-resolved whole-organ and regional tissue oximetry. *NMR in biomedicine* 2017;30(4).
14. Fan AP, Benner T, Bolar DS, Rosen BR, Adalsteinsson E. Phase-based regional oxygen metabolism (PROM) using MRI. *Magn Reson Med* 2012;67(3):669-678.
15. Jain V, Langham MC, Wehrli FW. MRI Estimation of Global Brain Oxygen Consumption Rate. *Journal of Cerebral Blood Flow & Metabolism* 2010;30(9):1598-1607.
16. Wehrli FW, Rodgers ZB, Jain V, Langham MC, Li C, Licht DJ, Magland J. Time-resolved MRI oximetry for quantifying CMRO₂ and vascular reactivity. *Academic radiology* 2014;21(2):207-214.
17. Zhang J, Liu T, Gupta A, Spincemaille P, Nguyen TD, Wang Y. Quantitative mapping of cerebral metabolic rate of oxygen (CMRO₂) using quantitative susceptibility mapping (QSM). *Magnetic Resonance in Medicine* 2015;74(4):945-952.

18. Zhang J, Cho J, Zhou D, Nguyen TD, Spincemaille P, Gupta A, Wang Y. Quantitative susceptibility mapping-based cerebral metabolic rate of oxygen mapping with minimum local variance. *Magn Reson Med* 2017.
19. Zhang J, Zhou D, Nguyen TD, Spincemaille P, Gupta A, Wang Y. Cerebral metabolic rate of oxygen (CMRO₂) mapping with hyperventilation challenge using quantitative susceptibility mapping (QSM). *Magnetic resonance in medicine* 2017;77(5):1762-1773.
20. Kressler B, de Rochefort L, Liu T, Spincemaille P, Jiang Q, Wang Y. Nonlinear regularization for per voxel estimation of magnetic susceptibility distributions from MRI field maps. *IEEE transactions on medical imaging* 2010;29(2):273-281.
21. Liu J, Liu T, de Rochefort L, Ledoux J, Khalidov I, Chen W, Tsiouris AJ, Wisnieff C, Spincemaille P, Prince MR, Wang Y. Morphology enabled dipole inversion for quantitative susceptibility mapping using structural consistency between the magnitude image and the susceptibility map. *NeuroImage* 2012;59(3):2560-2568.
22. Wang Y, Liu T. Quantitative susceptibility mapping (QSM): Decoding MRI data for a tissue magnetic biomarker. *Magn Reson Med* 2015;73(1):82-101.
23. Cho J, Zhou D, Kee Y, Spincemaille P, Wang Y. Quantitative Susceptibility Mapping of Magnetic Quadrupole Moments. *Concepts in Magnetic Resonance Part A* 2019;2019:14.
24. Sakai F, Nakazawa K, Tazaki Y, Ishii K, Hino H, Igarashi H, Kanda T. Regional cerebral blood volume and hematocrit measured in normal human volunteers by single-photon emission computed tomography. *Journal of cerebral blood flow and metabolism : official journal of the International Society of Cerebral Blood Flow and Metabolism* 1985;5(2):207-213.
25. Savicki JP, Lang G, Ikeda-Saito M. Magnetic susceptibility of oxy- and carbonmonoxyhemoglobins. *Proceedings of the National Academy of Sciences* 1984;81(17):5417-5419.
26. Hoffman R. *Hematology: Basic Principles and Practice*: Churchill Livingstone; 2005.

27. Spees WM, Yablonskiy DA, Oswald MC, Ackerman JJ. Water proton MR properties of human blood at 1.5 Tesla: magnetic susceptibility, T(1), T(2), T*(2), and non-Lorentzian signal behavior. *Magn Reson Med* 2001;45(4):533-542.
28. Cerdonio M, Morante S, Torresani D, Vitale S, DeYoung A, Noble RW. Reexamination of the evidence for paramagnetism in oxy- and carbonmonoxyhemoglobins. *Proceedings of the National Academy of Sciences of the United States of America* 1985;82(1):102-103.
29. An H, Lin W. Cerebral oxygen extraction fraction and cerebral venous blood volume measurements using MRI: effects of magnetic field variation. *Magn Reson Med* 2002;47(5):958-966.
30. Leenders KL, Perani D, Lammertsma AA, Heather JD, Buckingham P, Healy MJ, Gibbs JM, Wise RJ, Hatazawa J, Herold S, et al. Cerebral blood flow, blood volume and oxygen utilization. Normal values and effect of age. *Brain : a journal of neurology* 1990;113 (Pt 1):27-47.
31. Sukstanskii AL, Yablonskiy DA. Theory of FID NMR signal dephasing induced by mesoscopic magnetic field inhomogeneities in biological systems. *Journal of magnetic resonance (San Diego, Calif : 1997)* 2001;151(1):107-117.
32. Yablonskiy DA, Haacke EM. Theory of NMR signal behavior in magnetically inhomogeneous tissues: the static dephasing regime. (0740-3194 (Print)).
33. He X, Yablonskiy DA. Biophysical mechanisms of phase contrast in gradient echo MRI. *Proceedings of the National Academy of Sciences* 2009;106(32):13558-13563.
34. Cho J, Kee Y, Spincemille P, Nguyen TD, Zhang J, Gupta A, Zhang S, Wang Y. Cerebral metabolic rate of oxygen (CMRO₂) mapping by combining quantitative susceptibility mapping (QSM) and quantitative blood oxygenation level-dependent imaging (qBOLD). *Magnetic resonance in medicine* 2018;80(4):1595-1604.

35. Cho J, Zhang S, Kee Y, Spincemaille P, Nguyen TD, Hubertus S, Gupta A, Wang Y. Cluster analysis of time evolution (CAT) for quantitative susceptibility mapping (QSM) and quantitative blood oxygen level-dependent magnitude (qBOLD)-based oxygen extraction fraction (OEF) and cerebral metabolic rate of oxygen (CMRO₂) mapping. *Magnetic resonance in medicine*;0(0).
36. Wang Y. *Principles of Magnetic Resonance Imaging: Physics Concepts, Pulse Sequences, & Biomedical Applications: CreateSpace Independent Publishing Platform*; 2012.
37. Kee Y, Liu Z, Zhou L, Dimov A, Cho J, de Rochefort L, Seo JK, Wang Y. Quantitative Susceptibility Mapping (QSM) Algorithms: Mathematical Rationale and Computational Implementations. *IEEE transactions on bio-medical engineering* 2017;64(11):2531-2545.
38. Haacke EM, Brown RW, Thompson MR, Venkatesan R. *Magnetic Resonance Imaging: Physical Principles and Sequence Design*: Wiley; 1999.
39. Wang X, Sukstanskii AL, Yablonskiy DA. Optimization strategies for evaluation of brain hemodynamic parameters with qBOLD technique. *Magnetic resonance in medicine* 2013;69(4):1034-1043.
40. X. U, DA. Y. Enhancing image contrast in human brain by voxel spread function method. In *Proceedings of the 22nd Annual Meeting of ISMRM*;Milan, Italy, Abstract 3197.
41. Baron JC. Mapping the ischaemic penumbra with PET: implications for acute stroke treatment. *Cerebrovascular diseases (Basel, Switzerland)* 1999;9(4):193-201.
42. Grandin CB, Duprez TP, Smith AM, Mataigne F, Peeters A, Oppenheim C, Cosnard G. Usefulness of Magnetic Resonance–Derived Quantitative Measurements of Cerebral Blood Flow and Volume in Prediction of Infarct Growth in Hyperacute Stroke. *Stroke* 2001;32(5):1147-1153.
43. Hogg R, McKean J, Craig A. *Introduction to mathematical statistics*: Pearson Education; 2005.

44. Dai W, Garcia D, de Bazelaire C, Alsop DC. Continuous flow-driven inversion for arterial spin labeling using pulsed radio frequency and gradient fields. *Magn Reson Med* 2008;60(6):1488-1497.
45. Alsop DC, Detre JA, Golay X, Gunther M, Hendrikse J, Hernandez-Garcia L, Lu H, MacIntosh BJ, Parkes LM, Smits M, van Osch MJ, Wang DJ, Wong EC, Zaharchuk G. Recommended implementation of arterial spin-labeled perfusion MRI for clinical applications: A consensus of the ISMRM perfusion study group and the European consortium for ASL in dementia. *Magn Reson Med* 2015;73(1):102-116.
46. Buxton RB, Frank LR, Wong EC, Siewert B, Warach S, Edelman RR. A general kinetic model for quantitative perfusion imaging with arterial spin labeling. *Magnetic resonance in medicine* 1998;40(3):383-396.
47. Xu B, Liu T, Spincemaille P, Prince M, Wang Y. Flow compensated quantitative susceptibility mapping for venous oxygenation imaging. *Magn Reson Med* 2014;72(2):438-445.
48. Liu T, Khalidov I, de Rochefort L, Spincemaille P, Liu J, Tsiouris AJ, Wang Y. A novel background field removal method for MRI using projection onto dipole fields (PDF). *NMR in biomedicine* 2011;24(9):1129-1136.
49. Mugler JP, 3rd, Brookeman JR. Three-dimensional magnetization-prepared rapid gradient-echo imaging (3D MP RAGE). *Magn Reson Med* 1990;15(1):152-157.
50. de Rochefort L, Liu T, Kressler B, Liu J, Spincemaille P, Lebon V, Wu J, Wang Y. Quantitative susceptibility map reconstruction from MR phase data using bayesian regularization: validation and application to brain imaging. *Magn Reson Med* 2010;63(1):194-206.
51. Jenkinson M, Smith S. A global optimisation method for robust affine registration of brain images. *Medical image analysis* 2001;5(2):143-156.

52. Jenkinson M, Bannister P, Brady M, Smith S. Improved optimization for the robust and accurate linear registration and motion correction of brain images. *NeuroImage* 2002;17(2):825-841.
53. Hansen PC. Analysis of Discrete Ill-Posed Problems by Means of the L-Curve. *SIAM Review* 1992;34(4):561-580.
54. Liu DC, Nocedal J. On the limited memory BFGS method for large scale optimization. *Mathematical programming* 1989;45(1):503-528.
55. Byrd RH, Lu P, Nocedal J, Zhu C. A limited memory algorithm for bound constrained optimization. *SIAM Journal on Scientific Computing* 1995;16(5):1190-1208.
56. Mintun MA, Raichle ME, Martin WR, Herscovitch P. Brain oxygen utilization measured with O-15 radiotracers and positron emission tomography. *Journal of nuclear medicine : official publication, Society of Nuclear Medicine* 1984;25(2):177-187.
57. Sun X, He G, Qing H, Zhou W, Dobie F, Cai F, Staufenbiel M, Huang LE, Song W. Hypoxia facilitates Alzheimer's disease pathogenesis by up-regulating BACE1 gene expression. *Proceedings of the National Academy of Sciences of the United States of America* 2006;103(49):18727-18732.
58. Acosta-Cabronero J, Williams GB, Cardenas-Blanco A, Arnold RJ, Lupson V, Nestor PJ. In vivo quantitative susceptibility mapping (QSM) in Alzheimer's disease. *PloS one* 2013;8(11):e81093.
59. Trapp BD, Stys PK. Virtual hypoxia and chronic necrosis of demyelinated axons in multiple sclerosis. *The Lancet Neurology* 2009;8(3):280-291.
60. Wisnieff C, Ramanan S, Olesik J, Gauthier S, Wang Y, Pitt D. Quantitative susceptibility mapping (QSM) of white matter multiple sclerosis lesions: Interpreting positive susceptibility and the presence of iron. *Magn Reson Med* 2015;74(2):564-570.

61. Kudo K, Liu T, Murakami T, Goodwin J, Uwano I, Yamashita F, Higuchi S, Wang Y, Ogasawara K, Ogawa A, Sasaki M. Oxygen extraction fraction measurement using quantitative susceptibility mapping: Comparison with positron emission tomography. *Journal of cerebral blood flow and metabolism : official journal of the International Society of Cerebral Blood Flow and Metabolism* 2016;36(8):1424-1433.
62. Carpenter DA, Grubb RL, Jr., Tempel LW, Powers WJ. Cerebral oxygen metabolism after aneurysmal subarachnoid hemorrhage. *Journal of cerebral blood flow and metabolism : official journal of the International Society of Cerebral Blood Flow and Metabolism* 1991;11(5):837-844.
63. Yamauchi H, Fukuyama H, Nagahama Y, Nabatame H. Significance of increased oxygen extraction fraction in five-year prognosis of major cerebral arterial occlusive diseases. *The Journal of Nuclear Medicine* 1999;40(12):1992.
64. Michael N. Diringer, Kent Yundt, Tom O. Videen, Robert E. Adams, Allyson R. Zazulia, Ellen Deibert, Venkatesh Aiyagari, Ralph G. Dacey J, Robert L. Grubb J, William J. Powers. No reduction in cerebral metabolism as a result of early moderate hyperventilation following severe traumatic brain injury. *Journal of neurosurgery* 2000;92(1):7-13.
65. Raichle ME, MacLeod AM, Snyder AZ, Powers WJ, Gusnard DA, Shulman GL. A default mode of brain function. *Proceedings of the National Academy of Sciences* 2001;98(2):676-682.
66. Doepp F, Schreiber SJ, von Munster T, Rademacher J, Klingebiel R, Valdueza JM. How does the blood leave the brain? A systematic ultrasound analysis of cerebral venous drainage patterns. *Neuroradiology* 2004;46(7):565-570.
67. Meder JF, Chiras J, Roland J, Guinet P, Bracard S, Bargy F. Venous territories of the brain. *Journal of neuroradiology Journal de neuroradiologie* 1994;21(2):118-133.

68. Fan AP, Bilgic B, Gagnon L, Witzel T, Bhat H, Rosen BR, Adalsteinsson E. Quantitative oxygenation venography from MRI phase. *Magnetic resonance in medicine* 2014;72(1):149-159.
69. Langkammer C, Krebs N, Goessler W, Scheurer E, Yen K, Fazekas F, Ropele S. Susceptibility induced gray-white matter MRI contrast in the human brain. *Neuroimage* 2012;59(2):1413-1419.
70. Gardener AG, Jezzard P. Investigating white matter perfusion using optimal sampling strategy arterial spin labeling at 7 Tesla. *Magnetic resonance in medicine* 2015;73(6):2243-2248.
71. Lee H, Englund EK, Wehrli FW. Interleaved quantitative BOLD: Combining extravascular $R2'$ - and intravascular $R2$ -measurements for estimation of deoxygenated blood volume and hemoglobin oxygen saturation. *Neuroimage* 2018;174:420-431.
72. Aaron Tropp J. *Topics in sparse approximation* 2004.
73. Aharon M, Elad M, Bruckstein A. K-SVD: An Algorithm for Designing Overcomplete Dictionaries for Sparse Representation 2006. 4311-4322 p.
74. Liu ZA-Ohoo, Spincemaille P, Yao Y, Zhang Y, Wang Y. MEDI+0: Morphology enabled dipole inversion with automatic uniform cerebrospinal fluid zero reference for quantitative susceptibility mapping. (1522-2594 (Electronic)).
75. Forgy EW. Cluster analysis of multivariate data : efficiency versus interpretability of classifications. *Biometrics* 1965;21:768-769.
76. MacQueen J. Some methods for classification and analysis of multivariate observations. *Fifth Berkeley Symposium on Mathematical Statistics and Probability*; 1967 1967; Berkeley, Calif. University of California Press. p 281-297. (Fifth Berkeley Symposium on Mathematical Statistics and Probability).

77. Jain AK. Data clustering: 50 years beyond K-means. *Pattern Recognition Letters* 2010;31(8):651-666.
78. Lloyd S. Least squares quantization in PCM. *IEEE Transactions on Information Theory* 1982;28(2):129-137.
79. Pelleg D, Moore AW. X-means: Extending K-means with Efficient Estimation of the Number of Clusters. *Proceedings of the Seventeenth International Conference on Machine Learning: Morgan Kaufmann Publishers Inc.*; 2000. p 727-734.
80. Kass RE, Raftery AE. Bayes Factors. *Journal of the American Statistical Association* 1995;90(430):773-795.
81. Zhang Y, Brady M, Smith S. Segmentation of brain MR images through a hidden Markov random field model and the expectation-maximization algorithm. *IEEE transactions on medical imaging* 2001;20(1):45-57.
82. Pei M, Nguyen TD, Thimmappa ND, Salustri C, Dong F, Cooper MA, Li J, Prince MR, Wang Y. Algorithm for fast monoexponential fitting based on Auto-Regression on Linear Operations (ARLO) of data. *Magn Reson Med* 2015;73(2):843-850.
83. Baune A, Sommer FT, Erb M, Wildgruber D, Kardatzki B, Palm G, Grodd W. Dynamical Cluster Analysis of Cortical fMRI Activation. *Neuroimage* 1999;9(5):477-489.
84. Heller R, Stanley D Fau - Yekutieli D, Yekutieli D Fau - Rubin N, Rubin N Fau - Benjamini Y, Benjamini Y. Cluster-based analysis of FMRI data. (1053-8119 (Print)).
85. Christen T, Schmiedeskamp H, Straka M, Bammer R, Zaharchuk G. Measuring brain oxygenation in humans using a multiparametric quantitative blood oxygenation level dependent MRI approach. *Magn Reson Med* 2012;68(3):905-911.
86. Ito H, Ibaraki M, Kanno I, Fukuda H, Miura S. Changes in the Arterial Fraction of Human Cerebral Blood Volume during Hypercapnia and Hypocapnia Measured by

- Positron Emission Tomography. *Journal of Cerebral Blood Flow & Metabolism* 2005;25(7):852-857.
87. Ito H, Kanno I Fau - Iida H, Iida H Fau - Hatazawa J, Hatazawa J Fau - Shimosegawa E, Shimosegawa E Fau - Tamura H, Tamura H Fau - Okudera T, Okudera T. Arterial fraction of cerebral blood volume in humans measured by positron emission tomography. (0914-7187 (Print)).
 88. Hongyu A, Weili L. Cerebral venous and arterial blood volumes can be estimated separately in humans using magnetic resonance imaging. *Magnetic resonance in medicine* 2002;48(4):583-588.
 89. Stone AJ, Blockley NP. A streamlined acquisition for mapping baseline brain oxygenation using quantitative BOLD. *Neuroimage* 2017;147:79-88.
 90. Hua J, Liu P, Kim T, Donahue M, Rane S, Chen JJ, Qin Q, Kim SG. MRI techniques to measure arterial and venous cerebral blood volume. *Neuroimage* 2019;187:17-31.
 91. Blockley NP, Griffeth VE, Germuska MA, Bulte DP, Buxton RB. An analysis of the use of hyperoxia for measuring venous cerebral blood volume: comparison of the existing method with a new analysis approach. *Neuroimage* 2013;72:33-40.
 92. Blockley NP, Griffeth VE, Simon AB, Buxton RB. A review of calibrated blood oxygenation level-dependent (BOLD) methods for the measurement of task-induced changes in brain oxygen metabolism. *NMR in biomedicine* 2013;26(8):987-1003.
 93. Domsch S, Mie MB, Wenz F, Schad LR. Non-invasive multiparametric qBOLD approach for robust mapping of the oxygen extraction fraction. *Zeitschrift für Medizinische Physik* 2014;24(3):231-242.
 94. Hatazawa J, Shimosegawa E Fau - Toyoshima H, Toyoshima H Fau - Ardekani BA, Ardekani Ba Fau - Suzuki A, Suzuki A Fau - Okudera T, Okudera T Fau - Miura Y, Miura Y. Cerebral blood volume in acute brain infarction: A combined study with dynamic susceptibility contrast MRI and 99mTc-HMPAO-SPECT. (0039-2499 (Print)).

95. Siemonsen S, Löbel U, Sedlacik J, Forkert ND, Mouridsen K, Østergaard L, Thomalla G, Fiehler J. Elevated T2-values in MRI of stroke patients shortly after symptom onset do not predict irreversible tissue infarction. *Brain : a journal of neurology* 2012;135(6):1981-1989.
96. Wang Y, Spincemaille P, Liu Z, Dimov A, Deh K, Li J, Zhang Y, Yao Y, Gillen KM, Wilman AH, Gupta A, Tsiouris AJ, Kovanlikaya I, Chiang GC, Weinsaft JW, Tanenbaum L, Chen W, Zhu W, Chang S, Lou M, Kopell BH, Kaplitt MG, Devos D, Hirai T, Huang X, Korogi Y, Shtilbans A, Jahng GH, Pelletier D, Gauthier SA, Pitt D, Bush AI, Brittenham GM, Prince MR. Clinical quantitative susceptibility mapping (QSM): Biometal imaging and its emerging roles in patient care. *Journal of magnetic resonance imaging : JMRI* 2017;46(4):951-971.
97. Wisnieff C, Liu T, Spincemaille P, Wang S, Zhou D, Wang Y. Magnetic susceptibility anisotropy: cylindrical symmetry from macroscopically ordered anisotropic molecules and accuracy of MRI measurements using few orientations. *Neuroimage* 2013;70:363-376.
98. Chen W, Gauthier SA, Gupta A, Comunale J, Liu T, Wang S, Pei M, Pitt D, Wang Y. Quantitative susceptibility mapping of multiple sclerosis lesions at various ages. *Radiology* 2014;271(1):183-192.
99. Tan H, Liu T Fau - Wu Y, Wu Y Fau - Thacker J, Thacker J Fau - Shenkar R, Shenkar R Fau - Mikati AG, Mikati Ag Fau - Shi C, Shi C Fau - Dykstra C, Dykstra C Fau - Wang Y, Wang Y Fau - Prasad PV, Prasad Pv Fau - Edelman RR, Edelman Rr Fau - Awad IA, Awad IA. Evaluation of iron content in human cerebral cavernous malformation using quantitative susceptibility mapping. (1536-0210 (Electronic)).
100. Murakami Y, Kakeda S, Watanabe K, Ueda I, Ogasawara A, Moriya J, Ide S, Futatsuya K, Sato T, Okada K, Uozumi T, Tsuji S, Liu T, Wang Y, Korogi Y. Usefulness of quantitative susceptibility mapping for the diagnosis of Parkinson disease. (1936-959X (Electronic)).

101. Wilks DS. Chapter 15 - Cluster Analysis. In: Wilks DS, editor. International Geophysics. Volume 100: Academic Press; 2011. p 603-616.
102. Skare S, Hartwig A, Martensson M, Avventi E, Engstrom M. Properties of a 2D fat navigator for prospective image domain correction of nodding motion in brain MRI. *Magn Reson Med* 2015;73(3):1110-1119.
103. Wang Y, Rossman PJ, Grimm RC, Wilman AH, Riederer SJ, Ehman RL. 3D MR angiography of pulmonary arteries using realtime navigator gating and magnetization preparation. *Magnetic resonance in medicine* 1996;36(4):579-587.
104. Nguyen TD, Nuval A, Mulukutla S, Wang Y. Direct monitoring of coronary artery motion with cardiac fat navigator echoes. *Magn Reson Med* 2003;50(2):235-241.
105. Haacke EM, Tang J, Neelavalli J, Cheng YCN. Susceptibility mapping as a means to visualize veins and quantify oxygen saturation. *Journal of Magnetic Resonance Imaging* 2010;32(3):663-676.
106. Stadlbauer A, Zimmermann M, Kitzwogger M, Oberndorfer S, Rossler K, Dorfler A, Buchfelder M, Heinz G. MR Imaging-derived Oxygen Metabolism and Neovascularization Characterization for Grading and IDH Gene Mutation Detection of Gliomas. *Radiology* 2017;283(3):799-809.
107. Benjamin EJ, Blaha MJ, Chiuve SE, Cushman M, Das SR, Deo R, Ferranti SD, Floyd J, Fornage M, Gillespie C, Isasi CR, Jiménez MC, Jordan LC, Judd SE, Lackland D, Lichtman JH, Lisabeth L, Liu S, Longenecker CT, Mackey RH, Matsushita K, Mozaffarian D, Mussolino ME, Nasir K, Neumar RW, Palaniappan L, Pandey DK, Thiagarajan RR, Reeves MJ, Ritchey M, Rodriguez CJ, Roth GA, Rosamond WD, Sasson C, Towfighi A, Tsao CW, Turner MB, Virani SS, Voeks JH, Willey JZ, Wilkins JT, Wu JH, Alger HM, Wong SS, Muntner P. Heart Disease and Stroke Statistics—2017 Update: A Report From the American Heart Association. *2017;135(10):e146-e603.*

108. Adeoye O, Nyström KV, Yavagal DR, Luciano J, Nogueira RG, Zorowitz RD, Khalessi AA, Bushnell C, Barsan WG, Panagos P, Alberts MJ, Tiner AC, Schwamm LH, Jauch EC. Recommendations for the Establishment of Stroke Systems of Care: A 2019 Update. *Stroke* 2019;50(7):e187-e210.
109. Nogueira RG, Jadhav AP, Haussen DC, Bonafe A, Budzik RF, Bhuva P, Yavagal DR, Ribo M, Cognard C, Hanel RA, Sila CA, Hassan AE, Millan M, Levy EI, Mitchell P, Chen M, English JD, Shah QA, Silver FL, Pereira VM, Mehta BP, Baxter BW, Abraham MG, Cardona P, Veznedaroglu E, Hellinger FR, Feng L, Kirmani JF, Lopes DK, Jankowitz BT, Frankel MR, Costalat V, Vora NA, Yoo AJ, Malik AM, Furlan AJ, Rubiera M, Aghaebrahim A, Olivot J-M, Tekle WG, Shields R, Graves T, Lewis RJ, Smith WS, Liebeskind DS, Saver JL, Jovin TG. Thrombectomy 6 to 24 Hours after Stroke with a Mismatch between Deficit and Infarct. *Stroke* 2017;378(1):11-21.
110. Albers GW, Marks MP, Kemp S, Christensen S, Tsai JP, Ortega-Gutierrez S, McTaggart RA, Torbey MT, Kim-Tenser M, Leslie-Mazwi T, Sarraj A, Kasner SE, Ansari SA, Yeatts SD, Hamilton S, Mlynash M, Heit JJ, Zaharchuk G, Kim S, Carrozzella J, Palesch YY, Demchuk AM, Bammer R, Lavori PW, Broderick JP, Lansberg MG. Thrombectomy for Stroke at 6 to 16 Hours with Selection by Perfusion Imaging. *Stroke* 2018;378(8):708-718.
111. Sobesky J, Zaro Weber O, Lehnhardt FG, Hesselmann V, Neveling M, Jacobs A, Heiss WD. Does the mismatch match the penumbra? Magnetic resonance imaging and positron emission tomography in early ischemic stroke. *Stroke* 2005;36(5):980-985.
112. Dirnagl U, Iadecola C, Moskowitz MA. Pathobiology of ischaemic stroke: an integrated view. *Trends in neurosciences* 1999;22(9):391-397.
113. Zhang S, Yao Y, Shi J, Tang X, Zhao L, Zhu W. The temporal evolution of diffusional kurtosis imaging in an experimental middle cerebral artery occlusion (MCAO) model. *Magnetic resonance imaging* 2016;34(7):889-895.
114. Aboul-Enein F, Lassmann H. Mitochondrial damage and histotoxic hypoxia: a pathway of tissue injury in inflammatory brain disease? *Acta neuropathologica* 2005;109(1):49-55.

115. Ge Y, Zhang Z, Lu H, Tang L, Jaggi H, Herbert J, Babb JS, Rusinek H, Grossman RI. Characterizing brain oxygen metabolism in patients with multiple sclerosis with T2-relaxation-under-spin-tagging MRI. *Journal of cerebral blood flow and metabolism : official journal of the International Society of Cerebral Blood Flow and Metabolism* 2012;32(3):403-412.
116. Fan AP, Govindarajan ST, Kinkel RP, Madigan NK, Nielsen AS, Benner T, Tinelli E, Rosen BR, Adalsteinsson E, Mainero C. Quantitative oxygen extraction fraction from 7-Tesla MRI phase: reproducibility and application in multiple sclerosis. *Journal of cerebral blood flow and metabolism : official journal of the International Society of Cerebral Blood Flow and Metabolism* 2015;35(1):131-139.
117. Moncada S, Bolanos JP. Nitric oxide, cell bioenergetics and neurodegeneration. *Journal of neurochemistry* 2006;97(6):1676-1689.
118. Varghese J, Potter LC, LaFountain R, Pan X, Raman SV, Ahmad R, Simonetti OP. CMR-based blood oximetry via multi-parametric estimation using multiple T2 measurements. *Journal of cardiovascular magnetic resonance : official journal of the Society for Cardiovascular Magnetic Resonance* 2017;19(1):88.
119. Wang Y, Spincemaille P, Liu Z, Dimov A, Deh K, Li J, Zhang Y, Yao Y, Gillen KM, Wilman AH, Gupta A, Tsiouris AJ, Kovanlikaya I, Chiang GC-Y, Weinsaft JW, Tanenbaum L, Chen W, Zhu W, Chang S, Lou M, Kopell BH, Kaplitt MG, Devos D, Hirai T, Huang X, Korogi Y, Shtilbans A, Jahng G-H, Pelletier D, Gauthier SA, Pitt D, Bush AI, Brittenham GM, Prince MR. Clinical quantitative susceptibility mapping (QSM): Biometal imaging and its emerging roles in patient care. *Journal of magnetic resonance imaging : JMRI* 2017;46(4):951-971.
120. Yao Y, Nguyen TD, Pandya S, Zhang Y, Hurtado Rua S, Kovanlikaya I, Kuceyeski A, Liu Z, Wang Y, Gauthier SA. Combining Quantitative Susceptibility Mapping with Automatic Zero Reference (QSM0) and Myelin Water Fraction Imaging to Quantify

- Iron-Related Myelin Damage in Chronic Active MS Lesions. *AJNR American journal of neuroradiology* 2018;39(2):303-310.
121. Kaunzner UW, Kang Y, Zhang S, Morris E, Yao Y, Pandya S, Hurtado Rua SM, Park C, Gillen KM, Nguyen TD, Wang Y, Pitt D, Gauthier SA. Quantitative susceptibility mapping identifies inflammation in a subset of chronic multiple sclerosis lesions. *Brain : a journal of neurology* 2019;142(1):133-145.
 122. Gardner RV. Sickle Cell Disease: Advances in Treatment. *Ochsner J* 2018;18(4):377-389.
 123. Kim JS. Moyamoya Disease: Epidemiology, Clinical Features, and Diagnosis. *J Stroke* 2016;18(1):2-11.
 124. Phi JH, Wang K-C, Lee JY, Kim S-K. Moyamoya Syndrome: A Window of Moyamoya Disease. *J Korean Neurosurg Soc* 2015;57(6):408-414.
 125. Li J, Jin M, Sun X, Li J, Liu Y, Xi Y, Wang Q, Zhao W, Huang Y. Imaging of Moyamoya Disease and Moyamoya Syndrome: Current Status. *J Comput Assist Tomogr* 2019;43(2):257-263.
 126. Bollmann S, Rasmussen KGB, Kristensen M, Blendal RG, Østergaard LR, Plochanski M, O'Brien K, Langkammer C, Janke A, Barth M. DeepQSM - using deep learning to solve the dipole inversion for quantitative susceptibility mapping. *Neuroimage* 2019;195:373-383.
 127. Yoon J, Gong E, Chatnuntaweck I, Bilgic B, Lee J, Jung W, Ko J, Jung H, Setsompop K, Zaharchuk G, Kim EY, Pauly J. Quantitative susceptibility mapping using deep neural network: QSMnet. *Neuroimage* 2018;179:199-206.
 128. Jin KH, McCann MT, Froustey E, Unser M. Deep Convolutional Neural Network for Inverse Problems in Imaging. *IEEE Transactions on Image Processing* 2017;26(9):4509-4522.

129. McCann MT, Jin KH, Unser M. Convolutional Neural Networks for Inverse Problems in Imaging: A Review. *IEEE Signal Processing Magazine* 2017;34(6):85-95.
130. Hornik K. Approximation capabilities of multilayer feedforward networks. *Neural Networks* 1991;4(2):251-257.
131. Ronneberger O, Fischer P, Brox T. U-Net: Convolutional Networks for Biomedical Image Segmentation. *Medical Image Computing and Computer-Assisted Intervention – MICCAI 2015*; 2015; Cham. Springer International Publishing. p 234-241. (*Medical Image Computing and Computer-Assisted Intervention – MICCAI 2015*).
132. Lehtinen J, Munkberg J, Hasselgren J, Laine S, Karras T, Aittala M, Aila T. Noise2Noise: Learning Image Restoration without Clean Data. In: Jennifer D, Andreas K, editors. *Proceedings of the 35th International Conference on Machine Learning*. Volume 80. *Proceedings of Machine Learning Research: PMLR %J Proceedings of Machine Learning Research*; 2018. p 2965--2974.
133. Fan AP, Khalil AA, Fiebach JB, Zaharchuk G, Villringer A, Villringer K, Gauthier CJ. Elevated brain oxygen extraction fraction measured by MRI susceptibility relates to perfusion status in acute ischemic stroke. *Journal of cerebral blood flow and metabolism : official journal of the International Society of Cerebral Blood Flow and Metabolism* 2019;271678x19827944.
134. Ito H, Kanno I, Kato C, Sasaki T, Ishii K, Ouchi Y, Iida A, Okazawa H, Hayashida K, Tsuyuguchi N, Ishii K, Kuwabara Y, Senda M. Database of normal human cerebral blood flow, cerebral blood volume, cerebral oxygen extraction fraction and cerebral metabolic rate of oxygen measured by positron emission tomography with ¹⁵O-labelled carbon dioxide or water, carbon monoxide and oxygen: a multicentre study in Japan. *European Journal of Nuclear Medicine and Molecular Imaging* 2004;31(5):635-643.
135. Driver ID, Wise RG, Murphy K. Graded Hypercapnia-Calibrated BOLD: Beyond the Iso-metabolic Hypercapnic Assumption. 2017;11(276).

136. Jackson JD. Classical electrodynamics: Wiley; 1999.
137. Kanwal RP. Generalized functions theory and technique: Theory and technique: Springer Science & Business Media; 2012.